NORTHWESTERN UNIVERSITY

Electrostatic Mechanisms for Shape Selection in Charged Chiral Molecular Assemblies

A DISSERTATION

SUBMITTED TO THE GRADUATE SCHOOL
IN PARTIAL FULFILLMENT OF THE REQUIREMENTS

for the degree

DOCTOR OF PHILOSOPHY

Department of Physics and Astronomy

By

Joseph Maurice McCourt

EVANSTON, ILLINOIS

June, 2023

Abstract

How molecular chirality manifests at the nano- to macroscale has been a scientific puzzle since Louis Pasteur discovered biochirality. In general, amphiphilic molecules can organize into a vairety of assembly shapes including micelles, spherical vesicles, cylindrical micelles, and planar bilayers. However, when such amphiphilic molecules are chiral, helical ribbons, helicoidal scrolls (cochleates), twisted ribbons and even möbius strips (closed twisted ribbons) appear. These fascinating supramolecular chiral materials have particular properties that make them useful for applications in drug delivery, biosensors, nanoelectronics, and chiral recognition devices. Controlling the shape and internal architecture of the assemblies is critical for these technologies, but the structure, and thus the function, of these hierarchical assemblies reconfigure in response to stimuli, via mechanisms that are often elusive. In this study, we observe and explain how molecular reordering driven by variations in electrostatic interactions can induce micrometer-scale structural changes in membranes of charged, chiral molecules. The size, shape, and charge of soft assembled nano-structures, like those in biology, respond in an interconnected manner to solution ionic conditions, providing a pathway to shape control of chiral materials. This study combines experimental, theoretical, and computational approaches to elucidate key principles in analyzing the coupling of electrostatics and nano-scale details of soft nano-structures. These preliminary efforts have led to development of an electrostatics-based approach for assembly shape selection and nano-scale structure control in chiral assemblies.

Acknowledgements

First and foremost, I would like to thank my advisor Prof. Michael Bedzyk and co-advisor Prof. Monica Olvera de la Cruz for giving me the opportunity to work in their research groups. I was very excited about the opportunity about working on both experiment and computation in my research and it was only possible with their support. I would also like to give a huge thanks to Dr. Sumit Kewalramani who acted as my mentor for the past 5 years. He has taught me so much and I really appreciate all the time he has given to me. I would also like to thank Prof. John Marko for his teaching and also his inspiration as a physicist. Finally I would like to thank Dr. Felipe Jimenez Angeles for his assistance in many of my simulation efforts over the years. These individuals form my thesis defense committee and I would like to thank them for taking the time to review my work.

I would like to take this time to thank the Department of Energy (DOE), Office of Basic Energy Sciences who supported a financially supported a bulk of my research. I would also like to acknowledge the Center for Computation and Theory of Soft Materials (CCTSM) which provided additional support. This research made use of the Peptide Synthesis Core Facility of the Simpson Querrey Institute, Keck Biophysics facility, NUANCE Center, and Quest High-Performance Computing Cluster at Northwestern University. In addition, much work was performed at the Advanced Photon Source (APS) at Argonne National Lab (ANL). Thank you to the management and staff of these centers and institutions. Specifcally, I would like to thank my experimental collaborators in these institutions over the years. I thank Mark Karver for peptide synthesis, Dr. Eric W. Roth for cryogenic electron microscopy measurements, and Dr. Steven Weigand and Dr. Soenke Seifert for assistance with measurements performed at the APS, especially during the COVID-19 pandemic lockdown times where all experiments were performed remotely.

Many people over the years have provided me with support, guidance, and overall enjoyable conversation. I would like to thank Prof. Michelle Driscoll for opportunity to work in her research group during my first year at Northwestern and ensuing a passion for soft matter physics. It was also during these early years that I met fellow physics PhD students Aretaios Lalakos, Michael MacKenzie, Dr. Daniel Weiss, Dr. Weihua Lei, Patrick Krantz, and many more who now make up some of my closet friends. I would like to thank them for their friendship over the years and thank the entire Northwestern Department of Physics and Astronomoy community. In addition, I would like to thank fellow members of my research groups. To name a few, I would like to thank Dr. Trung Nguyen, Dr. Baofu Qiao, Dr. Hang Yuan, Dr. Jeremy Wang, Dr. Elise Goldstein, Carlos Torres, Roger Reinertsen, David Garcia, Selin Cetin, Amol Agarwal, Dan Duplessis, Dr. Leticia Lopez-Flores, Dr. Dulce Maria Valencia, Dr. Anusheela Das, Dr. Yanna Chen, Dr. Katherine Harmon, and Dr. Guennadi Evmenenko. I would also like to thank a variety of strangers whom I will never meet who worked to develop a variety of open source packages that I have used over the years in my research. Thank for sharing your work with everyone.

During my studies, I was diagnosed with Type 1 Diabetes. While it was a life adjustment, I would like to take some time to thank Northwestern Health Services and Northwestern Medicine for making the transition as manageable as possible. They have helped me with a variety of things over the years. With the COVID-19 pandemic still fresh in our memories, I think it is an especially important time to be thankful for the members of our medical communities. And thank you to the scientists of times past who discovered insulin, which is the medicine that keeps me alive today.

Finally, I would like to thank the people closest to me. A special thanks goes to my partner, Kelsea Chang, who came into my life just a year and a half ago. I appreciate her unconditional love and support and everything she does for me. She has introduced me to a whole new group of friends and I am looking forward to our future together. I would like to thank my family for without their support, my memorable time at Northwestern would not have been possible. To my mother, Michelle, my twin brother Tommy, my triplet siblings Al, Kitty and Tina, my older brother Jimmy, my Uncle Herb and Aunt Erin, and many more as I have a large loving family, I appreciate you all so much. And thank you to my cat Charlie, who has been there every step of the way throughout this journey.

List of Symbols and Abbreviations

C_nK_m	molecular chemical formula: alkyl tail of n carbons covalently bonded to headgroup consisting of m lysine amino acids
L-,D-	left-, right-handed amino acid
λ_D	Debye screening length
α	degree of ionization
K_a	chemical reaction coefficient (e.g. deprotonation of amine side chain in lysine amino acid)
m	Hill coefficient
λ	wavelength (e.g. X-ray)
ρ	electron density (e.g. $\rho_{water} = 334$ e/nm^3)
q	scattering vector
k_BT	Boltzmann constant $k_B \times$ absolute temperature T = 4.1 pN $\cdot$ nm at $T \simeq 300$ K, room temperature
pH	$-\log_{10}[H^+]$, where $[H^+]$ is the molar concentration of H^+ ions
l_B	Bjerrum length
e	elementary charge $\simeq 1.6 \times 10^{-19}$ C
ψ	electrostatic potential

Ψ	ψ / k_BT
SAXS/WAXS	**S**mall/**W**ide **A**ngle **X**-ray **S**cattering
PA	**P**eptide **A**mphiphile
HH	**H**enderson **H**asselbach
MD	**M**olecular **D**ynamics
CG	**C**oarse **G**rained
CD	**C**ircular **D**ichroism
CR	**C**harge **R**egulation
(**cyro**-) **TEM**	(**cyro**genic-) **T**ransmission **E**lectron **M**icroscopy
APL	**A**rea **P**er **L**ipid
PB	**P**oisson **B**oltzmann
APS	**A**dvanced **P**hoton **S**ource
DND-CAT	**D**upont-**N**orthwestern-**D**ow **C**ollaborative **A**ccess **T**eam
DOE	**D**epartment **o**f **E**nergy
CCTSM	**C**enter for **C**omputation and **T**heory of **S**oft **M**aterials

To all of my teachers: those I’ve had, those I’ve admired, and those I’ve never met.

Contents

List of Tables

List of Figures

0 Introduction

0.1 Charged Chiral Amphiphiles

Chirality, or handedness, has a long history of importance in physics, chemistry, and biology. The most common example is our left and right hands, which are distinct mirror images of one another. Nature itself has been called chiral as many biomolecules exist naturally in only one handedness. Examples include the L-entaniomer amino acids that constitute proteins (Figure 1A), phospholipids that make up the cell membrane, and the most famous exemplification: nature's right-handed genetic code, DNA. In addition, chirality can manifest itself on the macroscopic scale with examples including the spirals on shell's of snails and helical plant tendrils (Figure 1B,C) [1].

Researchers have found that molecular chirality plays an important role in determining and controlling the shape of self-assembled supramolecular amphiphilic aggregates. The molecular chirality is often manifested in fascinating mesoscopic chiral shapes such as helical ribbons and nanotubes with barber-pole like markings [2, 3, 4, 5, 6, 7, 8], twisted ribbons [7, 8, 9, 10], helicoidal scrolls (cochleates) [11, 12, 13, 14], and möbius strips [15]. Figure 2 shows cartoon examples of all of these structures. The competing hydrophillic and hydrophobic interactions of the amphiphilic molecules lead to assembly, commonly bilayers, with head groups facing the surrounding water and tail groups being shielded from the water. The equilibrium molecular distances in the membrane are determined by the competition between the attractive and repulsive intermolecular interactions. The assembly then experiences an additional bending force that arises because a close packing of chiral molecules in the membranes necessitates a relative twist between the neighboring molecules. This is qualitatively analogous to the case of packing of hard screws of a given handedness [16, 17].

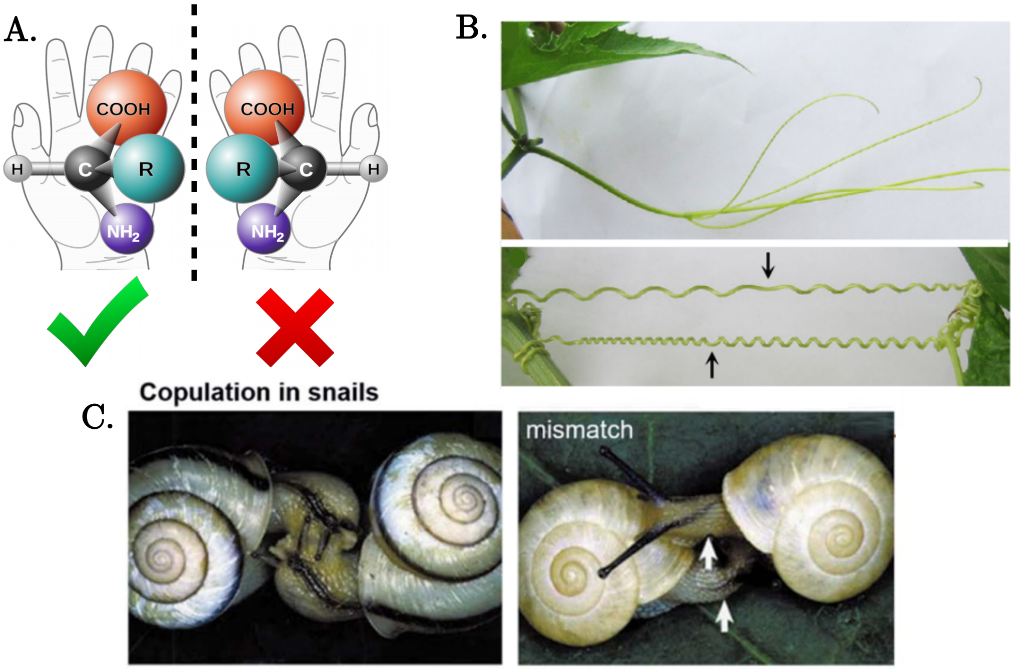

Figure 1: Taken from [18]: **A.** General chemical structures of amino acids, where the R group side chain varies between different amino acids. Only left-handed amino acids exist naturally, but right-handed amino acids can also be synthetically reproduced. The choice of nomenclature for left vs. right is by convention. Taken from [1]: **B.** Plant tendrils extend off from a central stem, which upon contacting another surface, twist to form helical ribbon-like structures with increased stability. **C.** Snails can only reproduce with another snail whose shell spiral has the same handedness. This is due to steric constraints of opposite handed shells and how snails coopulate.

An additional consideration for assemblies of the mentioned biological chiral macromolecules is that they are all charged. The phosphate groups contained in nucleic acids that make up DNA and phospholipids of the cell membrane have a fixed net charge at biologically relevant conditions and amino acids have charged chemical groups whose ionization state depends on the surrounding ion environment. The resulting electrostatic interactions can determine the details of molecular packing and thereby indirectly modulate chiral assemblies. For example, zwitterionic phospholipids assemble into helices and nanotubes [2, 3, 19]. By contrast, cochleates have been observed for phospholipids that are negatively charged [11, 12, 13]. Similarly, tuning the molecular charge can induce transformation between different chiral sturctures such as helical and twisted ribbons.[20]

Finally, the range of electrostatic interactions can control overall structural properties such as the pitch of twisted ribbons in amyloid fibrils [21]. Charge and chirality (or parity) together are part of fundamental symmetries in physics and their universal importance cannot be overstated (see [22] for a light discussion).

Detecting and explaining how achiral electrostatic or van der Waals assembly interactions can control shape selection and nano-scale structure in chiral assemblies has remained elusive due to variety of reasons. Inhibiting future development is the limited amount of molecular modeling of the membranes that form helical assemblies. Therefore, the relation between the chemical structure of the molecules to the elastic constants on which most theoretical work is based is elusive. Experimental analysis of the molecular order and orientation in chiral assemblies is also limited due to inherent difficulty of measuring positional correlations (e.g. crystallinity) between neighboring molecules in solution assemblies that give rise to the chiral twisting force. In addition, electrostatic effects are commonly ignored in the existing models. Further study and analysis is important for attaining and optimizing distinct structures based on chiral building blocks for varied applications. The use of a simple system in exploring the phase space of charged chiral shapes would help pave the way for development of theories and design principles for unique soft assembly structures.

0.1.1 Examples of Assembly Shapes in Nature and Applications

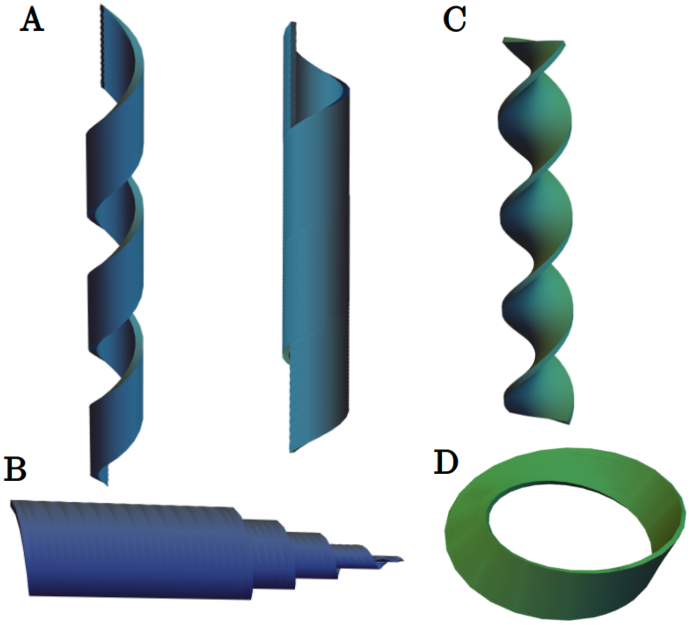

Figure 2: Cartoon drawings of chiral shapes: **A.** helical ribbon and closed helical tubule, **B.** cochleate (scroll-like), **C.** twisted ribbon and **D.** möbius strip.

As stated above, self-assembly in simple synthetic chiral molecular systems can provide insights into important biophysical processes and have been found in a wide variety of systems [23]. For example, helical ribbons and tubules observed in the synthetic bile salt containing crystallized cholesterol are analogous to chiral shapes observed in the process of gallstone formation [24]. In addition, soft chiral assemblies have potential nanotechnological applications that depend sensitively on the overall shape and nm-scale structural details of these assemblies. Helicoidal scrolls are being explored as drug/macromolecular delivery platforms due to their ability to encapsulate nanoscale objects within the bilayers (hydrophobic molecules) and in the aqueous phase between adjacent bilayers (hydrophilic molecules) [12]. Here, the bilayer thickness and the inter-bilayer separation determines the size of the objects that such cochleates can trap and release. Templated helical ribbons and nanotubes are recognized as possible nano- and meso-electronic components such as nanowires and solenoids [25, 26]. The diameter and the helical pitch of these assemblies determine the nanowire properties and solenoid turn densities. Similarly, the nanotube diameter determines the diffusion rate of entrapped molecules in controlled release applications. For applications of helices and nanotubes, see excellent reviews and references therein [5, 6, 27, 28]. These examples illustrate the need for developing control over shape selection and internal architecture of chiral assemblies.

0.2 Theoretical Background

0.2.1 Amphiphillic Assembly

Many molecular aggregates including micelles, microemulsions, bilayers, vesicles, biological membranes, and macromolecules such as proteins form readily in aqueous solution by the self-assembly of *amphiphilic molecules*. Containing both a *hydrophobic* and *hydrophillic* component, these molecules associate themselves with a water based solvent accordingly to keep hydrohobic components away from the solvent and the hydrophillic components in contact with the solvent. When placed in solution, these *soft* self-assembled structures and the systems they form stand apart from other assemblies in one important respect: unlike solid particles or rigid macromolecules such as viruses, globular proteins, and DNA, they are fluid-like.[29] This is because the forces that hold amphiphilic molecules together in micelles and bilayers area are not due to strong covalent or ionic bonds but arise from weaker van der Waals, hydrophobic, and hydrogen-bonding. The fluidity of the assemblies results in the ability to bend and stretch into a variety of complex configurations while still having positional ordering. A typical amphiphilic molecule is composed of a hydrophobic hydrocarbon tail and polar/charged headgroup, i.e. a lipid. Due to the preferences of these two molecular groups, the molecules assemble into a bilayer with the hydrophilic headgroups facing towards the water and tails facing towards each other with van der Waals attractions between tail regions leading to stable structures.

These assemblies are then also affected by screened electrostatic interactions as they are in solution. If the solution conditions, such as the electrolyte concentration or the pH, of an aqueous suspension of aggregates is changed, not only will this affect the interactions between the aggregates, but it will also affect the intermolecular forces within each aggregate, thereby modifying the size and shape of the structures themselves. It is therefore necessary to begin by considering the electrostatic interactions that determine how and why certain molecules in solution associate into various well-defined structures.

0.2.2 Electrostatic Interactions in Solution

The Poisson-Boltzmann equation is the starting point for describing electrostatic interactions in solution. It aims to describe the distribution of the electric potential in solution in the direction normal to a charged surface. This distribution is important to determine how the electrostatic interactions will affect the other surrounding molecules and ions. We begin with the Poisson equation for describing the electrostatic potential ψ and describe the distribution of the ions (of concentration c_i and valency z_i) with Boltzmann statistics:

$$\nabla^2\psi(r) = -\frac{\rho(r)}{\epsilon} \tag{1}$$

$$\rho(r) = c_i z_i e^{-z_i e\psi(r)/k_B T} \tag{2}$$

Performing a Taylor expansion of eq 2 and combining it with eq 1, we acquire

$$\nabla^2\psi(r) = \frac{1}{\lambda_D^2}\psi(r) \tag{3}$$

$$\implies \psi(r) = \psi_0 \exp\left[\frac{-r}{\lambda_D}\right]$$

where $\lambda_D \equiv$ *Debye screening length* $= \sqrt{\frac{\epsilon k_B T}{2e^2 I_s}}$ and $I_s \equiv$ *ionic strength* $= \sum_i c_i z_i^2$. eq 3 is the well known Poisson Boltzmann formulation. The screening length is directly related to the prevalence of electrolytes (ions) in the system. Increasing the number of ions leads to a smaller screening length and an exponential reduction in the range of electrostatic interactions.

Adjusting the pH ($\equiv -\log_{10}\left([H^+]\right)$) of a solution is another way to modify the electrostatic environment of a solution system. The pH (or conversely, pOH) level influences the proton exchange of ionizable molecules. For example, five of the twenty amino acids have ionizable side chains whose charge value depends on the pH of the surrounding solution. It is easiest to describe such processes with simple chemical reactions based on the concepts of *acids* (proton donors) and *bases* (proton acceptors).

$$\begin{gathered} A^- + H^+ \rightleftharpoons AH \\ B + H^+ \rightleftharpoons BH^+ \end{gathered} \tag{4}$$

One example of a acid and base is HCl (hydrochloric acid) and NaOH (sodium hydroxide), respectively. Such molecules are commonly used to decrease and increase the pH of a solution respectively. These molecules readily dissociate in water and the reactions are as follows:

$$\begin{gathered} HCl \rightleftharpoons H^+ + Cl^- \\ NaOH \rightleftharpoons OH^- + Na^+ \end{gathered} \tag{5}$$

When an assembly consists of an ionizable molecule, the magnitude of the surface charge is therefore determined by the pH and is affected by the presence of other charged entities in the vicinity. This process is known as *charge regulation* (CR) [30]. Although this phenomenon has been theoretically studied since the seminal work by Kirkwood in the 1950s [31], the assumption that all objects carry a constant charge is still widely employed. Surface charge distribution plays a key role in macromolecular structure formation in biomolecular systems. Charge regulation is particularly relevant for aggregation owing to the relation between the charge distribution and the structure of the aggregate.

0.2.3 Continuum Models for Chiral Assemblies

As stated within the introduction, a close-packed assembly of chiral molecules necessitates that the neighboring molecules are tilted with respect to each other. This is similar to the case of packing of hard screws. While this classical analogy has limitations, it provides an accurate approximation and intuitive understanding of the origin of the chiral twisting force in chiral assemblies [17, 32, 33].

Previous theoretical studies have focused on using phenomenological elastic models to explain the shapes seen in chiral assemblies. We start with the Canham-Helfrich free energy density for the bending of some general surface.

$$f = \kappa\Big(\frac{1}{R_1} + \frac{1}{R_2}\Big)^2 + \kappa_G\Big(\frac{1}{R_1 R_2}\Big) \tag{6}$$

where R_1 and R_2 are the principal radii of curvature of the surface and κ and κ_G are the moduli for mean curvature and Gaussian curvature respectively [34, 35]. As an example, for the case of a cylinder of radius R, $f_{cyl} = \kappa\big(\frac{1}{R}\big)^2$, with $R_1 = R$ and $R_2 \to \infty$. While chiral interactions can lead to a number of shapes such as closed cylindrical tubules or helical ribbons with cylindrical (mean) curvature and twisted ribbons with saddle-like (Gaussian) curvature (Figure 2,[23]), We first focus on helical ribbons/tubules to illustrate the goal of continuum models. Most energetic models incorporate chirality by orientational order in the tilt and positional correlations of the molecules. The simplest model put forward by Helfrich-Prost (HP) writes a free energy [36]

$$F = \int dA \kappa\Big(\frac{1}{r^2}\Big) - \lambda_{HP}\Big(\frac{1}{r}\Big)\sin\phi\cos\phi \tag{7}$$

The first term in equation eq 7 is identical to the free energy for a cylindrical surface as a helical ribbon has the same mean curvature as a cylinder, but now there is an additional term linear in the curvature $\big[\sim \big(\frac{1}{r}\big)\big]$ whose strength is controlled by the chiral coupling parameter λ_{HP}. This term depends on the projected molecular tilt angle ϕ (Figure 3). Note, even without a detailed molecular model of a membrane, we can make two statements about λ_{HP} purely on the basis of symmetry. First, if we replace all molecules in a system by their enantiomers, then the entire membrane transforms into its mirror image, and λ_{HP} must change sign. Hence, the helical tubule radius r remains the same, but the tilt orientation ϕ is reversed, giving the mirror-image tubule structure. Second, because λ_{HP} depends on the chiral order of the membrane, we should be able to reduce it by diluting chiral effects. If chiral molecules are mixed with their enantiomers, λ_{HP} should scale linearly with the enantiomeric excess for small enantiomeric excess [17].

In general, for surfaces without Gaussian curvature, we may write

$$F = \int dA \kappa C^2 - \lambda_{HP} C \sin\phi \cos\phi \tag{8}$$

where C is the mean curvature of the surface.

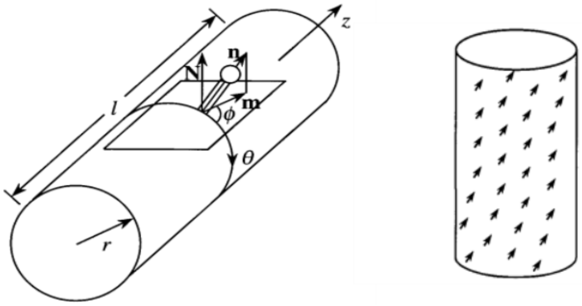

Figure 3: Taken from [17]. Geometry for tubule formed from tilted chiral molecules. Here, r is the tubule radius, l is the tubule length, n is the molecular director, m is the projection of n into the local tangent plane (normalized to unit magnitude), ϕ is the angle in the tangent plane between m and the curvature direction (the equator running around the cylinder), and N is the local normal vector.

This model focuses on what effects orientational order in the tilt of molecules with respect to a surface normal will have on bilayer elastic properties. To highlight some theoretical progress, another model which focused on tilt modulation along the surface was developed by Selinger et al. who proposed a kinetic evolution for bilayer ribbons into helical tubules based on defects [17]. Chung et al. considered that bending along the tilt vector or perpendicular to it will have different energetic penalties [24]. And Nelson and Powers considered more terms that could arise due to chirality than the HP model and analyzed thermal fluctuations of helical ribbon/tubules [37]. In fact, there are many competing models describing chiral lipid assemblies, most of which focus on orientational order in the tilt of the molecules [38]. Usually, electrostatic interactions are ignored and thus a main focus of of this work is to elucidate the electrostatic relationship to the observed chiral shapes and performing a systematic analysis of the different chiral morphologies. The work presented herein will add to the framework for theories of charged, chiral assemblies.

0.3 Research Question and Chapter Outlines

To summarize, an understanding of the relationship between charged chiral assembly morphologies and their interconversion mechanism is lacking due to the absence of a molecular system that enables a systematic exploration of the phase space of chiral shapes, and because the important electrostatic interactions are neglected in theoretical work. Therefore, using a combination of experimental, computational, and theoretical techniques, I propose to investigate the following question: ***How do electrostatic forces determine shape selection and molecular packing in charged, chiral amphiphile assemblies?***

We focus on a single charged chiral building block, C_nK_1, to serve as our molecular system. It consists of a single ionizable lysine amino acid head group (K) coupled to a carbon tail of length n (C_n). The following chapters are organized as follows.

Chapter 1: Here, a charged, chiral amphiphile (palmitoyl-lysine, $C_{16}K_1$) is used to elucidate the pathway for planar nano-ribbon to scroll-like cochleate assembly transition induced by salt (NaCl) concentration. In situ small- and wide-angle X-ray scattering (SAXS/WAXS), atomic force and cryogenic transmission electron microscopies (AFM and cryo-TEM) tracked these transformations over angstrom to micrometer length scales. SAXS shows that interbilayer spacing (D) in the cochleates scales linearly with the Debye length, and ranges from 13 to 35 nm for NaCl concentrations from 100 to 5 mM. Theoretical arguments that include electrostatic and elastic energies explain the membrane rolling and the bilayer separation–Debye length relationship. Our studies show how electrostatic interactions can be tuned to attain and control cochleate structures, which have potential for encapsulating, and releasing macromolecules in a size-selective manner.

Chapter 2: Here we extend our analysis of the self-assembly pathways for a series of amphiphiles, C_nK_1, consisting of an ionizable amino acid [lysine (K)] coupled to alkyl tails with n = 12, 14, or 16 carbons. This simple system allows us to probe the effects of electrostatic and van der Waals interactions in chiral assemblies. Small/wide-angle X-ray scattering (SAXS/WAXS) reveals that at low pH, where the headgroups are ionized (+1), $C_{16}K_1$ forms high aspect ratio, planar crystalline bilayers. Molecular dynamics (MD) simulations reveal that tilted tails of the bilayer leaflets are interdigitated. SAXS shows that, with increasing salt concentration, C$_{16}$K$_1$ molecules assemble into cochleates (as described in **Chapter 1**), whereas at elevated pH (reduced degree of ionization), helices are observed for all C$_n$K$_1$ assemblies. The shape selection between helices and scrolls is explained by a membrane energetics model. The nano- to meso-scale structure of the chiral assemblies can be continuously controlled by solution ionic conditions.

Chapter 3: We further extend our investigation of C$_n$K$_1$ systems. The most common chiral assembly shapes are helical membranes, helical scrolls (cochleates) and twisted membranes. These shapes have been observed in natural and synthetic systems. Despite the prevalence, an understanding of the interconversion mechanisms between different chiral morphologies is lacking. In this study, we were able to generate all the common chiral structures in perhaps the simplest chiral molecular series C$_n$K$_1$, where one amino acid [lysine (K)] is coupled to alkyl tails of n (= 8-18) carbons. This was accomplished by tuning the solution ionic conditions. Scroll-like assemblies were observed when the molecular degree of ionization was high, and the electrostatic interactions were short-ranged. By contrast, helical and twisted membranes are observed for long (n = 12-18) and short (n = 10) molecular tails, respectively, when the molecular degree of ionization was low and the electrostatic interactions were long-ranged. In addition we show we can control the formation of chiral or achiral structures by tuning the chiral coupling via varied ratios of enantiomers in the assemblies. These results were derived by combining X-ray scattering and electron/atomic force microscopy. Overall, our study reveals that electrostatic interactions can be used to guide chiral shape selection and nano-scale structure in molecular self-assemblies.

Chapter 4: We focus on a similar system, C$_{16}$K$_2$, to consider the case where the chiral assembly forces are weak compared to the electrostatics to better understand the coupling between electrostatics and the nano-scale geometry of the assemblies. The size, shape, and charge of soft assembled nano-structures, like those in biology, respond in an interconnected manner to solution ionic conditions. Customarily, the charge regulation of ionizable groups is described through a pK_a (ion dissociation constant), which is related to the degree of ionization of the group. pK_a values are commonly deduced from Henderson-Hasselbalch or Hill model fits to titration data. However, such models do not account for the size and shape of assemblies and lack a physical explanation for an apparent pK_a shift to some effective pK_a,eff for the same ionizable molecule in different assembly morphologies and ionic environments. This leaves a gap in the intuitive understanding of the charge regulation process. To tackle this problem, we combined X-ray scattering, titration measurements, and nonlinear Poisson-Boltzmann theory to predict the degree of ionization in highly charged, ionizable assemblies. We analyzed the self-assembly and charge regulation of the peptide amphiphile $C_{16}K_2$: a two ionizable amino acid [Lysine (K)] head group coupled to a 16-carbon length tail. Experiments revealed assembly shape and size transitions as a function of pH and salt concentration and detailed nanoscale structure. An electrostatic model then allowed extraction of the shape and size-dependent degree of ionization. In this way, we were able to reproduce experimental titration data without any adjustable parameters. Overall, our study elucidates key principles in analyzing the coupling of electrostatics and nano-scale details of soft nano-structures which play a crucial role in biological systems.

0.4 General Methods

0.4.1 Experimental

0.4.1.1 X-ray Scattering (SAXS/WAXS)

In-situ solution small/wide angle X-ray scattering (SAXS/WAXS) is the primary experimental technique for this project. Incoming X-ray photons ($\lambda \sim 0.01 - 100$ nm) of momentum $\boldsymbol{k_0}$ scatter off of an electron dense object with final momentum $\boldsymbol{k}$. For elastic scattering $|\boldsymbol{k_0}| = |\boldsymbol{k}|$ and we define a scattering vector $|\boldsymbol{q}| = |\boldsymbol{k} - \boldsymbol{k_0}| = \frac{4\pi \sin\theta}{\lambda}$, where θ is the scattering angle and λ is the X-ray wavelength (Figure 4). X-ray scattering off of electrons is weak and we can therefore use the Born approximation for independent scattering leading to the intensity profile for X-ray scattering being modelled as [39]

$$I(q) = \langle |F(\boldsymbol{q})|^2 \rangle_{\text{orientations}} \tag{9}$$

where the *form factor* F is the Fourier transform of the electron density distribution of the object relative to the background, $\Delta\rho(r)$.

$$F(\boldsymbol{q}) = \int \Delta\rho(r)\, \text{exp}\left[i\boldsymbol{q}\cdot\boldsymbol{r}\right] dV \tag{10}$$

With this, the intensity profile from the distribution of electrons with a given shape can be modelled explicitly with the geometry of the structure and the electron contrast between the object and its environment. Example calculations are shown in B.1. Due to the ability to look at a large amount of sample in a small amount of time, SAXS is a very useful technique for analyzing the geometry of chiral equilibrium stuctures and acquiring general characteristics of soft assemblies.

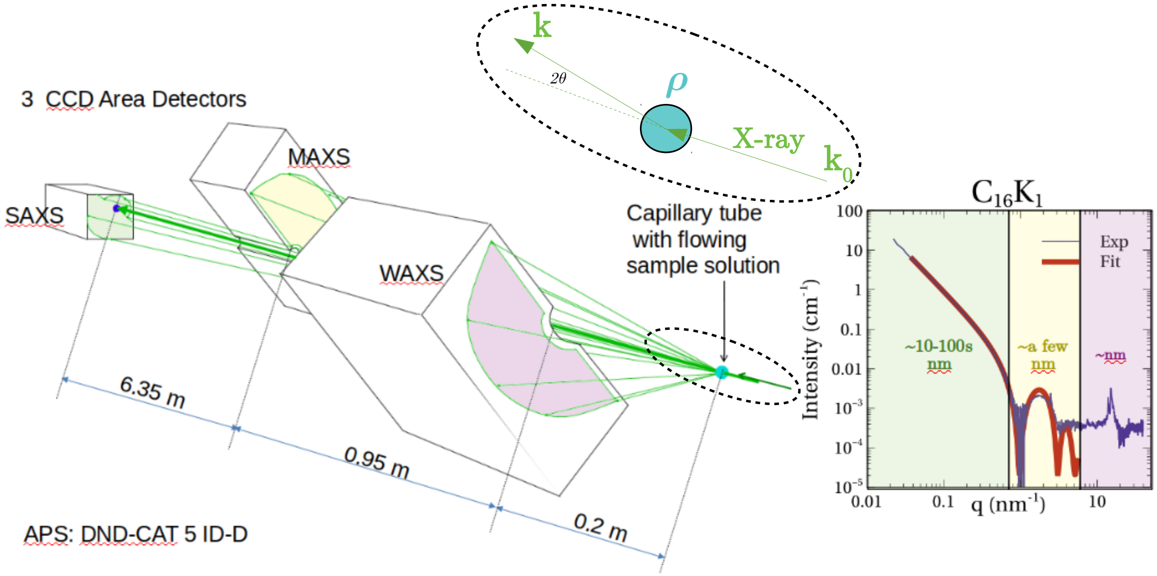

Figure 4: SAXS/MAXS/WAXS experimental set-up at Sector 5 ID-D at APS. Multiple detectors at different scattering angles allows for collection of information from a large range of length scales simultaneously. A scattering profile from a $C_{16}K_1$ bilayer ribbon assembly is shown on the right as an example, where colored regions correspond to information from the color matched detectors on the left.

0.4.1.2 Circular Dichroism (CD)

CD measures the preferential absorption of left and right circularly polarized light of assemblies in solution. A CD signal only occurs for helical ordering of charge, which makes it a common technique employed to look at helical/chiral structures [4, 40, 41]. The overall CD signal is given as $\Delta\epsilon \sim$ log $\frac{I_R}{I_L}$, where I corresponds to the fractional transmitted intensity of right and left circularly polarized light. A negative signal corresponds to preferential absorption of right circularly polarized light and similarly, there is positive signal for preferential absorption of left circularly polarized light, corresponding to opposite helical ordering.

0.4.1.3 Titration

Titration measurements involves the slow addition of a titrant and measuring how the pH of a solution containing a weak acid/base changes as you add more of the titrant (in our experiments, the titrant NaOH is used). A *titration curve* is a plot of the pH of a solution as a function of the volume of added titrant and is characterized by an *equivalence point*, pH=pH$_{equiv}$, where the titrant and solution are in concentration equilibrium. Another parameter that characterizes titration curves is the pK$_a = \frac{1}{2}$pH$_{equiv}$. For our experiments, titration is performed to measure the *degree of ionization*, α, of the assembly molecules as a function of the pH of the solution.

0.4.1.4 Atomic Force Microscopy (AFM) and Cryo-Transmission Electron Microscopy (Cryo-TEM)

Microscopy techniques, AFM and cryo-TEM, are another way to visualize the structures. In AFM, the information is gathered by touching the surface with a mechanical probe. When the probe/tip is brought into proximity of a sample surface, forces between the tip and the sample lead to a deflection of the cantilever according to Hooke's law. Piezoelectric elements that facilitate tiny but accurate movements enable precise scanning. AFM can be performed in both a solid and liquid environment. Cryo-TEM involves performing TEM analysis while keeping the sample at cryogenic temperatures. TEM is a technique that images a sample using an electron beam. where high energy electrons (80-200 keV) are transmitted through electron transparent samples and imaged on a plane. The study of thin, frozen slices of suspensions allows for morphology studies of particles in their dispersed state.

0.4.1.5 Peptide Amphiphile Synthesis

Our samples, C$_n$K$_m$olecules, were all synthesized with collaboration from Dr. Mark Karver by the Peptide Synthesis Core at Northwestern University

0.4.2 Computational

0.4.2.1 Molecular Dynamics (MD) Simulations

Classical MD simulations involve billiard ball like collisions. Electrons are not treated explicitly. We start with an initial configuration of atoms (or ”beads” if atoms are coarse-grained) and evolve the system according to Newton’s law.

$$\boldsymbol{F} = m\boldsymbol{a} = m\frac{d\boldsymbol{v}}{dt} = \frac{d\boldsymbol{p}}{dt} \tag{11}$$

$$\boldsymbol{F} = -\nabla V \tag{12}$$

Given the initial positions and velocities of every atom, if we have defined the potential for the system, then we have all forces on all atoms and can solve for the time evolution of the system. For MD simulations considered in this text, atoms (beads) will have bonded and non-bonded interactions. Bonded interactions including covalent bond-stretching, angle-bending, improper dihedrals, and proper dihedrals are computed on the basis of fixed lists for the given particles. Non-bonded interactions between two particles (i and j) use a Lennard-Jones (LJ) for short range attractive and repulsive forces

$$V_{LJ} = 4\epsilon_{ij}\Big[\Big(\frac{\sigma_{ij}}{r_{ij}}\Big)^{12} - \Big(\frac{\sigma_{ij}}{r_{ij}}\Big)^{6}\Big] \tag{13}$$

and a Coulomb potential for longer range electrostatic interactions

$$V_{Coul} = \frac{1}{4\pi\epsilon_0}\frac{q_i q_j}{\epsilon_r r_{ij}} \tag{14}$$

where r_{ij} is the separation between two particles, q_i is the electronic charge of particle i (similarly for q_j), ϵ_0 is the permittivity of free space (vacuum electric constant), ϵ_r is a relative dielectric constant, and ϵ_{ij}, σ_{ij} are taken from a matrix of LJ-parameters for a given force field which are created and optimized by fitting parameters to experimental data.

0.4.2.2 Continuum Modelling

Energetic models can be used to estimate equilibrium structures for assembly morphologies. This calculation begins with a continuum elastic free energy (e.g. 0.2.3, eq 7), meaning there is no discrete shape/orientation and chemical structure of the individual molecules, expressed in terms of the membrane elastic constants and ends with a prediction for the morphology. In addition, continuum modelling is used to model electrostatic interactions in solution as discussed in 0.2.2.

1 Chapter 1

“*It is a pleasure to find out how different observable phenomena of the physical world fit together...It is the discovering of the connection between physical phenomena and describing them by mathematical analysis, rather than the analysis itself, which is interesting.*”

-G.I. Taylor

In this chapter we analyze the chiral molecule $C_{16}K_1$ and its molecular assemblies. The formation of scroll-like (cochleate) chiral molecular assemblies with addition of the monovalent salt, NaCl, is discussed. The resulting screening of the electrostatic interactions with added salt leads to a manifestation of the molecular chirality at the supramolecular level in a transformation pathway from flat bilayer ribbon to sheet to cochleate. The precise characterization of this pathway suggests a robust method for controlling the structural details of scroll-like assemblies.

1.1 Introduction

Amphiphilic molecules can self-assemble into a variety of 3D, 2D, and 1D nano- and mesoscale structures. These structures serve as simplified models for understanding biological assemblies and their functions and have applications in drug delivery [12, 42, 43, 44, 45], regenerative medicine [46, 47], biosensing [48], hydrogen production [49, 50], and clean water technologies [51]. An interesting assembly structure is the nanoribbon, which is a high aspect ratio (10:1 or greater) bilayer. Nanoribbons are a gateway to a number of other morphologies with distinct functionalities. For example, nanoribbons of a charged chromophore amphiphile can transform to a scroll-like (cochleate) morphology when the solution ionic strength is increased [49]. These cochleates serve as efficient charge-transfer agents for photocatalysts in hydrogen production. Cochleate formation from liposomes of negatively charged phospholipids in the presence of multivalent cations also involves a nanoribbon intermediate [11, 12, 13]. Biocompatible phospholipid cochleates are being explored as drug-delivery agents because they can trap macromolecules, such as proteins, and DNA, and provide protection against degradation due to their multilayer geometry. Nanoribbons have also been observed in peptide amphiphiles (PAs), which consist of a sequence of amino acids covalently linked to an alkyl tail [52, 53]. For example, a peptide amphiphile that stimulates collagen production has been found to self-assemble into nanotapes with an internal bilayer structure [54]. In a PA with alternating charged and neutral amino acids, nanoribbons were found to transform into helical ribbons as the PA concentration was reduced [55] and into helical and twisted nanoribbons when the amino acid sequence was permuted [56]. Helical assemblies have been previously used to template semiconductor nanohelices [26]. Despite the progress, the correlation between experimental conditions such as molecular design, ionic strength, pH, amphiphile concentration, and the attained nanoribbon-related morphology are not fully established. Therefore, precise control of nanoribbon-related architecture requires further understanding of the delicate interplay between intermolecular interactions and elastic and interfacial energies.

A recent theoretical study showed that for charged molecules, tuning the range of electrostatic interactions could induce transitions between different nanoribbon-related morphologies [57]. Specifically, a phase diagram was deduced for a 2D lattice of charged points, which interacted via long-range repulsive electrostatic interactions and short-range attractive interactions. Planar nanoribbon to wavy ribbon with periodic undulations to helical ribbon transitions were predicted as the range of the electrostatic interactions is increased. This study suggests a facile method for accessing distinct nanoribbon architectures by varying the ionic strength (μ) of the solution because the range of electrostatic interactions as parametrized by Debye length (λ_D) scales as $\frac{1}{\sqrt{mu}}$. Recent experiments also attest that tuning the ionic strength leads to predictable changes in the nanoribbon-related assembly morphology. For example, the period of the twists in amyloid fibril aggregates monotonically decreases with decreasing ionic strength [21].

In this study, we analyze morphological changes in charged planar nanoribbons as a function of increasing ionic strength. In this regime, nanoribbon to cochleate transformations have been observed in phospholipids [13] and chromophore amphiphiles [49, 50, 58, 59]. However, the generality and the mechanistic details of this transition are still unknown. In particular, the correlation between the ionic strength induced changes in the molecular packing and the mesoscopic morphology transformations are elusive. The principal aim of this study is to start with a nanoribbon structure and experimentally trace the micrometer to angstrom length-scale transformations in the membrane structure as a function of ionic strength by using a combination of cryotransmission electron microscopy (cryo-TEM), liquid-atomic force microscopy (liquid-AFM), and in situ small- and wide-angle X-ray scattering (SAXS/WAXS). The experiments are coupled with theoretical models that qualitatively explain the observed morphological transitions.

We chose a simple peptide amphiphile (PA), $C_{16}K_{1}$, with a single ionizable amino acid lysine (K) covalently linked to a palmitoyl (C_{16}) alkyl tail (Figure 1.1A). This PA was chosen because our recent study [14] on $C_{16}K_{2}$ found spherical micelle to cylindrical micelle to a mixture of cylindrical micelle and nanoribbon transformations as the molecular charge was reduced by increasing the solution pH. Therefore, we hypothesized that removing one of the charged lysines from the headgroup could yield a macroscopic state consisting purely of nanoribbons. Second, the choice of this PA ensures that the interheadgroup interactions are Coulombic, unlike the case of PAs with multiple amino acids, where the assembly is strongly modulated by intermolecular hydrogen bonding.

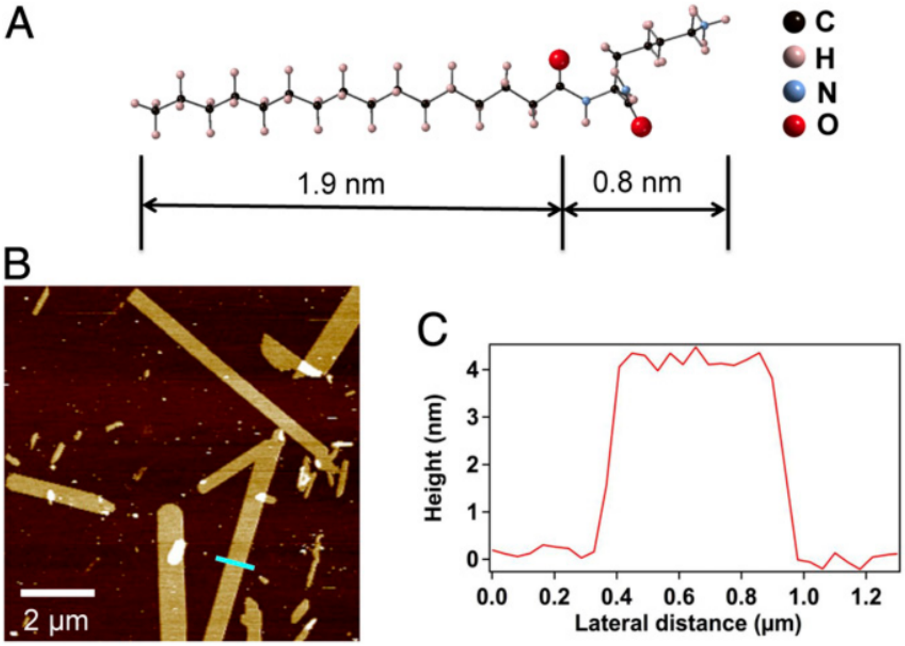

Figure 1.1: **A.** Molecular structure of +1 charged $C_{16}K_1$ with estimates for hydrophobic tail and hydrophillic headgroup lengths. The molecular conformation was derived from an MD simulation for a single $C_{16}K_1$ in water using the universal force field [60]. **B.** AFM image from a silica/water interface showing high aspect ratio $C_{16}K_1$ nanoribbons. **C.** The height profile across a $C_{16}K_1$ ribbon (green line in **B**).

1.2 Method Specifications

1.2.1 Peptide Synthesis

Peptides were synthesized using a CEM Liberty microwave-assisted peptide synthesizer. Standard fluoren-9-ylmethoxycarbonyl (Fmoc) solid-phase peptide synthesis was used with rink amide MBHA resin (100-200 mesh). For each coupling, 5 equivalents of Fmoc- protected amino acid (or palmitic acid) in DMF was added with 5 equivalents of N,N,N′,N′-tetramethyl-O-(1H-benzotriazol-1-yl)uronium hexafluoophosph-ate (HBTU) in DMF and 10 equivalents of N,N-diisopropylethylamine (DIPEA) in NMP. Fmoc removal was accomplished using a solution of 20% piperidine in DMF and 0.1 M 1-hydroxybenzotriazole (HOBt). Peptides were cleaved from the resin using a mixture of

95% trifluoroacetic acid (TFA), 2.5% water, and 2.5% triisopropylsilane for 3 h. Crude peptide was precipitated from this solution using cold diethyl ether. Purification was carried out on a Waters Prep 150 HPLC using a water/acetonitrile with 0.1% TFA solvent system and a Phenomenex Kinetex 30x150 mm C18 column. Eluting fractions were analyzed by Electrospray Ionization Mass Spectrometry (ESI-MS) using an Agilent 6520 Q-TOF LCMS before lyophilization and purity analysis by the same Agilent LCMS (water/acetonitrile with 0.1% formic acid solvent system and Phenomenex Proteo 100 × 1 mm column).

1.2.2 X-ray Scattering

SAXS/WAXS intensities (0.02 nm $^{-1}$ < q < 30 nm^{-1}) were collected simultaneously using three Rayonix CCD detectors at the 5ID-D undulator beamline of the Advanced Photon Source at Argonne National Laboratory. The beam size was 0.25 $\times$ 0.25 mm^2, and the incident beam intensity was $\sim$ 3 $\times$ 10^{11} photons/s. The sample solutions were injected through a capillary tube flow-cell (1.5 mm, quartz) at 2-5 mm/sec to reduce radiation damage. The capillary was embedded in a vacuum cell to avoid air scattering. A fast shutter was used to limit sample exposure to X-rays only during the data collection time (5-10 s for each measurement). For improving statistics, 5-10 measurements were made per sample. For background subtraction and for calibrating the intensities to an absolute scale, SAXS/WAXS patterns were also collected from the empty capillary and from the capillary containing pure water before measurements on every sample. The 2D SAXS/WAXS patterns were converted into 1D intensity profiles by azimuthal integration while taking into account the polarization, solid- angle and transmission corrections. The data were also normalized for the scan time. For absolute intensity calibration, the normalized and corrected scattered intensity profiles from pure water (difference of the scattering from capillary filled with water and the empty capillary) were fitted to straight lines. The intercept of these lines was set to 0.0165 cm $^{-1}$, the expected scattered intensity from water at q = 0 on an absolute scale at T = $25°$C. The data from the corresponding samples were thereafter scaled accordingly.

1.2.3 Cryo-TEM

Frozen hydrated samples were made by Vitrobot (FEI) and imaged at cryogenic temperatures. For preparing the samples, 3 μL solutions were deposited on TEM copper grids with holey carbon film (Ted Pella, Inc.). The sample was blotted 2 times for $\sim$ 6 seconds total before plunging into liquid ethane. A HT7700 (Hitachi) TEM with a bottom-mounted CCD camera (Orius) was operated at 100 kV to capture high-contrast micrographs. During the imaging process, samples were kept in a cryo-holder (Gatan 626) at -178°C. Raw images were processed using Image J.

1.2.4 AFM

A Bruker Bioscope Resolve was used to image the $C_{16}K_1$ membranes at the solid-liquid interface. Each sample was prepared by dropping 20 μL of 4 mM $C_{16}K_1$ solution onto a 1 $\times$ 1 cm ^{2} Si substrate, which was cleaned by piranha (3:1 H_2SO_4 : H_2O_2) solution. Bruker Scanasyst-Fluid+ probes were used for high-resolution imaging directly at the solid-liquid interface. Samples were scanned using the PeakForce Tapping mode with a peakforce frequency of 1 kHz. Raw images were processed through Nanoscope Analysis.

1.3 Results and Discussion

1.3.1 $C_{16}K_1$ Assemblies in Water

We first describe the $C_{16}K_1$ assembly in the absence of added salt. For this, L-$C_{16}K_1$ was dispersed in pure water at 4 mM concentration. Unless otherwise stated, the enantiomeric form of the amino acid [left-handed (L)] and the PA concentration (4 mM) are the same in all of the samples. The pH of this $C_{16}K_1$ dispersion was $\sim$4.6, which is much lower than the dissociation constant p$K \sim 7.6$ for $C_{16}K_1$ in their aggregates [61]. Therefore, under the experimental conditions, nearly all of the $C_{16}K_1$ are expected to be in their +1 ionized state.

The AFM image of $C_{16}K_1$ assemblies at a silica (SiO x)/water interface (Figure 1.1B) and other AFM images collected at different spots on the substrate reveal that in the absence of added salt,

$C_{16}K_1$ assembles into flat ribbons, with widths (W) in the range of a few hundred nm, lengths (L) ranging from 2 to 20 µm, and aspect ratio (L/W) as high as 30. All of the ribbons exhibit the same thickness of $\sim$4.0 nm, as shown by a representative AFM height scan (Figure 1.1C). This thickness is less than twice the length (5.4 nm) of fully extended $C_{16}K_1$ molecules (Figure 1.1A), suggesting that the $C_{16}K_1$ ribbons are bilayers with the alkyl tails of the 2 leaflets interdigitated. The interdigitated bilayer configuration, which has also been observed in $C_{16}K_2$ [14] and other PAs [55], is expected for molecules with headgroup cross-sectional areas much larger than that for the alkyl tails.

1.3.2 $C_{16}K_1$ Assemblies with Added NaCl

Screening effects are analyzed in $C_{16}K_1$ dispersions that contain NaCl at concentrations (c) ranging from 0 to 100 mM. Figure 1.2 A–D show AFM images of $C_{16}K_1$ assemblies at SiO_x /NaCl solution interfaces for $c = 0$, 1, 3, and 5 mM. Peak-force error images are shown as they deliver better 3D representation of the morphologies [62, 63]. With increasing NaCl concentration the ribbon aspect ratio decreases, and at $c = 3$ mM nearly isotropic sheets of 1 to 3-μm diameter are observed (Figure 1.2C). At or above this threshold concentration (c_{th}), the sheets roll into cochleates (Figure 1.2D). The multilayered nature of the scrolls is also observed in cryo-TEM images (Figure 1.2F). Overall, AFM and cryo-TEM show that increasing the ionic strength even over a narrow range first induces the ribbon to sheet to cochleate transitions.

We obtain ensemble-averaged, quantitative details of the mesoscopic morphology by SAXS and the molecular packing by WAXS in the ribbons and the cochleates. Figure 1.3 A and C show the background-subtracted SAXS and WAXS data for $C_{16}K_1$ ribbons in pure water with added NaCl, as a function of scattering vector magnitude $q = 4\pi sin(\theta)/\lambda$. Here, $\lambda = 0.827$ is the X-ray wavelength, and 2θ is the scattering angle. For $q < 0.4$ nm^{-1} (Figure 1.3A), the intensity $I \propto q^{-2}$ is indicative of structures with extended sizes in 2D, which is consistent with the AFM observation of flat ribbons with length and width both greater than $2\pi/q_{min} \sim 300$ nm, where q_{min} is the minimum accessible q in the measurements. Figure 1.3A (red) shows strong Bragg reflections in the range

14 < q < 16 nm^{-1} corresponding to $0.45 > 2\pi/q > 0.4$ nm distances, which are close to the diameter of the alkyl tails. Therefore, within the ribbons, the alkyl tails pack on a crystalline lattice such that the nearest-neighbor distances are commensurate with the tail diameter. A

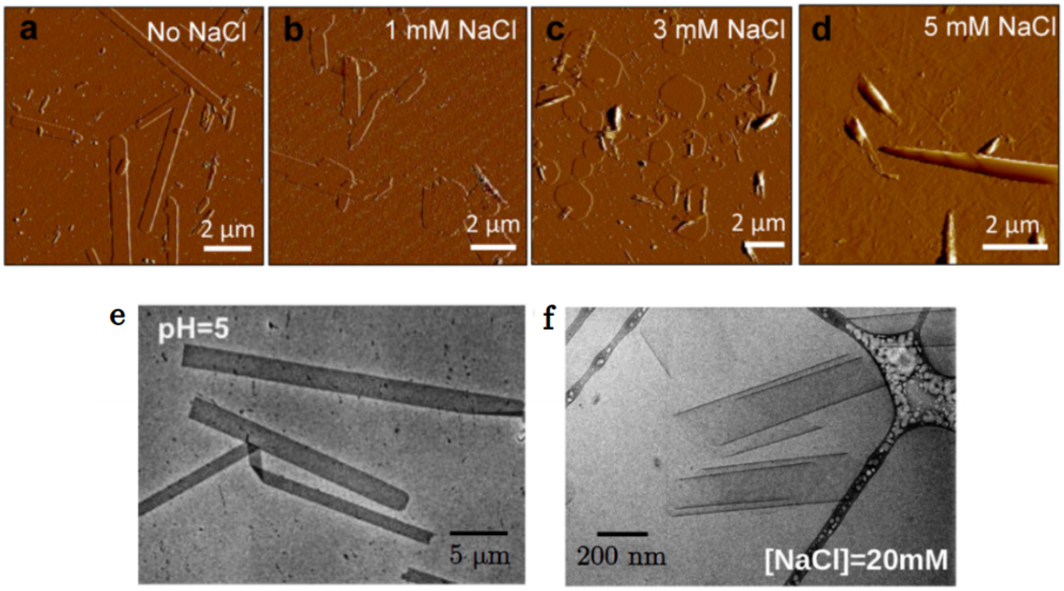

Figure 1.2: a-d AFM peakforce error images of drop-cast $C_{16}K_1$ membranes at SiO_x/NaCl solution interface. As NaCl concentration increases, structural transformations are observed from nanoribbon to isotropic sheet and to rolled-up cochleates, which exhibit a screw-like pitch. **e,f** Cryo-TEM images of bilayer ribbon with no added salt or NaOH (pH$\sim$5) and cochleate lamella at [NaCl] $=$ 20 mM.

We traced the ribbon to cochleate transformation and the changes in cochleates as a function of NaCl concentration via SAXS/WAXS. Figure 1.3A and C show X-ray scattering from 4 mM $C_{16}K_1$ at low (c = 1–5 mM) and high (c = 5–50 mM) NaCl concentrations, respectively. Figure 1.2A shows that for $c \geq 2$ mM and for $q < 0.1$ nm^{-1}, the monotonic fall in intensity is replaced by multiple intensity modulations due to cochleates. The SAXS-deduced NaCl concentration of 2 mM for ribbon to cochleate transition is only slightly lower than the threshold $c_{th} = 3$ mM in AFM experiments. Therefore, rolling of the membrane into cochleates is driven by the solution ionic strength; i.e., the range of intermolecular electrostatic interactions controls the ribbon to cochleate transition. Figure 1.2A shows intensity modulations across the entire q range of 0.02–25 nm^{-1} , which are divided into 4 groups, each yielding information at a different length scale: 1) the 0.02 < q < 0.06 nm^{-1}

modulation arises from the cross-section of the cochleates. If we assume the overall shape of a cochleate is a cylinder of radius R, then the scattering amplitude $F_{cyl}(q) \propto J_1(qR)/(qR)$ where J_1 is the first-order Bessel function of the first kind. The first zero of $J_1(qR)/(qR)$ occurs at $qR = 3.8$. Therefore, the minimum at $q \sim 0.022$ nm^{-1} yields an average cochleate radius $R = 3.8/0.022 \sim 173$ nm, which is consistent with the TEM image of the cochleates. 2) For 0.1 < q < 1 nm^{-1}, the intensity maxima positions follow the sequence $q_{max} : 2q_{max} : 3q_{max}$. Therefore, these modulations are Bragg reflections due to periodic lamella, with a spacing $D = 2\pi/q$ max within the cochleates. Based on q_{max} (Figure 1.3C) for 0.005 $\leq c \leq$ 0.1 M, $D(\text{nm}) = 6.40 + 2.05 \times c^{-1/2}$ (Figure 1.2D). That is, for the range of NaCl concentration used, the interlamellar spacing could be continuously tuned from 13 to 35 nm, and the interlamellar spacing varies linearly with the electrostatic screening length ($\lambda_D \propto c^{-1/2}$). Thus, the range of electrostatic interactions also controls the interbilayer spacing. 3) As noted in the SAXS analysis of ribbons, the broad intensity modulation for 0.8 < q < 3 nm^{-1} is due to an individual$C_{16}K_1$ bilayer. Figure 1.2A shows that the minimum position at $q \sim 0.9$nm $^{-1}$ shifts to a lower q when the ribbons are transformed into cochleates. This shift is observed up to $c = 4$ mM (Figure 1.2A,C), and is consistent with an increase in the bilayer thickness from 4.0 nm (ribbon) to 4.3 nm (cochleate) due to an increase in the thickness of the tail region. Thus, a curvature-induced strain in the cochleates reduces the extent of interdigitation between the bilayer leaflets. 4) The curvature also reduces the degree of order in the packing of $C_{16}K_1$ tails and headgroups. For the case of 4 mM $C_{16}K_1$, the sharp diffraction peaks corresponding to the crystalline ordering smear out for $c \geq$ 3 mM. Overall, X-ray scattering analysis reveals that above a threshold NaCl concentration of 2–3 mM, $C_{16}K_1$ assembles into cochleates. The interbilayer spacing within these cochleates depends linearly on the electrostatic screening length, and the curved morphology of the cochleates induces a reduction in the interdigitation between the bilayer leaflets and the crystallinity in the molecular packing.

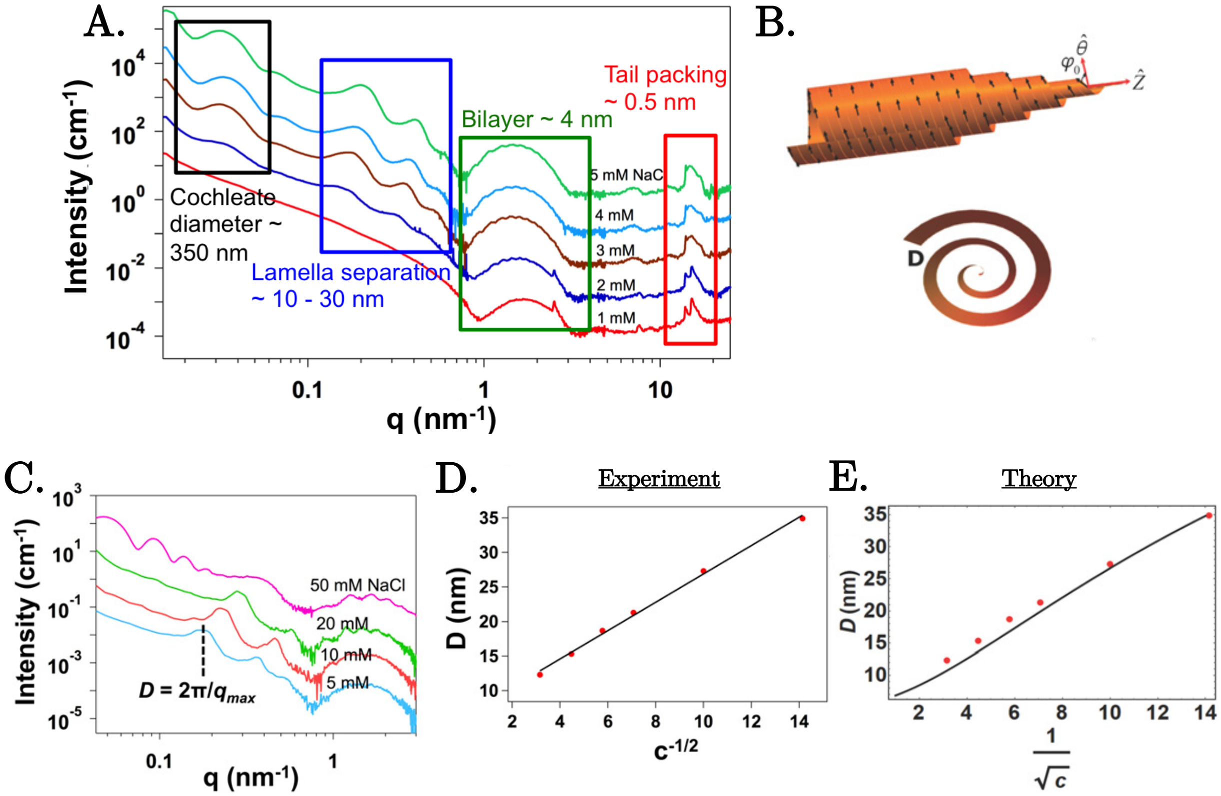

Figure 1.3: **A.** Background-subtracted in situ SAXS/WAXS data for 4 mM $C_{16}K_1$ as the NaCl concentration is increased from 1 to 5 mM. The datasets are offset vertically for clarity. With increasing NaCl concentration, the appearance of multiple intensity modulations for $q < 0.1$ nm^{-1} and the smearing of the sharp WAXS tail packing diffraction peaks are connected with the ribbon to cochleate transition. **B.** Cochleate surface coordinates used in modelling. Note the lamellar spacing D between each overlapping layer of the scroll-like structure in the cross section view of the cochleate. **C.** Background-subtracted in situ SAXS data for 4 mM $C_{16}K_1$ as the NaCl concentration is increased from 5 to 50 mM. The datasets are again offset vertically for clarity. The position of first-order small-angle diffraction peaks ($0.1 < q < 1$ nm^{-1}) is used to determine the interbilayer spacing D inside the cochleates. **D.** SAXS-derived interbilayer spacing in the cochleates varies linearly as a function of $c^{-1/2}$, where c is NaCl molar concentration. The solid black line is the best fit with equation: $D(\text{nm}) = 6.40 + 2.05 \times c^{-1/2}$. **E.** Theoretical fit to the interbilayer spacing using the Helfrich Prost model described in the text (see A.2 for more details).

1.3.3 Cochleate Chiral Assembly Energetic Model

We developed a theoretical model to rationalize the observed cochleate formation. Previous theoretical studies have shown that membranes of chiral molecules will experience an out-of-plane bending force [17, 32, 36] if the molecules are tilted with respect to the bilayer normal. Briefly, because of chirality, the molecules do not pack parallel to each other, but exhibit a twist with respect to their neighbors. This relative orientation constraint and the constraint of a preferred tilt angle with respect to the bilayer normal can be simultaneously satisfied by shapes exhibiting cylinder-like curvature, such as closed tubes. In qualitative agreement with these theories, SAXS/WAXS measurements show that at high salt concentrations, cochleates are formed for (left-handed) L- and (right-handed) D-$C_{16}K_1$ (Figure 1.4A). Under identical conditions, planar bilayers are observed for a racemic mixture (1:1 mixture of L- and D-$C_{16}K_1$) (Figure 1.4B). Furthermore, molecular chirality induces chirality in the assemblies at all length scales: At the nanoscale, the 2D lattice for tail packing is oblique ([61]), and at the mesoscale the cochleates have a screw-like handedness (Figure 1.2). For these reasons, we use the Helfrich–Prost model [36] to show that the combined effects of molecular chirality and tilt not only lead to helical ribbon and cylinder [17, 32, 36] morphologies, but can also stabilize the spiral-helicoidal shape of cochleates. This model also yields insights into the relationship between interbilayer separation in cochleates and salt concentration.

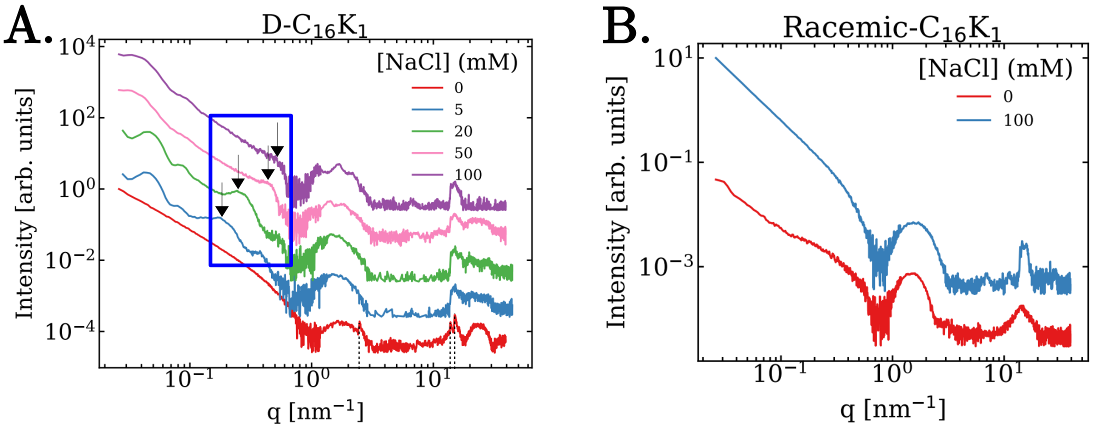

Figure 1.4: **A.** SAXS/WAXS from 4 mM solutions of D-C$_{16}$K$_1$ for 0-100mM NaCl. The data have been shifted vertically for clarity. SAXS/WAXS from assemblies of D-C$_{16}$K$_1$ in pure water exhibit sharp diffraction peaks at identical q positions as for L-C$_{16}$K$_1$ ($q =$ 2.5 nm^{-1}, 14<q<16 nm^{-1}, black dotted). These diffraction peaks originate from headgroup ordering and the packing of tails on an oblique lattice, respectively. In addition, intensity modulations due to the form factor of cochleates and diffraction peaks due to the periodic inter-bilayer separations within the cochleates are observed for both the D- forms of C$_{16}$K$_1$, which shift depending on the ionic strength of the solution in the same manner as L-C$_{16}$K$_1$ (black arrows). **B.** By contrast, the assemblies of racemic mixtures do not exhibit the diffraction peaks corresponding to the headgroup ordering; and only a broad diffraction peak at q ~15 nm^{-1}, likely due to short-ranged positional correlations between the alkyl tails, is observed. No intensity modulations from cochleate formation are observed for the solution containing the racemic mixture. For the racemic mixture, the intensity at low q falls monotonically as q^{-2} , implying that the assemblies are planar bilayers. Taken together, these measurements show that molecular chirality is essential for cochleate formation.

The scroll morphology (Figure 1.3B) resembles a spiral-helicoidal surface that can be parameterized as: $\boldsymbol{X}(\theta, z) = (D\theta \sin\theta, D\theta cos\theta, p\theta + z)$. Here, D is the sheet separation in the cochleate, and p is the pitch of the helical windings along the cochleate long axis. The relevant interactions for such a membrane are the elastic energy, the long-range electrostatic interaction, the short-range attractive van der Waals interaction, and the short-range hydration repulsion [64]. Based on SAXS/WAXS measurements, the aqueous layer thickness (D–δ) varies between ~31 and 9 nm when the salt concentration is varied between 5 and 100 mM. This thickness is much larger than the hydration decay length [64]. Therefore, the hydration energy term can be neglected. Besides, in a mean-field description, short-range attractive forces can be neglected [36, 65]. Theoretical arguments and experimental observations above suggest that lipid tilt and chirality are relevant in the membrane description. Thus, the energy for a cochleate can be written as: $H_T = H_F + H_S + H_B$. Here, H_F is the Frank interaction describing the increment in the energy due to the molecular reordering and distortions from their uniformly aligned configuration. H_S and H_B are the electrostatic and the bending energies, respectively. The electrostatic interactions H_S renormalize the physical properties of the membrane. In particular, the membrane bending rigidity changes as: $\kappa = \kappa_0 + \kappa_{el}(\lambda_D)$ [66]. Here, κ_0 is the intrinsic membrane bending rigidity and κ_{el} is an electric contribution that depends on the membrane geometry and the Debye length, λ_D . This electric contribution to bending has been experimentally verified for some lipid membranes [67]. Thus, the combined effect of bending and electrostatic energies can be written as $H_S + H_B \simeq \kappa \int dAK^2$. Here $K = \frac{2+\theta^2}{D(1+\theta^2)^{3/2}}$ is twice the mean curvature of the cochleate and $dA = D\sqrt{1+\theta^2}$ is the area element. If we assume that the molecules orient uniformly such that the tilt projection $\boldsymbol{m}$ in the local tangent plane forms an angle ϕ_0 with the azimuthal direction, then $\boldsymbol{m} = \cos\phi_0\hat{\theta} + \sin\phi_0\hat{z}$, where $\hat{\theta}$, $\hat{z}$ are the unit vectors in the azimuthal and axial directions (Figure 1.3B). Therefore, the Frank energy takes the simple form

$$\frac{H_F}{W} = \frac{\kappa'}{2}K^2\cos^2\phi_0 - \lambda_{HP}K\sin\phi_0\cos\phi_0 \tag{1.1}$$

Here, κ' is the difference between elastic constants for bending the membrane in the parallel and perpendicular directions to the tilt vector, and λ_{HP} measures the strength of the intermolecular chiral interactions [32, 36]. The minimization of the total energy H_T with respect to ϕ_0 predicts a critical tilt angle $\sec 2\phi_0 = -(2\kappa + \kappa')/\kappa'$. If the energetic costs of bending the membrane parallel or perpendicular to the tilt direction are almost the same, (i.e., $\kappa' \simeq 0$), then $\phi_0 \simeq 45^\circ$. This is roughly equal to the angle of the helical windings with the cochleate's principal axis suggesting that molecular tilt direction coincides with the membrane folding direction. This hypothesis needs further exploration. While the molecular tilt orientation is related only to the membrane elastic parameters, the interbilayer separation D depends on κ/λ_{HP} , i.e., the ratio of the membrane bending rigidity and the molecular chiral interaction parameter. In particular, D decreases nearly linearly with the Debye length for $R << \kappa/\lambda_{HP}$, where R is the cochleate external radius (Figure

1.3D). Furthermore, a theoretical curve approximately reproduces the D vs. λ_D experimental data (Figure 1.3E) (see A.2 for more details). The slight quantitative deviation between the experiment and theory (Figure 1.3D,E) is likely due to neglecting the stretching degrees of freedom and the thickness of the membrane. Nevertheless, the accuracy of the qualitative predictions of the model clearly highlights the collective effect of molecular tilt and chirality in inducing the spontaneous membrane curvature. This combined with the electrostatic effects, which rigidifies the membrane, enable us to deduce qualitatively the key structural features of the cochleates. In particular, this simplified theoretical model suggests that the linear relationship between the interbilayer separation and the electrostatic screening length is not a result of system-specific design, but of the interplay between electrostatic energy and the membrane internal degrees of freedom. Therefore, it is not surprising that similar linear relationships have been observed in other charged layered systems, such as clay mineral montmorillonite [68, 69]. We note that the linear relationship is not valid in the presence multivalent ions. For example, negatively charged phospholipid cochleates show little or no dependence of interbilayer spacing on the $CaCl_2$ concentration [70]. It is possible that the multivalent cations are tightly bound to the molecules resulting in interbilayer electrostatic interactions that cannot be parameterized by the screening length λ_D alone. By contrast, the use of monovalent salts to induce the $C_{16}K_1$ cochleate structure leads to tunable interbilayer spacing over $\sim$10–40 nm. This structural feature may have application for controlled encapsulation and release of drug particles within a specific size range.

Finally, we note that while the experimental results for cochleates are in qualitative agreement with the predictions of theoretical models for assembly of chiral molecules, there are still unresolved questions. First, these continuum models [17, 32, 36] are strictly applicable to fluid-like membranes or membranes with hexatic order. That is for cases where there are no long-range intermolecular positional correlations. However, the WAXS data from L- and D-$C_{16}K_1$ ribbons clearly show sharp diffraction peaks indicating crystalline bilayers (Figure 1.3A, Figure 1.4A). Second, membrane curvature is expected for cases where the molecules are tilted with respect to the bilayer normal. Our WAXS data are currently inconclusive in this regard.

1.4 Summary and Future Work

We designed a peptide amphiphile C$_{16}$K$_1$ to investigate the electrolyte-induced transformation of planar bilayers to scroll-like cochleates. We show that with the addition of NaCl, the high aspect ratio C$_{16}$K$_1$ ribbons formed in zero salt conditions transform to isotropic sheets, prior to rolling up to form cochleates. This ribbon to cochleate transformation also induces a reduction in the crystallinity in the molecular packing. Further addition of salt reduces, within the cochleates, the interbilayer separation, which scales linearly with the Debye length. Theoretical models show that rolling of membranes into cochleates is the combined effect of molecular chirality and tilt. The linear relationship between the interbilayer separation and the screening length in cochleates is qualitatively explained by the competition between electrostatic and the effective elastic interactions that include the internal degrees of freedom of tilt and chirality. These results suggest that the salt-induced structural transitions in the C$_{16}$K$_1$ system should be observed in other charged bilayer membranes. Our combined experimental and theoretical study yields insight into attaining the cochleate structures and controlling their internal architecture. These results should be useful for optimizing the structure and function of cochleates in many applications, including drug delivery and encapsulation of macromolecules.

Future work will focus on determining whether the molecules in bilayer have a small tilt or the molecules undergo a tilting transition just prior to the sheet to cochleate transformation. In addition, further control of the scroll-like cochleate structure will be explored by adjusting the levels of enantiomers in the cochleate assemblies. By combining left-handed and right-handed C$_n$K$_1$ molecules in solution, in principle, one can tune the degree of chiral coupling, λ_{HP}, that appears in A.14. Such tuning should lead to scroll-like cochleate of different morphologies.

2 Chapter 2

"*You take something you thought you knew and discover there's so much more to it than you could have possibly imagined.*"

-Corbin Creamerman

In this chapter we contrast the ribbon to sheet to cochleate transformation pathway of $C_{16}K_1$ molecular assemblies with added salt described in Chapter 1 with a ribbon to helical ribbon transformation of $C_{16}K_1$ (and generally C_nK_1) assemblies with increased pH. The different electrostatic environments and interactions of these two pathways are highlighted and discussed.

2.1 Introduction

Chiral molecules are ubiquitous in biology and synthetic chemistry. Examples include amino acids that constitute the proteins, lipids that constitute the cell membranes, and synthetic peptide amphiphiles. Molecular chirality is often manifested in fascinating mesoscopic chiral shapes (Figure 1A−D) such as helical ribbons and nanotubes with barberpole-like markings [2, 3, 4, 5, 6, 7, 8, 71], twisted ribbons [7, 8, 9, 10, 72], helicoidal scrolls (cochleates) [11, 12, 13, 73], and möbius strips [15]. Self-assembly in simple synthetic chiral molecular systems can provide insights into important biophysical processes. For example, helical ribbons and tubules observed in synthetic bile salt are analogous to chiral shapes observed in gallstone formation [24]. Furthermore, these soft chiral assemblies have potential nanotechnological applications that depend sensitively on the overall shape and nm-scale structural details of these assemblies. For example, helicoidal scrolls are being explored as drug/macromolecular delivery platforms due to their ability to encapsulate nanoscale objects within the bilayers (hydrophobic molecules) and in the aqueous phase between adjacent bilayers (hydrophilic molecules) [12]. Here, the bilayer thickness and the interbilayer separation should determine the size of the objects that such cochleates can trap and release. Helical ribbons and nanotubes are recognized as possible templates for nano- and meso-electronic components such as nanowires and solenoids [25, 26]. Clearly, the diameter and the helical pitch of these assemblies determine the nanowire properties and solenoid turn densities. For applications of helices and nanotubes, see excellent reviews, refs [5], [6], and [28], and references therein. These examples illustrate the need for developing control over shape selection, internal architecture of chiral assemblies, and interconversion mechanisms.

For membranes the origin of chiral shapes lies in the out of plane bending force that arises because a close packing of chiral molecules necessitates a relative twist between the neighboring molecules. This is qualitatively analogous to the case of packing of hard screws of a given handedness [16]. Theoretical studies based on continuum elasticity models show that simultaneous constraints of a preferred molecular tilt with respect to the membrane surface and the chirality-induced twist stabilize curved or bent membrane shapes such as open or closed helices [17, 32, 36], twisted ribbons [9], and scrolls [73]. While theoretical models include the tilt ordering, they exclude positional correlations, including crystallinity in molecular packing. This is despite experimental hints of an intricate coupling between molecular packing and chiral assembly. For example, a spherical vesicle is the equilibrium morphology for diacetylenic phospholipid membranes in the high temperature fluid phase (molten lipid tails, Lα-phase). By contrast, these same membranes in the low temperature condensed phase (tightly packed tilted lipid tails, Lβ'-phase) bend into chiral tubules [19]. Similarly, the assembly of a peptide amphiphile (N-α-lauryl-lysyl-aminolauryl-lysyl-amide) exhibits transformation from helical membranes to achiral spherical micelles when the temperature is raised above the chain melting transition temperature [74]. However, the effect of membrane fluidity or crystallinity on chiral assemblies is an unresolved issue [17]. In this context, the current study deals with chiral assemblies of crystalline membranes.

Attractive and repulsive interactions determine the details of molecular packing, and thereby indirectly modulate chiral assemblies. To illustrate, recent experimental studies have shown that electrostatic interactions can have profound effects on the chiral shape selection and structures. For example, zwitterionic phospholipids assemble into helices and nanotubes [3, 4, 19]. By contrast, cochleates have been observed for phospholipids that are negatively charged [11, 12, 13]. Similar is the case for peptide amphiphiles with ionizable amino acids [75]: tuning the molecular charge can induce a transformation between helical and twisted ribbons [20]. Furthermore, the range of electrostatic interactions controls the twist-pitch in amyloid peptide fibrils [21].

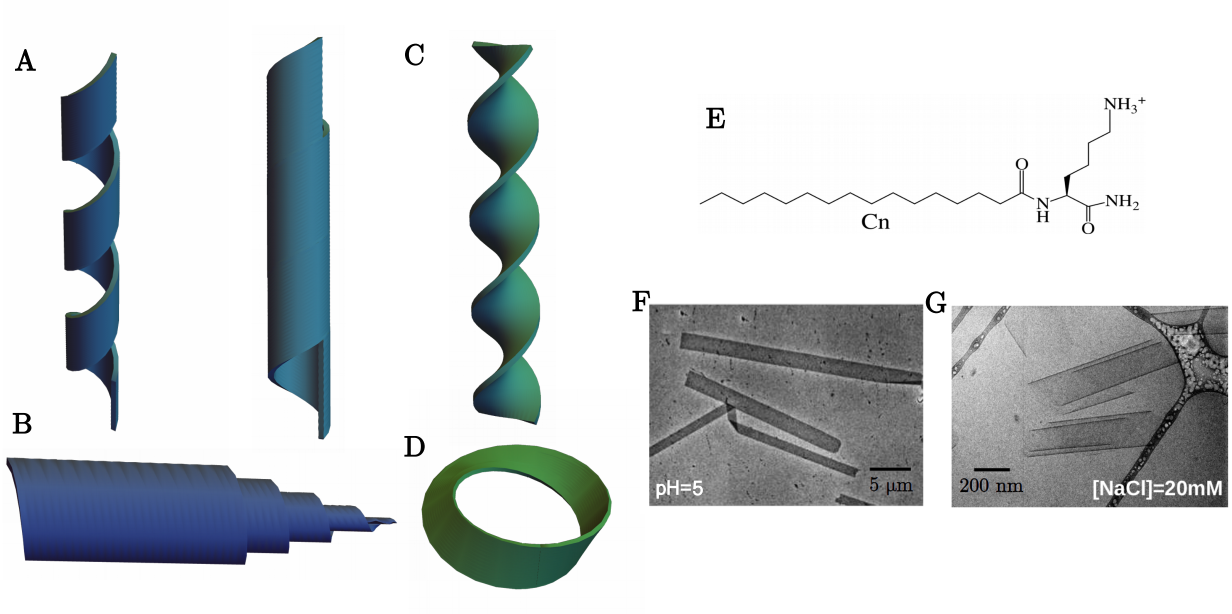

Figure 2.1: Schematics of chiral shapes: **A.** helical ribbon and closed helical tubule, **B.** cochleate (scroll-like), **C.** twisted ribbon, and **D.** möbius strip. **E.** Schematic for the molecular design for the homologous series of amphiphiles C_nK_1. **F.** TEM image of L-$C_{16}K_1$ flat ribbons and **G.** cryo- TEM cochleate structure for L-$C_{16}K_1$ in [NaCl] = 20 mM.

Despite the above-described progress, a clear understanding of the interconversion mechanisms between different chiral shapes and controls for nanoscale structures of chiral morphologies are lacking. This knowledge gap is likely due to a dearth of suitable molecular systems and theoretical models that enable exploration of the phase space of chiral shapes by systematically tuning the important intermolecular interactions. To address this, we designed a homologous series of amphiphiles C_nK_1 (Figure 2.1E) consisting of a single ionizable, chiral amino acid headgroup (lysine, K) that is covalently coupled to alkyl tails of varying lengths (n). We note here that lysine and polylysine amphiphiles, in particular, $C_{16}K_n$ (n = 1−3), have been explored in the context of antimicrobial properties [76]. However, in that study [76], no structural analysis of $C_{16}K_1$ assemblies was performed. The simple molecular design of C_nK_1 in the present work allows control over intermolecular electrostatic, van der Waals, and chiral interactions. For electrostatic interactions, the molecular charge can be tuned via pH. For very dilute solutions, the fraction of headgroups that are ionized (degree of ionization, $\alpha \equiv \frac{[NH_3^+]}{[NH_3^+]+[NH_2]}$) is expected to decrease with increasing pH according to $\mathrm{p}K_a = \mathrm{pH} - \log_{10}\frac{[NH_2]}{[NH_3^+]}$ where K_a is the reaction coefficient for the deprotonation of the lysine headgroup. The range of electrostatic interactions (screening length λ_D) can be controlled by salt concentration c via the electrostatic potential, which is of the form $V(r) \propto \frac{e^{-r/\lambda_D}}{r}$, $\lambda_D \propto \frac{1}{\sqrt{c}}$. We note that, in the very low salt concentration regime, the interaction is dominated by the long-range Coulomb potential $V(r) \propto 1/r$, and there is no theoretical work on charged chiral morphologies in this regime. The strength of the attractive van der Waals interactions can be tuned by the alkyl tail length, and in principle, the strength of the chiral interactions can be altered by producing binary mixtures with varied ratios of molecules with right- (D) and left-handed (L) lysines.

As a part of analyzing chiral assemblies by systematically varying the intermolecular interactions in the $C_{16}K_1$ molecular series, we recently reported on the $C_{16}K_1$ assembly behavior as the range of intermolecular electrostatic interactions λ_D was tuned from $\sim$10 to 1 nm by addition of salt ([NaCl] = 0.001−0.1 M) [73]. This study showed that under conditions where nearly all the lysines were expected to be ionized (+1, pH $\ll$ pK_a), $C_{16}K_1$ molecules formed high aspect ratio (L/W > 10), flat, crystalline bilayers. These bilayer ribbons transformed to sheets ($L/W \sim$ 1), which rolled up into helicoidal scrolls as the NaCl concentration was increased. Furthermore, the interbilayer spacing in the scrolls varied linearly with λ_D [73]. These results are reproducible, as demonstrated by transmission electron microscopy (TEM) images of the high aspect nanoribbons and cochleates observed in the newly synthesized batch of $C_{16}K_1$ that is used in the present work (Figure 2.1F,G). Here, we extend this work to analyze how the coupling between electrostatic and van der Waals interactions controls the chiral shape selection and internal structure. Specifically, we analyze assemblies for n = 12, 14, and 16 molecules as a function of the solution pH, that is, the average molecular charge. To be explicit, our previous report focused on enhancing the effects of chiral interactions by screening the intermolecular electrostatic interactions. In this work, the strength of electrostatic interaction is reduced by lowering the degree of ionization of the molecular headgroups, but the electrostatic interactions remain long-ranged.

2.2 Method Specifications

The C_nK_1 assembly structures were analyzed over µm to Å-length-scales by in situ small- and wide-angle X-ray Scattering (SAXS/WAXS), atomic force microscopy (AFM), cryo-transmission electron microscopy (cryo-TEM), and circular dichroism (CD). SAXS yields structural information about the overall shape as well as membrane characteristics (radius, bilayer thickness) and WAXS provides information regarding local molecular packing. AFM and Cryo-TEM allow for visualization of the assemblies and CD provides a direct probe into the chirality of the superstructures. In addition, titration was used to determine how the protonation state of the lipid molecules changes as a function of pH. Some details are provided below.

2.2.1 Peptide Synthesis

Peptides were synthesized using a CEM Liberty Blue microwave- assisted peptide synthesizer. Standard fluoren-9-ylmethoxycarbonyl (Fmoc) solid-phase peptide synthesis was used with rink amide MBHA resin (100-200 mesh). Each coupling was performed using 4 equivalents of Fmoc-protected amino acid or fatty acid, 4 equivalents of N,N'- diisopropylcarbodiimide (DIC), and 8 equivalents of ethyl(hydroxyimino)cyanoacetate (Oxyma pure) in DMF. Removal of the Fmoc groups was achieved with 20% 4-methylpiperidine in DMF and 0.1 M 1-hydroxybenzotriazole (HOBt). Peptides were cleaved from the resin using a mixture of 95% trifluoroacetic acid (TFA), 2.5% water, and 2.5% triisopropylsilane for 3 h. Crude peptide was precipitated from this solution using cold diethyl ether. Purification was carried out on a Waters Prep 150 HPLC using a water/acetonitrile with 0.1% TFA solvent system and a Phenomenex Kinetex 30$\times$150 mm C18 column. Eluting fractions were analyzed by Electrospray Ionization Mass Spectrometry (ESI-MS) using an Agilent 6520 Q-TOF LCMS before lyophilization and purity analysis by the same Agilent LCMS (water/acetonitrile with

0.1% formic acid solvent system and Phenomenex Proteo 100 × 1 mm column).

2.2.2 X-ray Scattering

SAXS/WAXS intensities (0.02 nm^{-1} < q < 30 nm^{-1}) were collected simultaneously using three Rayonix CCD detectors at the 5 ID-D undulator beamline of the Advanced Photon Source (APS) at Argonne National Laboratory. The beam size was 0.25 × 0.25 mm^2 , and the incident beam intensity was $\sim$ 3 × 10^{11} photons/s. The sample solutions were injected through a capillary tube flow-cell (1.5 mm, quartz) at 2-5 mm/sec to reduce radiation damage. The capillary was embedded in a vacuum cell to avoid air scattering. A fast shutter was used to limit sample exposure to X-rays only during the data collection time (5-10 s for each measurement). For improving statistics, 5-10 measurements were made per sample. For background subtraction and for calibrating the intensities to an absolute scale, SAXS/WAXS patterns were also collected from the empty capillary and from the capillary containing pure water before measurements on every sample. Additional SAXS/WAXS measurements were performed at 12 ID-C,D. At this APS beamline, data was collected using a Pilatus single photon counting area detector placed at a sample to detector distance (SDD) of 2.27 m. 15 or 17 keV X-ray were used with X-ray wavelength λ = 0.0827 or 0.0729 nm. The beamsize at the sample position was $\sim$ 0.4mm × 0.2mm and the flux was 2 × 10^{12} photons/s. An exposure time of $\sim$1 s was used.

The 2D SAXS/WAXS patterns were converted into 1D intensity profiles by azimuthal integration while taking into account the polarization, solid-angle and transmission corrections. The data were also normalized for the scan time. For absolute intensity calibration, the normalized and corrected scattered intensity profiles from pure water (difference of the scattering from capillary filled with water and the empty capillary) were fitted to straight lines. The intercept of these lines was set to 0.0165 cm^{-1} , the expected scattered intensity from water at q = 0 on an absolute scale at T = 25°C. The data from the corresponding samples were thereafter scaled accordingly.

2.2.3 Cryo-TEM

Microscopy was performed in the BioCryo facility at Nortwestern University with a Hitachi HT7700 tungsten emission TEM at 100 kV and data was collected on a Gatan Orius 2 k × 4.67 k digital camera. For sample preparation, 200-mesh Cu grids with a lacey carbon membrane were glow-discharged for 30 seconds in a Pelco easiGlow glow-discharger at 15 mA with a chamber pressure of 0.24 mBar. 4μL of 4 mM amphiphile solutions were then pipetted onto the grid and plunge-frozen into liquid ethane with an FEI Vitrobot Mark III cryo plunge freezing robot with 5 seconds of blotting and a blot offset of 0.5 mm. Grids were stored in liquid nitrogen until loaded into a Gatan 626.6 cryo transfer holder cooled down to -172°C.

2.2.4 TEM

Ex-situ TEM imaging was also performed on a HT7700 microscope, operating at 100kV. 1% Uranyl acetate solution was used as stain to increase image contrast. A small droplet of the sample solution (10 µL) was first placed on a TEM grid, and blotted after 3-5 min. Then a droplet of uranyl acetate solution (10 μL) was added on the grid, and blotted after 3-5 min. The grid was dried under ambient conditions for 2 h before transferring to the microscope.

2.2.5 AFM

Dimension FastScan AFM operating in tapping mode at 1-2 kHz frequencies was used to scan C$_n$K$_1$ assemblies drop-cast onto Si (1 0 0) substrates. Raw images were processed using Gwyddion. For preparing the samples, precut 1×1 cm^2 Si(1 0 0) substrates from MTI corporation were cleaned with Piranha solution (3:1 mixture of sulfuric acid and hydrogen peroxide). Substrates were then rinsed with copious amounts of ultrapure water (resistivity 18.2 MΩ·cm) and dried under a nitrogen stream. 20 μL of 4 mM amphiphile solutions were then pipetted onto the substrates and allowed to dry for 2-3 hours before AFM measurements.

2.2.6 Titration

5-6 mL solutions of 4 mM C_nK_1 were titrated with a 100 mM NaOH solution. The amphiphile and the NaOH solutions were freshly prepared in ultrapure water (resistivity = 18.2 MΩ·cm). The pH was measured using an Oakton pH 6 Acorn Series meter equipped with a Mettler Toledo micro electrode, which was calibrated at pH 4, 7 and 10 using buffers, prior to titration measurements.

2.2.7 CD

0.25-0.5 mM C_nK_1 solutions were prepared. 400 μL of amphiphile solution was placed in a 1 mm path-length cuvette. The Jasco J-815 Circular Dichroism (CD) Spectrophotometer instrument in the BioKeck facility at Northwestern University was then used to measure the absorption spectrum of the sample. Nitrogen was flowed at a rate from 45-60 ft^3 /hr (higher flow for deep UV region) to displace oxygen in the optical system such that the absorption of light by ozone formation is reduced. Raw data was processed using Spectra Manager Software.

2.2.8 MD Simulations

Classical all-atom explicit solvent molecular dynamics (MD) simulations were performed to study the nanoscale order of $C_{12}K_1$ and $C_{16}K_1$ flat bilayers. All simulations are performed and analyzed using GROMACS 2016.3 [77]. Additional analysis used the MDAnalysis python package [78, 79]. VMD and Pymol software packages allowed for visualization of simulation trajectories [80, 81]. The atomistic CHARMM 36 force field (March 2019) was employed to model C_nK_1 bilayers, which includes Coulomb electrostatic and Leonnard-Jones interactions [82] For simulations, all bonds containing hydrogen were constrained by the LINCS algorithm, which supported an integration time step of 2 fs. 180 lipid molecules were preassembled into bilayers using the packmol software and solvated with TIP3P water molecules [83] and Cl^- counterions for electroneutrality. All bilayer normals were oriented in the z direction. MD simulations were carried out using a rectangular box ($\sim 6 \times 6 \times 10$ nm^3) with periodic boundary conditions in x, y, z directions. The bilayer/explicit solvent system is equilibrated using the V-rescale modified Berendsen thermostat for temperature

(T=300 K). Pressure equilibration used Parrinello-Rahman semi-isotropic coupling with a reference value of 1 bar, compressibility of 4.5×10 -5 bar^{-1} , and characteristic time of 2 ps. After equilibration, C 16 -K bilayer production runs were carried out in the NPT (canonical) ensemble for 250 ns with a time step of 2 fs and semi-isotropic pressure coupling with the same Parrinello-Rahman coupling parameters. $C_{12}K_1$ production runs were 150 ns. Periodic boundary conditions were employed in all dimensions during production simulations. Electrostatic interactions are all calculated using the particle mesh Ewald (PME) method. Real space cut-off values for electrostatic and Van der Waal forces were 1.2 nm.

2.3 Results and Discussion

We first describe and discuss the assembly behavior of $C_{16}K_1$ as a function of solution pH. Thereafter, the generality of these findings is tested through the characterization of $C_{12}K_1$ and $C_{14}K_1$ assemblies.

2.3.1 Relationship between pH and Degree of Ionization for $C_{16}K_1$

To quantitatively relate pH and the degree of ionization (α), we titrated 5 mL of a 4 mM L-$C_{16}K_1$ solution in pure water with a 0.1 M NaOH solution (Figure 2.2A). This titration curve could be modeled with the empirical Hill equation (eq 2.1, see B.2) [84], which is a modified form of the Henderson−Hasselbalch (HH) equation (eq 1, $m = 1$ case) that works well for dilute solutions.

$$\alpha = \frac{1}{1 + 10^{m(\text{pH}-\text{p}K_a)}} \tag{2.1}$$

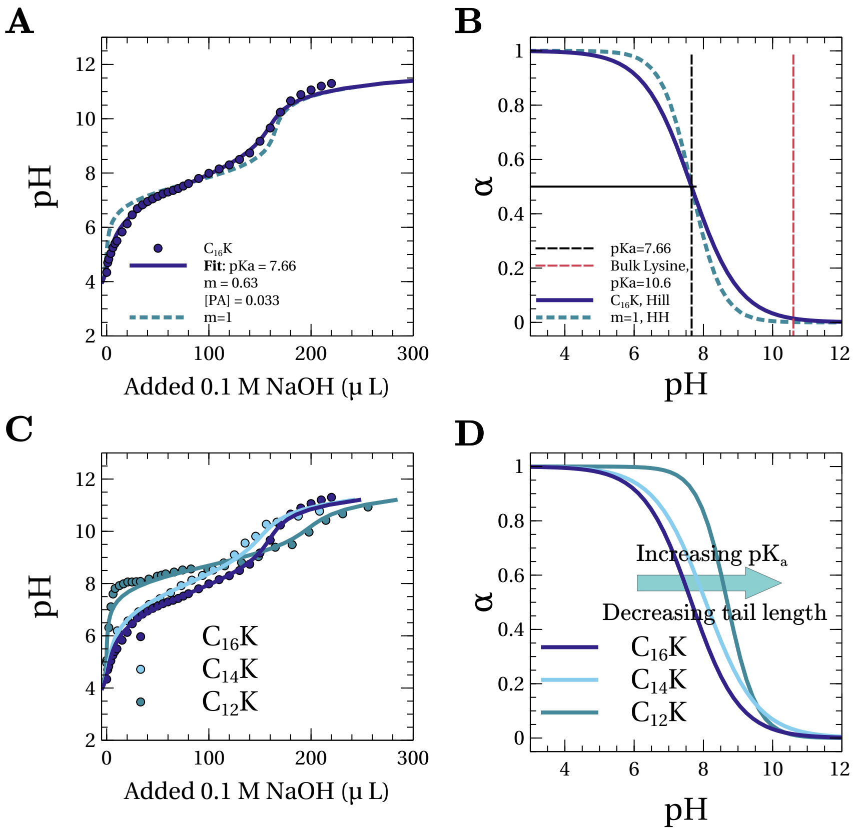

Figure 2.2: **A.** pH titration curve for a 4 mM L-$C_{16}K_1$ solution in 5 mL of pure water with a 0.1 M NaOH solution (circles) along with a fit based on the empirical Hill equation (solid blue curve). For comparison, also shown is a simulation with the Henderson−Hasselbalch (HH) equation (dashed light blue curve), with a pK_a that is identical to that derived from the Hill equation fit. **B.** Degree of ionization (α) vs pH, as derived from the fits based on the Hill equation (solid blue) and the HH equation (dashed light blue). As a reference, the pK_a values for L-$C_{16}K_1$ and free lysine are shown (dashed black and red lines, respectively). **C.** Measured titration curves for 4 mM C_nK_1 in 5 mL of pure water with 0.1 M NaOH. The data points are shown in circles and the Hill equation fits in solid lines. **D.** The degree of ionization vs pH for C_nK_1 that are deduced from the Hill model fits to the pH titration curves in **C.**

In eq 2.1, pK_a represents the center of the narrow pH window for the deionization of the molecular headgroups [α(pH = pK_a) = 0.5]. The parameter, m, determines the rate of change of the degree of ionization with pH. Therefore, m also determines the width of the aforementioned pH window. The best-fit values, p$K_a = 7.66$ and $m = 0.63$ (Figure 2.2B), indicate strong deviations from the dilute solution behavior and suggest that $C_{16}K_1$ molecules form tightly packed assemblies. To be explicit, (1) the fit value of $m = 0.63$ differs significantly from $m = 1$ (HH). This implies that the ionization and deionization of distinct molecular headgroups are not independent events. In particular, $m < 1$ reflects anticooperativity between molecules with regard to existing in identical ionization states [84]. (2) The p$K_a = 7.66$ is significantly different from the p$K_a = 10.54$ for free lysines [85]. This nearly 3 orders of magnitude shift in the acid−base equilibrium constant, which is qualitatively consistent with observations on assemblies of other charged amphiphile molecules [14, 86], implies a strong reduction in the tendency of the lysines in $C_{16}K_1$ to be ionized. Such charge regulation is expected because any arrangement of like-charged molecules in proximity increases the electrostatic potential energy of assemblies. The sought-after degree of ionization versus pH curve, which is derived from the best-fit parameters for the Hill equation, is shown in Figure 2.2B.

2.3.2 Chiral Assembly for $C_{16}K_1$ at Elevated pH

To test that the strategy of reducing the degree of ionization of the molecular headgroups leads to chiral assemblies, we performed circular dichroism (CD) spectroscopy on 0.5 mM solutions of right- (D) or left-handed (L) enantiomers or a racemic mixture of $C_{16}K_1$ (Figure 2.3A, right). For these measurements, pH $\sim$ pK_a ($\alpha \sim 0.5$, Figure 2.2B). In Figure 2.3A, $\Delta\epsilon = \epsilon_L - \epsilon_R$, where ϵ_L (ϵ_R) is the molar absorption coefficient for the left (right) circularly polarized light, and λ is the wavelength of light. The clearly observable CD signals for both L- and D-$C_{16}K_1$ in Figure 3A, right, show that the assemblies at pH $\sim$ pK_a are chiral. This contrasts with the flat crystalline bilayers observed at low pH$\ll$pK_a (Figure 2.1F). Furthermore, the handedness of these chiral assemblies is determined by the enantiomeric form of the molecules because the CD signals have opposite signs for L- and D-$C_{16}K_1$. The CD signal is nearly zero at all wavelengths for the racemic mixture (Figure 2.3A, right). The zero CD signal for the racemic mixture implies that either (1) the molecules phase-segregated such that each assembly consisted of molecules of only a specific handedness, that is, the solution consisted of an equal number of right- and left- handed assemblies, or (2) the right- and left-handed molecules coassembled to form achiral assemblies. SAXS measurements (Figure 2.7) revealed that the latter case holds true in the present study. In particular, the molecules assemble into stacks of flat bilayers for the racemic mixture. Finally, the CD spectra for L- and D-C$_{16}$K$_{1}$ is characterized by an absorption doublet at $\lambda \sim 200$ and 220 nm (Figure 2.3A, right).

Atomic force microscopy (AFM, Figure 2.3B) of a drop-cast 4 mM L-C$_{16}$K$_{1}$, pH = 8.5 (>pK_a) solution onto a Si (0 0 1) substrate showed right-handed helices of diameter ~ 250–300 nm (e.g., Figure 2.3B). Taken together, CD spectroscopy and AFM observations imply that the L-C$_{16}$K$_{1}$ (D-C$_{16}$K$_{1}$) flat bilayer ribbons twist into right- (left-) handed helices when the molecular degree of ionization is reduced by increasing the solution pH.

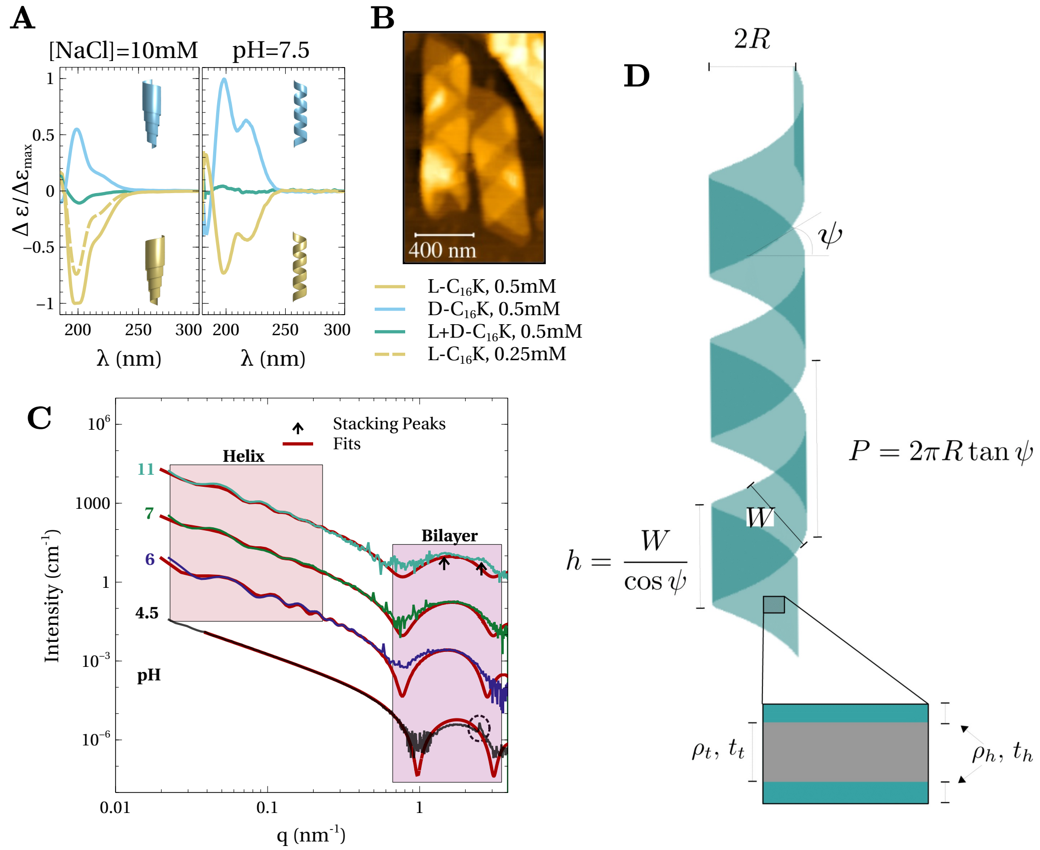

Figure 2.3: **A.** Circular dichroism spectra for C$_{16}$K$_1$ molecular assemblies in solutions with (1) pH $\sim$ pK_a (right) and (2) 10 mM NaCl and pH$\ll$pK_a (left). Insets show schematics of the chiral shapes derived from cryo-TEM or AFM measurements. **B.** Ex situ AFM image of C$_{16}$K$_1$ assemblies at pH $\sim$ 8.5 that were drop-cast and dried on a Si (1 0 0) substrate. **C.** In situ SAXS intensity profiles for 4 mM L-C$_{16}$K$_1$ assemblies in solutions at 4 different pH. The data for pH 6, 7, and 11 are scaled for clarity. Also shown are fits (red line) based on a planar bilayer (pH = 4.5) or helix (pH=6, 7, 11) models. **D.** Schematics of the helix model used to fit data. Left side shows a bilayer membrane that is twisted into a helix parametrized by three independent parameters. For example, the radius (R), the helix angle (ψ), and the width (W). Right side shows a cross-section of the bilayer membrane.

We note that the same correlation between the molecular enantiomeric form and the handedness of the assemblies was deduced for helicoidal scrolls formed in saline solutions by combining CD spectroscopy (Figure 2.3A, left) and AFM [73] and cryo-TEM (Figure 2.1G). Previous theoretical [87] and experimental [88] studies have shown that molecules of a given enantiomeric form can assemble into either right- or left-handed meso-shapes. This selection is determined by the coupling between the chiral interactions and the direction of the molecular tilt [87]. Cochleates (Figure 2.1G) and helices (Figure 2.3B) originate from the same C$_{16}$K$_1$ bilayer membranes (Figure 2.1F) in distinct ionic conditions. Therefore, the observation of the same handedness of the meso-shapes for a given molecular enantiomeric form is expected. The key result here is that achiral electrostatic interactions strongly affect chiral shape selection. Reducing the screening length by adding salt leads to cochleates. By contrast, reduction in the strength of electrostatic interactions through controlling the degree of ionization produces helices. Finally, we note that temperature-dependent CD spectroscopy (Figure 2.4) suggests that ordering/crystallinity in molecular packing is essential for the formation of the observed mesoscopic chiral shapes. In particular, the CD signal for helicoidal scrolls (Figure 2.3A, left) vanishes above $T \sim 60°C$ (Figure 2.4), which is within the observed range of chain melting transition temperatures for C$_1$$6$ tails that are coupled to charged headgroups [89]. This requirement of crystalline packing of alkyl tails is consistent with the examples of diacetylenic phospholipid [19] and peptide amphiphile (N-α-lauryl-lysyl-aminolauryl-lysyl-amide) [74] membranes discussed above. The details of the molecular packing for C$_{16}$K$_1$ membranes are deduced via X-ray scattering and MD simulations (discussed later).

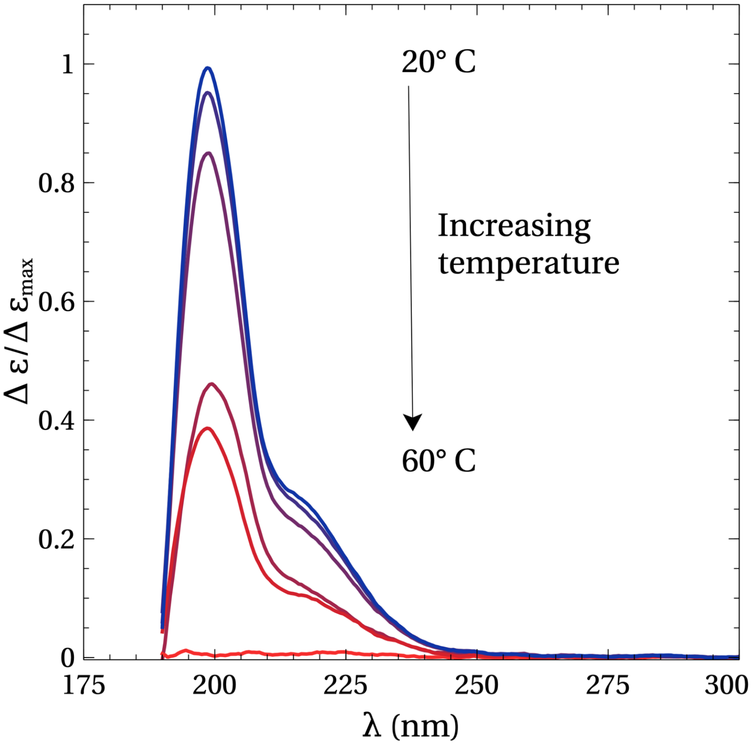

Figure 2.4: Temperature-dependent CD spectra for D-$C_{16}K_1$ molecular assemblies in a solution with 10 mM NaCl. The CD signal vanishes for $T = 60°$C.

2.3.3 Evolution of $C_{16}K_1$ Assembly Structure with pH

In situ small-angle X-ray scattering (SAXS) was utilized to analyze the structural evolution of the $C_{16}K_1$ assemblies as a function of pH. Figure 2.3C shows the background-subtracted SAXS intensity profiles as a function of the scattering vector magnitude $q = \frac{4\pi}{\lambda}\sin\theta$ for 4 mM L-$C_{16}K_1$ at pH = 4.5, 6, 7, and 11, which correspond to α = 0.99, 0.92, 0.72, and 0.008, respectively. Here, λ is the X-ray wavelength and θ is one-half of the angle between the incident and the scattered X-rays.

For pH = 4.5 (Figure 2.3C, bottom), the intensity profile is consistent with planar, interdigitated bilayers with crystalline ordering in the packing of the molecular headgroups and tails. This is because (1) for low q (<0.4 nm −1), the scattered intensity drops off monotonically as $I(q) \propto q^{-2}$. The Porod exponent of −2 is consistent with planar objects (Figure 2.1F) with both the lateral dimensions larger than $\frac{2\pi}{q_{min}} \sim 200$ nm [39]. Here, q_{min} is the smallest accessible q in our measurements. (2) Fitting the intensity profile with a bilayer model [90] reveals that the broad intensity modulation in the 0.8 nm^{-1} < q < 3 nm^{-1} is due to a 3.82 nm thick bilayer. The thicknesses of the hydrophobic tail and the hydrophilic headgroup regions were determined to be $t_t = 2.30$ nm and $t_h = 0.76$ nm. (3) The intensity profile shows sharp diffraction peaks in the SAXS (at $q \sim 2.5$ nm^{-1} , Figure 2.3C, dashed black circle) and the wide-angle X-ray scattering [(WAXS), $q > 10$ nm^{-1}] regimes (Figure 2.5A, inset). These diffraction peaks originate from crystalline ordering in the packing of the headgroups and molecular tails. We note that the expected length for a C_{16} alkyl tail in stretched trans-configuration is (16 − 1) $\times$ 0.127 nm ~ 1.9 nm [91]. Therefore, $t_t = 2.3$ nm is substantially lower than the expected length of 1.9×2 nm for two C_{16} tails. This is due to the interdigitation of the tails from the two bilayer leaflets, as demonstrated by our molecular dynamics (MD) simulations (discussed later).

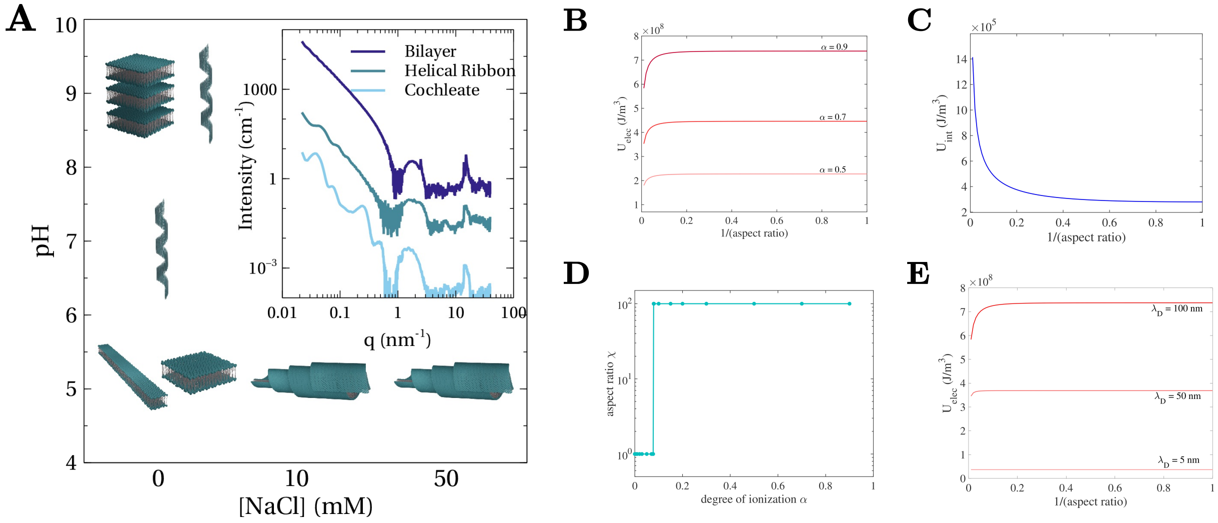

Figure 2.5: **A.** Structural phase diagram for C$_{16}$K$_1$ assemblies as a function of salt concentration and pH. The inset shows the characteristic SAXS/WAXS intensity profiles for planar bilayers, helices, and cochleates. Note that the SAXS patterns from the cochleates show diffraction peaks in the SAXS regime from membrane stacking ($q \sim 0.25$ and ~ 0.5 nm^{-1} in the above example). **B.** The variation of the rectangular membrane electrostatic energy density as a function of aspect ratio χ for different degrees of ionization α at a fixed $\lambda_D = 100$ nm. **C.** Interfacial energy density as a function of χ. **D.** Aspect ratio corresponding to the minimum total membrane energy as a function of α. **E.** Membrane electrostatic energy density as a function of χ for three different screening lengths (λ_D), which correspond to the cases of NaCl concentrations of ~10 μM, 40 μM, and 5 mM (top to bottom). For these calculations, $\alpha = 1$. The numerical calculations (**B**−**E**) were carried out for aspect ratio range: $100 \geq \chi \geq 1$, which encompasses the experimentally observed range ($\chi \sim 10 - 30$) for bilayer ribbons (example, Figure 2.1E). For degree of ionization $>\sim 0.07$, the membrane energy was found to be minimized for the highest $\chi (= 100)$ used in the calculations **D.**

In contrast to the planar bilayer case (pH = 4.5), the intensity profiles at elevated pH show multiple modulations in the low q (< 0.8 nm^{-1}) region (Figure 2.3C). For helical bilayer ribbons, the period of these modulations is primarily determined by the helix radius R. Furthermore, for a given R, the absolute positions and the amplitude of these modulations depend sensitively on the pitch angle ψ and the ribbon width W (see Figure 2.6). Additionally, for the pH = 11 case, where most of the molecules are expected to be in the deionized state (α = 0.008), the intensity modulation due to bilayer thickness (0.8 nm^{-1} $< q < 3$ nm $^{-1}$) exhibits a nearly flat top with two shallow maxima (weak diffraction peaks, Figure 2.3C, black arrows). These diffraction peaks arise due to membrane stacking. Therefore, we interpret that the C$_{16}$K$_1$ assembly at pH = 11 comprises of a mixture of multiple stacks of bilayers and helical ribbons. This reorganization of membranes into multilamella will become apparent when discussing later the assembly in C$_{12}$K$_1$ and C$_{14}$K$_1$ as for those cases, the stacking peaks are pronounced in the scattering profiles (Figure 2.8C). These observations imply that C$_{16}$K$_1$ assemblies transform from isolated high aspect ratio bilayers to helices to stacked membranes as the degree of ionization is reduced via pH.

We first ignore the stacking aspect and describe the fitting of the SAXS intensity profiles at pH = 6, 7, and 11 based on a helical bilayer membrane model depicted in Figure 2.3D. The scattered intensity from helices is distributed as cylindrical Bessel functions on reciprocal space planes defined by $q_{||,n} = \frac{2n\pi}{P}$ [92]. Here $q_{||,n}$ is the scattering vector component parallel to the helix axis and P is the helix pitch. We have analyzed the measured scattered intensity from helical ribbons using the multilayer helical membrane form factor, which is an extension of the Pringle and Schmidt model [92, 93]. Furthermore, we have taken into account polydispersity in helix size (eqs 2.2 and 2.3).

$$I(q) \propto \Big\langle \Big[\frac{(lh)^2}{qP}\Big] \sum_{n=-\infty}^{\infty} \text{sinc}^2\Big(q_{||,n}\frac{h}{2}\Big) G(q, R, t_b, t_t)^2 \Big\rangle_{\text{poly}} \tag{2.2}$$

Here,

$$G(q, R, t_b, t_t) = (\rho_h - \rho_s) \int_{R-t_b/2}^{R+t_b/2} r J_n(r\sqrt{q^2 - (q_{||,n})^2}) dr + (\rho_t - \rho_h) \int_{R-t_t/2}^{R+t_t/2} r J_n(r\sqrt{q^2 - (q_{||,n})^2}) dr \tag{2.3}$$

In eq 2.2, l is the number of turns in the helical bilayer membrane, h is the membrane width along the helix axis, t_b is the bilayer thickness and t_t is the thickness of the hydrophobic tail region (Figure 2.3D). In eq 2.3, ρ_h and ρ_t are the electron densities for the headgroup and hydrophobic tail regions of the amphiphilic bilayer, ρ_s is the solvent electron density, R is the mean radius, J_n are

Table 2.1: SAXS-Derived L-$C_{16}K_1$ Helix Parameters

pH	R (nm)	ψ(deg)	W (nm)	h/p	% polydispersity [1]
6	62.6	29.3	115.6	0.59	5.5
7	69.6	31.9	128.1	0.56	8.7
11	78.2	39.5	189.3	0.61	10.7

the n^{th} order Bessel functions of the first kind and $q_\perp, n = \sqrt{q^2 - (q_{||,n})^2} \geq 0$ is the scattering vector component normal to the helix axis. Size dispersity (eq 2.2) is taken into account by averaging over bilayer helical ribbons of 10 different equally spaced radii in the range $R \pm (\text{\% polydispersity})/100)R$. Finally, the summation in eq 2.2 was found to converge through inclusion of terms within $n = \pm 3$.

The SAXS data for helical bilayer membranes has two key features. Quasi-periodic intensity modulations in the low q ($\sim$ < 0.5 nm^{-1}) regime that arise from the helix shape and the broad intensity modulation spanning the $q \sim 0.8 - 5$ nm^{-1} region due to the bilayer structure of the amphiphilic membrane. The fitting of the SAXS data from helical bilayer ribbons was done in two steps.

First, the low q (≤ 0.4 nm^{-1}) data was fitted using equations 2.2 and 2.3 (main text) to estimate the parameters radius R, height/Pitch (h/P) and helix angle ψ that completely define the finite width helix. The parameter, corresponding to radius polydispersity was also optimized concurrently. This fit was done using the genetic algorithm for global optimization within the statistical toolbox of MATLAB.

Second, fitting over the extended q range encompassing the helix and bilayer intensity modulations was again performed using 2.2 and 2.3 (main text), but for this step Trust Region Reflective algorithm for local optimization within the statistical toolbox of MATLAB was used. Here, the helix parameters were allowed to vary only by $\pm$ 15% of the best-fit values in the first step. The parameters corresponding to the bilayer were also similarly bound by constraints about the best-fit values for the electron densities and the thicknesses of the headgroup and the tail regions (ρ_h, ρ_t, t_h, t_t) obtained by fitting the SAXS data from planar membranes at low pH for $C_{16}K_1$ case. For $C_{14}K_1$

---

[1] For parameter definitions, see Figure 2.3D. The case $h/P = 1$ corresponds to nanotubes with helical markings, and $h/P < 1$ corresponds to open helices. Bilayer parameters were fixed as $t_h = 0.75$ nm, $t_t = 2.3$ nm, $\rho_h = 430$ e/nm^3 , and $\rho_t = 307$ e/nm^3.

and $C_{12}K_1$, the constraints were relaxed on the parameter t_t for the tail thickness. The two-step approach was utilized because the global optimization over the extended q-space was found to be very slow. In both the steps, the optimal parameter values were obtained by minimizing the function:

$$F = \sum_{k=1}^{n} \left[\frac{I_{meas,k} - I_{fit,k}}{I_{meas,k}} \right]^2 \tag{2.4}$$

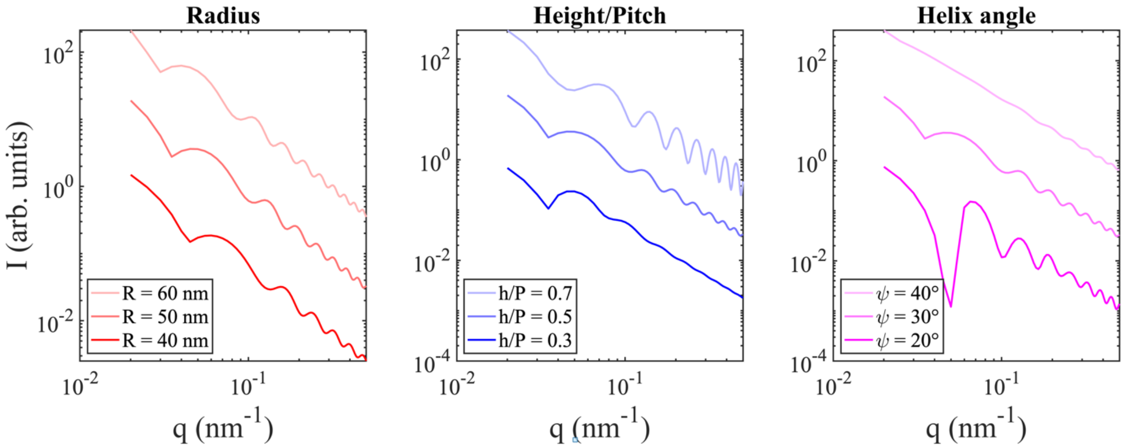

Figure 2.6: Simulated intensity profiles showing the sensitivity of SAXS to parameters defining a finite width helix. Intensity profiles for 3 different radius R at fixed height/pitch, $h/P = 0.5$ and a helix angle $\psi = 30°$ (Left), 3 different h/P for fixed $R = 50$ nm and $\psi = 30°$ (Center), and 3 different ψ for $R = 50$ nm and $h/P = 0.5$ (Right). For these low q simulations, the bilayer thickness was taken to be zero. We note that the finite width helix can be defined completely by 3 independent parameters such as radius R, width W and helix angle ψ. The parameter h/P was chosen instead of parameter W because it directly reflects how open is the helix. Furthermore, h/P appears as the argument of the sinc function in the helix form factor (eq 2.2, main text). Based on these simulations, it is clear that the helix radius dictates the intensity modulation frequency, which increases with increasing radius (Left). This is expected based on the analogy of diffraction from circular apertures of different radii. The amplitude as well as the absolute positions of minimum and maximum in the intensity profile are modulated by h/P and ψ The effect is coupled, but based on the above shown and other simulations it becomes clear the amplitude of the oscillations increases with h/P, that is the amount of material in the ribbon (Center). The amplitude is maximum for $h/P = 1$, which corresponds to the case of a nanotube.

Figure 2.3C shows the measured intensity profiles along with fits based on the helical bilayer membrane model (eqs 2.2 and 2.3). The best fit parameters are listed in Table 2.1 the effect of the parameters on a scattering profile are illustrated in Figure 2.6. This analysis shows that the helix radius increases monotonically as the degree of ionization is reduced by increasing the pH. Note that the SAXS-extracted helix radii (Table 2.1) are smaller than the AFM-derived radii (Figure 2.3B) by a factor of 1.5−2. This is likely because the dried-out helices in the ex situ AFM measurements were in a collapsed state. This collapse effect has been observed also for phospholipid helices and nanotubes [3]. If the helices completely flatten on drying, then the apparent radius in AFM is expected to be larger than the real radius by a multiplicative factor of $\pi/2$ [3]. This explains the discrepancies between our SAXS and AFM measurements. Overall, our studies on $C_{16}K_1$ assembly in varied ionic environments clearly demonstrate that electrostatic interactions (1) play a key role in shape selection of chiral assemblies and (2) can be systematically varied to continuously tune the nanoscale structure of the chiral assemblies. The first result is based on the observation of helicoidal scrolls in saline solutions and helices under elevated pH conditions, where the molecular degree of ionization was diminished. These observations are summarized in a structural phase diagram in Figure 2.5A. The second result is based on the observation that the helix radius monotonically increases with increasing pH (Table 1). We speculate that both these results can be explained by the electrostatics-driven changes in the shape of the planar membranes, from which these assemblies are derived.

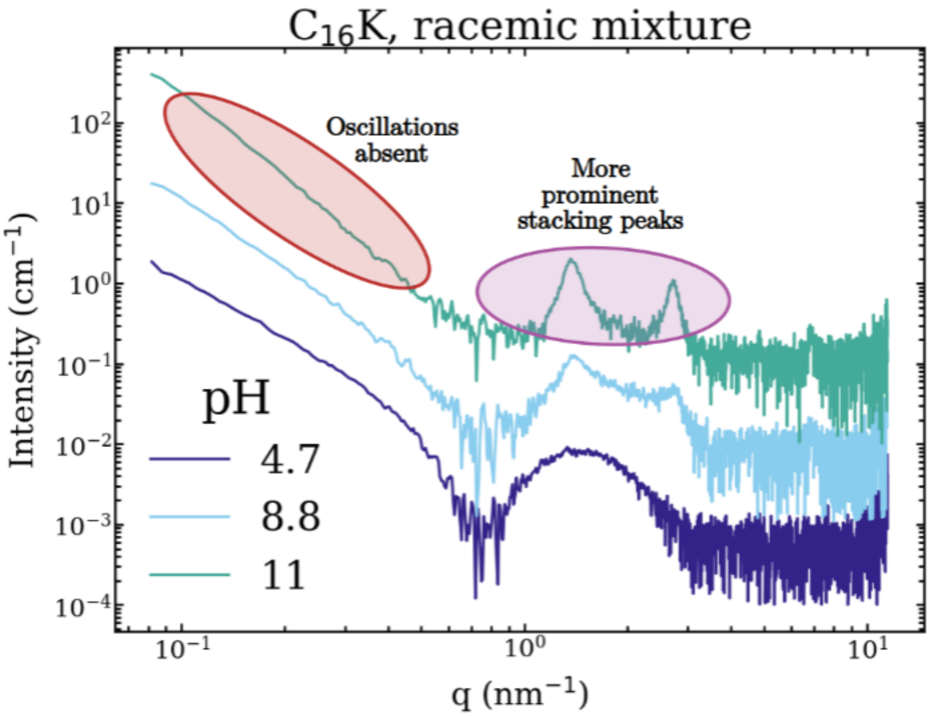

Figure 2.7: SAXS intensity profiles from 4 mM dispersions of 1:1 mixture of L-$C_{16}K_1$ and D-$C_{16}K_1$ at 3 different pH. For pH = 4.7 (Figure 2.7, bottom) , the intensity profile is consistent with planar bilayers. This is similar to the L-$C_{16}K_1$ case. However, in comparison to the intensity profiles from pure L-$C_{16}K_1$ (Figure 2.5A), the SAXS data from the racemic mixture at elevated pH (= 8.8, 11) do not exhibit any periodic intensity modulations in the low q (< 0.8 nm^{-1}) regime that are a signature of helical ribbons. Instead, the SAXS data from the racemic mixture shows more prominent diffraction peaks due to planar membrane stacking. These observations show that in 1:1 mixtures, the L- and D- molecules mix to form only achiral assemblies such as planar bilayers or stacks of the planar bilayers.

2.3.4 Model for Chiral Shape Selection

To explain chiral shape selection, we develop a simplified model for planar membrane energetics (eq 2.5, see A.1) and combine it with an elementary geometric argument that helices can only be formed if the aspect ratio of the planar membranes exceeds a critical value.

$$\frac{H_{\text{memb}}}{V} = U_{\text{elec}} + U_{\text{int}} = 2\frac{N_T^2}{VA}k_B T l_B \lambda_D \int\int_{0,0}^{L/\lambda_D, W/\lambda_D} \frac{e^{-\left(\sqrt{\frac{x^2+y^2}{\lambda_D^2}}\right)}}{\sqrt{\frac{x^2+y^2}{\lambda_D^2}}} dxdy + 2\gamma\left(\frac{L+W}{A}\right) \quad (2.5)$$

Equation 2.5 describes the model for rectangular charged membranes. Here, the membrane energy density $\left(\frac{H_{\text{memb}}}{V}\right)$ consists of intermolecular electrostatic repulsions (U_{elec}) and the interfacial energy (U_{int}) due to the exposure of hydrophobic tails on the membrane edge surfaces to the aqueous solvent. In eq 2.5, short-ranged interactions such as intermolecular van der Waals attractions and hydrogen bonding are ignored because such interactions, while critical for assembly, do not influence the mesoscopic membrane shape. In eq 2.5, N_T is the total membrane charge. V and A are the membrane volume and surface area, respectively. k_B is Boltzmann's constant, T is the absolute temperature, and l_B and λ_D are the Bjerrum length and the electrostatic screening length, respectively. L and W are the membrane length and width, respectively. The model parameters used in the numerical calculations are listed in A.1 and the results are illustrated in Figure 2.5B−E.

Figure 2.5B shows that the membrane electrostatic energy is minimized for high aspect ratio (quasi-1D) bilayers. This is because a 1D molecular arrangement results in larger next nearest, next−next nearest neighbor distances and a smaller number of nearest, next nearest, and so on neighbors, as compared to the case of a 2D membrane. By contrast, minimization of the interfacial energy is achieved for an aspect ratio $\chi = L/W = 1$, because for this aspect ratio, the membrane has the smallest perimeter for a fixed area (Figure 2.5C). Thus, the contact between the hydrophobic tails and the aqueous solvent is minimized for $\chi = 1$. For a wide pH range, when the degree of ionization α ($\propto N_T$) is sufficiently high ($>\sim 0.07$), the magnitude of the electrostatic energy is greater than the interfacial energy. Therefore, the membranes are expected to exhibit a high aspect ratio (Figure 2.5D). At very high pH, when the vast majority of the molecules are in the deionized state, the interfacial energy dominates, and the membranes transform to sheets with $\chi = 1$ (Figure 2.5D).

The above argument is consistent with the observation of helical membranes over a wide pH $\sim$ 6−11 range. This is because only high aspect ratio membranes, expected in this pH regime, can twist into helices. It can be readily shown that for a helix with l turns, the membrane aspect ratio should exceed a critical value: $\chi = L/W \geq 2l$. This relationship follows from noting that the helix pitch $P = 2\pi R tan\psi \geq h = W/cos\psi$ (Figure 2.3D), and the helix contour length $L = 2\pi Rl/cos\psi$. By contrast, at very high pH (≥ 11) the interbilayer electrostatic repulsions are very weak for the nearly deionized membranes with $\chi = 1$, and short-ranged intermembrane attractions drive the assembly into lamellar stacks. Note that the numerical calculations in Figure 2.5D suggest that this transition between helical and stacked membranes is exceedingly sharp and occurs at a critical degree of ionization (or pH).

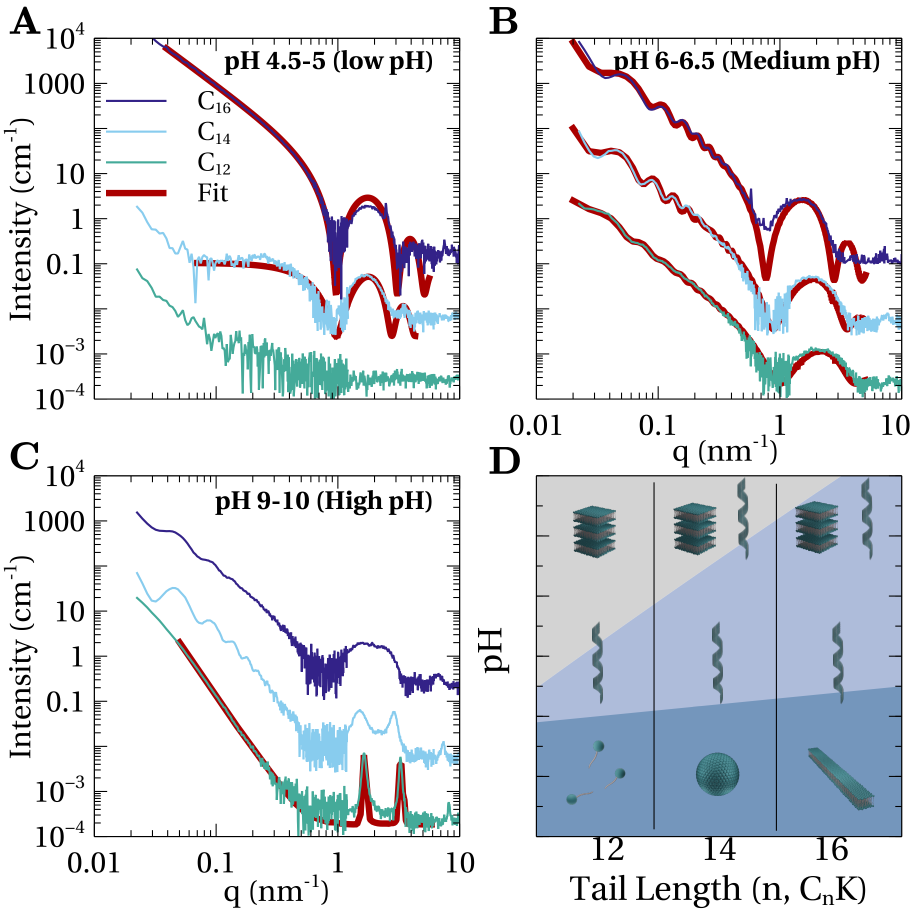

Figure 2.8: SAXS intensity profiles for 4 mM C$_n$K$_1$ solutions at low **A**, medium **B**, and high **C** pH. The data is shown along with fits (red solid lines) for all the cases where the solution consisted of the assemblies of a single type. Fit parameters for helical ribbons are listed in Table 2.1. Based on a multibilayer model [90], the fitting of high pH SAXS data for C$_{12}$K$_1$ (**C**) yielded $N = 140$ for number of lamella. **D.** SAXS-derived structural phase diagram for C$_n$K$_1$ assemblies as a function of molecular tail length (n = 12, 14, 16) and pH.

The effect of adding salt on the planar membrane shape is distinct from the above-described pH-induced changes. Experimentally, pH is increased by adding small quantities of NaOH. The number of free OH$^-$ ions that can screen the membrane charge is minute and varies from 0.01

μM to 1 mM in the pH = 6−11 range. By contrast, when a few mM of salt (e.g., NaCl) is added at low pH, the range of the electrostatic interactions becomes negligible when compared to the membrane dimensions. As a result, the membrane shape becomes insensitive to the short-ranged electrostatic inter- actions (Figure 2.5E). The minimization of interfacial energy then results in planar membranes with $\chi = 1$, even when the membranes are highly charged. These highly charged, $\chi = 1$ membranes cannot form helices as described above. Instead, they roll into scrolls, with inter-bilayer separation much greater than the electrostatic screening length λ_D [73]. The above arguments suggest that the electrostatics-driven chiral shape selection between helices and cochleates should be general to crystalline charged chiral membranes. This point of view is supported by a couple of previous experimental studies. For example, crystalline membranes of a charged, chromophore amphiphile, twisted into helices and rolled into cochleates at low (1 mM) and high (50 mM) NaCl concentration, respectively [49]. Similarly, zwitterionic phospholipid membranes forming helices [3, 4, 19] and charged phospholipid membranes rolling into cochleates in solutions containing multivalent ions [11, 12, 13] are qualitatively consistent with the idea that helices are formed when electrostatic interactions are weak, but long ranged. By contrast, cochleates are formed when the electrostatic interactions are short ranged. Thus, our theoretical model provides a simple electrostatics-based rationale for these observed transitions.

2.3.5 Discussion on Helix Radius as a Function of pH

The helix radius monotonically increases with increasing pH (Table 2.1). At first glance, this appears counterintuitive because the strength of the membrane twisting chiral interactions relative to the electrostatic interactions is expected to increase with increasing pH. This should result in a higher curvature (smaller radius). However, note that the radius increase is concomitant with an increase in the membrane width (Table 2.1). Based on this positive correlation between the radius and width, and the above theoretical model, we speculate that while high aspect ratio membranes are expected in a wide pH window, both the membrane lateral dimensions increase with increasing pH. That is, the molecules can assemble into larger aggregates as the strength of intermolecular electrostatic repulsions is diminished. The increased lateral dimensions result in larger radii for helices, as more energy would be required to bend larger amounts of material. More precisely, if the chiral twisting force remains constant, we would expect a larger radius with increasing width, because the energy to form a helix from a flat membrane scales as $E_{\text{hel}} \propto W/R$, analogous to the case for formation of a cylinder from a flat membrane [34, 35]. We also note that a positive correlation between membrane width and radius was also observed for helices in synthetic bile solutions [24].

2.3.6 pH-Dependent Assembly in $C_{12}K_1$ and $C_{14}K_1$ Molecular Systems

To understand how the coupling between attractive van der Waals and repulsive electrostatic interactions affects chiral assembly, we repeated pH titration and in situ SAXS measurements on aqueous dispersions of $C_{12}K_1$ and $C_{14}K_1$.

Figure 2.2C shows the meaured titration curves for 4 mM C_nK_1 (n = 12, 14, and 16) solutions along with fits based on the Hill equation (eq 2.1). The best fit parameters are listed in Table 2.2. These measurements and the analysis show that the pK_a monotonically increases with decreasing n (Figure 2.2C,D). Furthermore, the Hill parameter m (eq 2.1), while similar for $C_{14}K_1$ and $C_{16}K_1$, approaches 1 (HH case) for $C_{12}K_1$ (Table 2.2). That is reducing the number of carbons in the alkyl tails (1) enhances the propensity of the molecules in aggregates to remain ionized and (2) reduces the interdependency of molecular ionization/deionization events. Both these observations suggest that decreasing the strength of the attractive intertail van der Waals interactions, by reducing the tail length, results in aggregates with larger spacing between the charged molecular groups. This is verfied by SAXS (Figure 2.8A). In particular, for low pH ($\ll$pK_a), $C_{12}K_1$ molecules assemble into small undefined structures or monomers because the precise shape and size of these aggregates could not be determined from the very weak SAXS signal for this sample (Figure 2.8A, green profile). By contrast, for $C_{14}K_1$, spherical micelles (Figure 2.8A, cyan profile) of radius $R_{mic} = 2.54$ nm are observed. This radius is close to the expected molecular length of $C_{14}K_1$ ($t_t \sim 1.7$ nm + $t_h \sim 0.75$ nm). Here, 13×0.127 nm $\sim$ 1.7 nm is the expected C_{14} alkyl tail in the stretched

Table 2.2: Best-Fit Parameters Obtained by Fitting the Titration Curves for C_nK_1 with Hill Equation

molecule	nominal [PA] (mM)	fit [PA] (mM)	pK_a	m [2]
$C_{16}K_1$	4.0	3.3	7.66	0.63
$C_{14}K_1$	4.0	3.2	8.01	0.60
$C_{12}K_1$	4.0	4.0	8.69	0.92

trans-configuration [91] and 0.75 nm is the expected headgroup height as derived from SAXS measurements of $C_{16}K_1$ bilayers. Finally, for $C_{16}K_1$, as described earlier, $\sim$3.8 nm thick interdigitated, crystalline bilayers are observed (Figure 2.8A, navy profile). The splayed molecular arrangement in the curved spherical micelle geometry is expected to result in a larger area per headgroup than for the case of tightly packed molecules in the crystalline planar bilayer. Therefore, the SAXS-derived changes in assembly shapes with tail length are consistent with pH titration-based intuition that more “loosely” packed assemblies are formed with decreasing tail length.

In contrast to the tail length-dependent nano/mesoscopic shapes in the pH $\ll$ pK_a regime, helices of crystalline bilayers are observed for all three C_nK_1 (n = 12, 14, 16) molecular systems when the degree of ionization is reduced by increasing the pH. Here, the intensity profiles (Figure 2.8B) show the characteristic low q (<0.5 nm^{-1}) quasi-periodic intensity modulations due to the helical structure, a broad modulation due to the bilayer thickness for 0.8 nm^{-1} < q < 5 nm^{-1} , and diffraction peaks in the q > 10 nm^{-1} regime that arise from the crystalline molecular packing. Presumably, for the n = 12 and 14 molecular systems, the assembly into helices is preceded by the transformation of ill-defined small aggregates or micelles observed at very low pH into planar bilayer ribbons. This aspect requires further investigation as the precise transformation pathway to helices remains unclear due to the coarse pH steps in the current study. The long-term stability of helical membranes will also be investigated in our future work. This is because some previous studies have suggested that helical membranes with $h/P < 1$ are metastable intermediates to closed helices [nanotubes, $h/P = 1$]. However, the kinetics of the transformation from open to closed helices can be very slow (a few weeks to a few months [21, 74]). In our study, all structures

---

[2] The difference between the nominal and the fit molecular concentrations are perhaps due to errors in measuring very small quantities of flaky powder samples.

were analyzed within 2 days of sample preparation, and in all cases, the helical bilayer model (eqs 2.2 and 2.3) fits to the SAXS intensity profiles (Figure 2.8B, red traces, and Table 2.3) revealed open helices. Furthermore, these fits reveal that (1) the bilayer thickness increases at the rate of $\sim$0.2 nm per additional carbon in the alkyl tail and (2) the helix radius increases with decreasing tail length at a fixed pH.

Finally, in the pH $\gg$ pK_a regime, where the degree of ionization, $\alpha < 0.2$, assembly into multilamellar stacks is observed for all three cases (Figure 2.8C). Specifically, forC$_{12}$K$_1$, SAXS shows two strong diffraction peaks in the 1 nm^{-1} < q < 5 nm^{-1} range (Figure 2.8C, green profile). Based on fitting of the SAXS data (Figure 2.8C, red profile), these peaks arise due to a 1D periodic organization of the membranes in the bilayer-normal direction. For C$_{14}$K$_1$, the assembly consists of a mixture of helices and multilamellar stacks. This is because the SAXS intensity profile (Figure 2.8C, cyan profile) shows the aforementioned characteristics due to helices and the diffraction peaks due to the multilamella. For C$_{16}$K$_1$, the situation is like C$_{14}$K$_1$, with the exception that the multilamella diffraction peaks are very weak (Figure 2.8C, navy profile, and Figure 2.3C). These observations imply that at a fixed pH, the propensity for helices to transform into multilamellar stacks decreases with increasing alkyl tail length. Based on the positions q_1 of the principal multilamella diffraction peak, the interbilayer spacing $d_m = 2\pi/q_1$ are 4.49, 4.13, and 3.83 nm for C$_{16}$K$_1$, C$_{14}$K$_1$, and C$_{12}$K$_1$, respectively. These spacings are only 20−30% larger than the bilayer thicknesses of 3.82, 3.37, and 3.0 nm for C$_{16}$K$_1$, C$_{14}$K$_1$, and C$_{12}$K$_1$, respectively. This observation is consistent with the expectation that, in the very high pH regime, the interbilayer electrostatic repulsions are very weak, and short-ranged attractive interactions such as van der Waals interactions can drive the assembly into closely packed lamellar stacks.

In the medium to high pH regime two trends are puzzling. (1) At a fixed pH, the helix radius and width increase with decreasing tail length (Table 2.3). This is surprising because our above-described theoretical model and arguments for planar membranes suggested that the membrane width and thus the helix radius should increase with decreasing degree of ionization. Because the degree of ionization follows the sequence $\alpha_{\mathrm{C}_{12}}$ > $\alpha_{\mathrm{C}_{14}}$ > $\alpha_{\mathrm{C}_{16}}$, in the pH regime where helices are observed (Figure 2.2D), it was expected that the radii would follow: $R_{\mathrm{C}_{12}}$ < $R_{\mathrm{C}_{14}}$ < $R_{\mathrm{C}_{16}}$. (2)

It is surprising that the tendency for forming multilamella increases with decreasing tail length, in the pH 9−10 regime (Figure 2.8C). Based on our theoretical model, bilayer stacks are expected above a critical pH, where the vast majority of molecules are deionized, and the planar membrane transforms to the lowest perimeter (aspect ratio $\chi = 1$) configuration. In the pH 9−10 regime, the degree of ionization is expected again to follow the trend $\alpha_{\mathrm{C}_{12}} > \alpha_{\mathrm{C}_{14}} > \alpha_{\mathrm{C}_{16}}$ (Figure 2.2D). Therefore, the fraction of stacks to helices was expected to be highest for $\mathrm{C}_{16}\mathrm{K}_1$ and lowest for $\mathrm{C}_{12}\mathrm{K}_1$. These discrepancies imply that our theoretical model is very simplistic. It qualitatively explains the assembly shape selection and the nanoscale structure evolution with pH for a given molecular system but fails in explaining the quantitative trends when assembly behavior across distinct molecular systems is compared. Therefore, more detailed models or simulations are required that perhaps account for the molecular packing or the electrostatic and the steric coupling between the two leaflets of the interdigitated membrane. For example, such models may predict that bending rigidity follows the sequence $\kappa_{\mathrm{C}_{12}} > \kappa_{\mathrm{C}_{14}} > \kappa_{\mathrm{C}_{16}}$. This could account for the observed trend in helix radius with tail length because $E_{\mathrm{hel}} \propto \kappa$. Such models and simulations are beyond the scope of the current work and will form part of our future investigations.

We note here that while helices are observed for all the three $\mathrm{C}_n\mathrm{K}_1$ studied, the formation of these chiral mesoshapes is extremely sensitive to molecular design. If the headgroup charge is increased by adding even one additional ionizable group (e.g., $\mathrm{C}_{16}\mathrm{K}_2$ [14, 86]), then only spherical and cylindrical micelles are observed over an extended pH range and some planar membranes are observed only in the regime where the degree of ionization is very low. For polyionic amphiphiles, helical membranes have been observed (1) for molecules that are double-tailed [74] and (2) for single-tailed peptide amphiphiles consisting of multiple unionizable amino acids, which facilitate interheadgroup hydrogen bonding networks (e.g., β-sheet) [21, 71]. Based on this observation, we speculate that single-tailed molecules with one ionizable chiral headgroup, such as $\mathrm{C}_n\mathrm{K}_1$, represent the simplest molecular design for analyzing chiral structures.

The pH-dependent assembly in the $\mathrm{C}_n\mathrm{K}_1$ molecular series is summarized in Figure 2.8D. Most notable is the commonality that the molecules assemble into helices in the intermediate pH regime and bilayer stacks in the high pH regime when a majority of the molecules are deionized. These

Table 2.3: C$_n$K$_1$ Helix Parameters Derived from Fits in Figure 2.8B

molecule	pH	R (nm)	ψ (deg)	W (nm)	h/P	% polydispersity[3]
C$_{16}$K$_1$	6	62.6	29.3	115.6	0.59	5.5
C$_{16}$K$_1$	7	69.6	31.9	128.1	0.56	8.7
C$_{14}$K$_1$	6.5	76.1	29.0	180.45	0.68	7.4
C$_{12}$K$_1$	6.5	94.5	32.6	227.80	0.60	11.7

observations further validate the hypothesis that for crystalline membranes, helix is the equilibrium chiral morphology in the regime where electrostatic interactions are weak, but long-ranged.

2.3.7 Molecular Packing via MD Simulations and WAXS

Thus, far we have focused on the meso- and nano-scale aspects of the membrane shape. Here, we combine molecular dynamics (MD) simulations (see 2.2) and wide-angle X-ray scattering (WAXS) to investigate -scale molecular packing in C$_n$K$_1$ planar membranes. In particular, we focus on molecular tilt. Theoretical models for chiral assemblies require molecules to be tilted with respect to the membrane-normal [17, 32, 36]. However, due to orientational averaging in solution X-ray scattering and due to a limited number of diffraction peaks observed from membranes, precise determination of tilt angles from WAXS data alone is challenging. As such, combining MD simulations and WAXS analysis can prove useful in accessing information regarding molecular packing in assemblies.

We perform MD simulations on C$_{16}$K$_1$ and C$_{12}$K$_1$ planar bilayers as a function of degree of ionization α to understand how electrostatic and van der Waals interactions affect molecular packing. Thereafter, the molecular tilt obtained from MD simulations is used as a starting point for analysis of WAXS data for C$_{16}$K$_1$ bilayers.

Figure 2.9 summarizes the MD simulation results. These simulations validate the X-ray scattering-derived conclusion that the molecules assemble into crystalline, interdigitated bilayers. Further-

---

[3] Some bilayer parameters were fixed: $t_h = 0.75$ nm and $\rho_h = 430$ e/ nm^3 . The best fit values for the bilayer thickness and the electron density for the hydrophobic tail region were [t_b (nm), ρ_t (e/nm^3)] = [3.8, 307], [3.37, 300], and [3.0, 290] for $n =$ 16, 14, and 12, respectively.

more, consistent with theories for chiral membranes **??**, the molecules are found to be tilted with respect to the bilayer-normal. These aspects are illustrated through a simulation snapshot for a $\mathrm{C}_{16}\mathrm{K}_1$ bilayer (Figure 2.9D). Figure 2.9A−C show the MD-derived variation in important membrane parameters (defined in Figure 2.9E): area per lipid in a leaflet (APL), tilt magnitude (θ), and the bilayer thickness (t_b) as a function of degree of ionization α, which was controlled via pH in the experiments. Figure 2.9C shows that APL increases with increasing degree of ionization. This is due to increased inter-headgroup repulsions. Concomitantly, the alkyl tails tilt more [θ increases (Figure 2.9A)] such that the increase in the intertail distance is compensated. In particular, to a first approximation, the area/lipid tail/leaflet in the plane normal to the molecular tilt vector (or the molecular long axis) $S_0 = \text{APL} \times \cos\theta$ is independent of α and has the same value for both $\mathrm{C}_{12}\mathrm{K}_1$ and $\mathrm{C}_{16}\mathrm{K}_1$ (Figure 2.9F). As would be expected, an increase in θ, results in a thinner membrane. That is, t_b decreases with increasing α (Figure 2.9B).

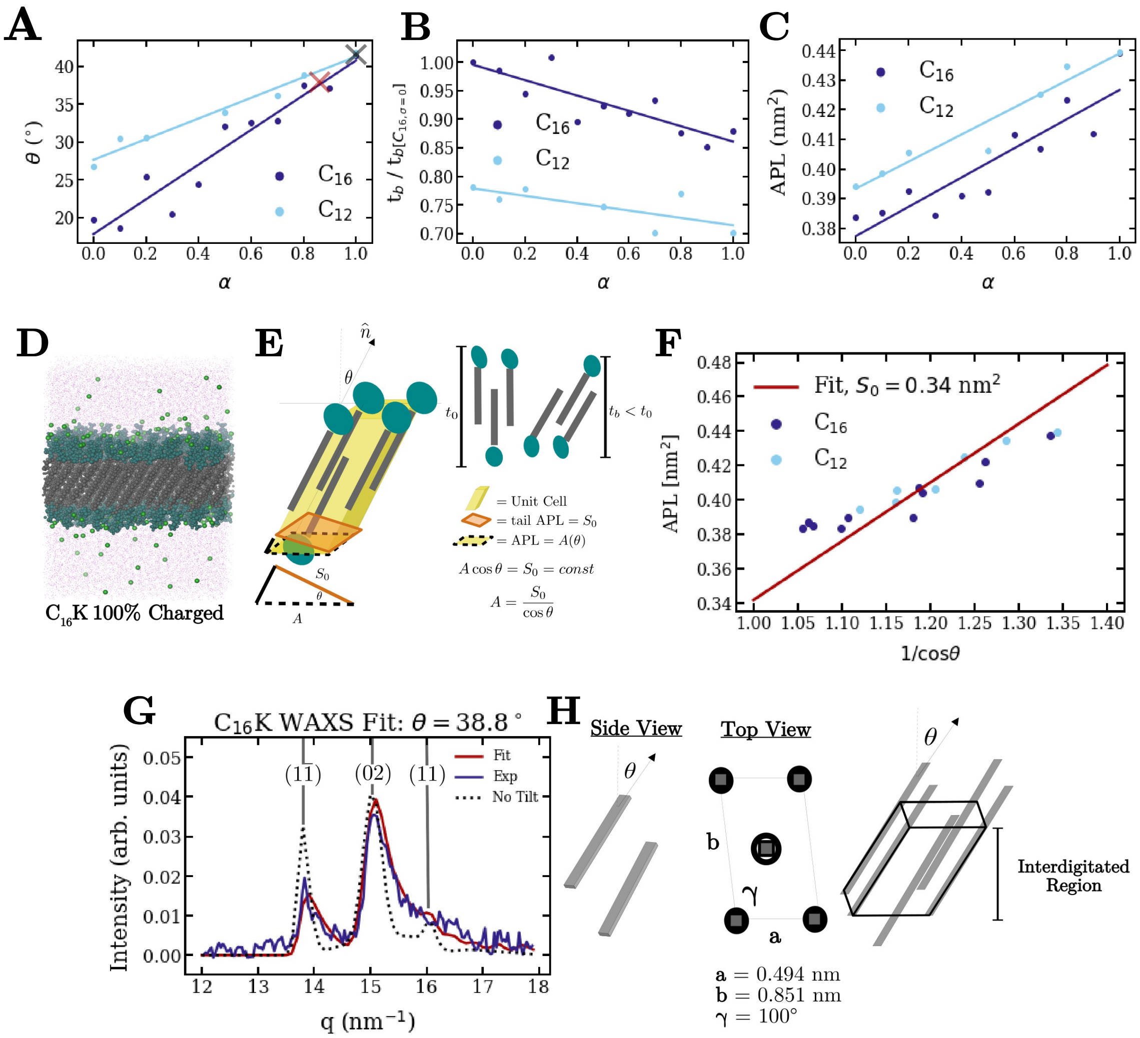

Figure 2.9: A. Molecular tilt angle with respect to the bilayer normal, **B.** bilayer thickness, and **C.** area/lipid/leaflet, for $C_{16}K_1$ and $C_{12}K_1$ bilayers at varying degrees of ionization. Bilayer thickness in **B** is normalized to the thickness of $C_{16}K_1$ bilayers at $\alpha = 0$. The navy and cyan lines in **A**-**C** are guides to the eye for MD data for $C_{16}K_1$ and $C_{12}K_1$ bilayers, respectively. **D.** Simulation snapshot of a $C_{16}K_1$ bilayer after 250 ns. Purple dots: water molecules; neon green: chloride counterions; green: headgroups; gray: tails. **E.** Definitions for the bilayer parameters APL, S_0 , θ, and t_b. **F.** The APL vs $1/\cos\theta$ data for $C_{16}K_1$ and $C_{12}K_1$ bilayers collapses on a straight line through origin. This demonstrates the constancy of the area per lipid tail in the tilt-normal plane. **G.** WAXS data for $C_{16}K_1$ bilayers at pH = 4.5 (blue) and corresponding fit (red) based on the tail packing model of the interdigitated region and oblique lattice shown in **H**. Miller indices for the diffraction peaks are labeled in gray.

We note that in C$_n$K$_1$ bilayers, APL is expected to be much larger than the cross-sectional area of an alkyl tail [$\sim S0/2$, (Figure 2.9E)]. This is due to a combination of the large headgroup size and the electrostatic repulsion between these charged groups. Therefore, the packing of the alkyl tails in a single leaflet is expected to be sparse. A dense arrangement of alkyl tails can only be achieved through interdigitation. Based on this observation and the above-derived coupling between APL and θ, we speculate that maximization of tail−tail van der Waals interactions is achieved through interdigitation and molecular tilt, which minimize the intertail distances by compensating for the difference between the APL and the lipid tail cross-sectional area. These MD-derived results are qualitatively consistent with experimental studies on lipid membranes: First, the MD-derived electrostatic driven increase in APL and the constancy of the tail area in the tilt-normal plane has been previously observed in noninterdigitated lipid membranes [94]. Second, the range of MD-derived tilt angles θ (~ 18−$42°$, Figure 2.9A) is consistent with the observed tilt angles in monolayers [95, 96] and bilayers [94, 97] of double-tailed lipids for which (1) headgroup cross-sectional area is greater than that for two alkyl tails and (2) APL $\sim$ 0.40 nm^2 , similar to the case for C$_n$K$_1$ (Figure 2.9C).

The qualitative trends in APL, θ and t_b are common to both the C$_{12}$K$_1$ and C$_{16}$K$_1$ bilayers. However, two tail length-dependent effects are observed. (1) For a given α, the APL (and consequently θ) is larger for C$_{12}$K$_1$ membranes (Figures 2.9A,C). The equilibrium molecular distances in the membrane plane and thus the APL are determined by the competition between the attractive and repulsive intermolecular interactions. We speculate that the APL is larger for C$_{12}$K$_1$ because the intertail van der Waals interactions are expected to be weaker than for the case of the longer tailed C$_{16}$K$_1$. (2) For a given α, the bilayer thickness t_b is smaller by ~ 20−25% for C$_{12}$K$_1$ (Figure 2.9B). This is due to the combined effects of shorter tail length and the larger molecular tilts θ for C$_{12}$K$_1$. We note that the MD results are consistent with the SAXS-derived thickness difference of $\sim$22% between the C$_{16}$K$_1$ and C$_{12}$K$_1$ membranes in the pH > 9 regime.

The above discussion shows that MD results can be rationalized by arguments based on intermolecular electrostatic and van der Waals interactions, and steric constraints on molecular packing. To test the MD results against experimental data, we analyzed the WAXS data from C$_{16}$K$_1$ bilayers formed at pH $\sim$ 4.5 [($\alpha \sim 1$), Figure 2.9G,H]. Experimentally, this is the only C$_n$K$_1$ assembly case where unstacked or unbent bilayers were observed. Figure 2.9G shows the WAXS data for $13 < q < 17$ nm^{-1} , where two of the strongest diffraction peaks at $q \sim 13.8$ and 15.0 nm^{-1} and a weak peak at $q \sim 16.5$ nm^{-1} are observed. These peaks are due to crystalline packing of molecular tails. In our previous work, [73] we had analyzed a similar diffraction data from a previous sample batch using a parallelepiped model for untilted tails, which were arranged on an oblique 2D lattice with $a = 0.49$ nm, $b = 0.85$ nm, and $\gamma = 100°$. Here, we show that including the tail tilt improves the fit to the data. As a starting point for WAXS analysis, we use the previously obtained lattice parameters, and the MD-simulation-derived tilt angle [$\theta = 41.5°$, Figure 2.9A, black cross]. The tails were allowed to rotate about all 3 Cartesian axes. The WAXS intensity calculations powder averaged the intensities from the modeled 2D interdigitated arrangement of the parallelepiped shaped tails, following the procedure by Harutyunyan et.al [98]. For further details, see B.3. The best-fit to the data is plotted in Figure 2.9G, and the corresponding unit cell is shown in Figure 6H. The two key findings from this analysis are as follows: (1) The oblique 2D unit cell (u.c.) can be described by lattice parameters $a = 0.494$ nm, $b = 0.851$ nm, and $\gamma = 100°$, very similar to those obtained via previous analysis. This corresponds to an APL $= ab \sin\gamma = 0.414$ nm^2/lipid/leaflet, which is very close to the MD-predicted APL for $\alpha = 1$ (Figure 2.9C). However, we note that the above-described oblique lattice was not reproduced in our atomistic MD simulations, which showed a structure close to a hexagonal packing of molecular tails by analyzing the radial distribution function of the bilayer assemblies (Figure 2.10). This may be due to the limited length scale ($\sim$10.0 nm) or time scale (0.3 μs) of the simulations or limitations of the CHARMM36 force field [99]. The limitation in achieving nonhexagonal molecular packing in MD simulations has been noted previously [100] and requires further investigation. (2) The basis consists of two tails: one pointing downward at the u.c. origin and one pointing upward at the u.c. center. Both the tails are tilted by $\theta \sim 38°$ with respect to the bilayer-normal. This θ matches the MD-predicted value at $\alpha = 0.9$ (Figure 2.9A, red cross), but is slightly lower than the MD-prediction of $\theta \sim 41.5°$ at $\alpha = 1$. Nevertheless, Figure 2.9G shows that the tilted tail model is significantly better than the untilted tail model in describing the WAXS data. Taken together, WAXS and MD simulations show that the bilayers are interdigitated and consist of molecules that are tilted with respect to the bilayer-normal.

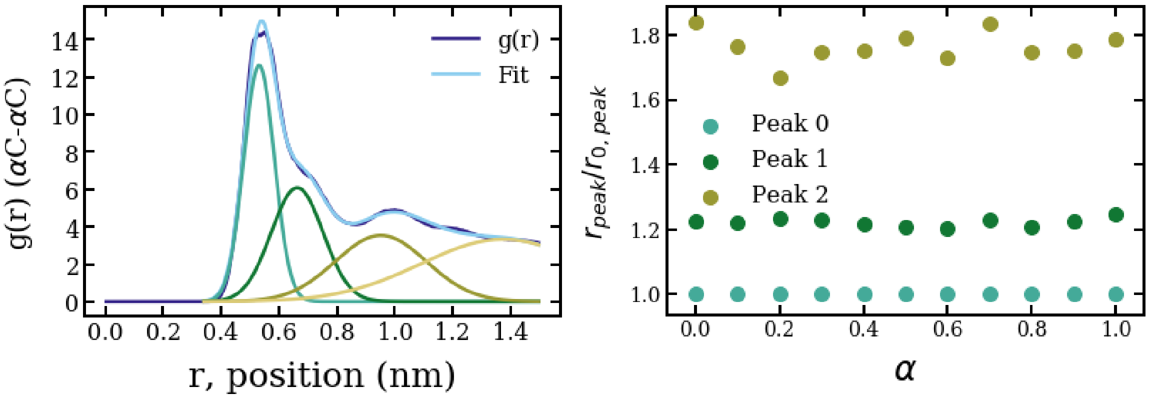

Figure 2.10: **A.** Radial distribution functions were calculated for the α-Carbon locations (the chiral center of the lysine headgroup) from MD simulations for $C_{16}K_1$ bilayers. The distributions were fitted with Gaussian peaks for systematically calculating peak positions. There are 3 notable peaks within the distribution profile: a primary peak at $r_0 \sim 0.53$nm, a shoulder peak at $r_1 \sim 0.66$ nm, and another broad peak at $r_2 \sim 1$ nm. The fourth gaussian peak used within the fit is not meaningful and only included to account for a background due to the semi-fluid nature of the membranes. For a perfect hexagonal lattice, the first three relative peak positions should have the following ratio relationship: $1:3:2$. The positions of the broad peaks at r_0 and r_2 match the $1:3$ ratio. However, the existence of the shoulder peak at $r_1/r_0 \sim 1.2$ is not accounted for by a pure hexagonal packing and suggests that the tilted interdigitated chains pack primarily in a distorted hexagonal lattice. **B.** These calculations were repeated for simulations at different α values and similar distorted hexagonal packing was found for bilayers at varied degrees of ionization.

2.4 Summary and Future Work

We designed a homologous series of ionizable chiral amphiphiles C_nK_1 (n = 12, 14, 16) and studied the assembly behavior of these molecules as a function of solution pH, which controlled the degree of ionization. The assembly structures were experimentally analyzed over to μm length scales using solution X-ray scattering and transmission electron and atomic force microscopies and were theoretically rationalized through a rudimentary model of charged membranes and MD simulations. Our multitechnique study has four key results: (1) At the and sub-nm scale, MD simulations in conjunction with WAXS experiments show that the C_nK_1 bilayers exhibit crystalline packing of tilted lipid tails. The tails from the two bilayer leaflets strongly interdigitate. This packing arrangement could be explained by an interplay between van der Waals and electrostatic interactions. (2) At the mesoscale, systematic SAXS analysis showed that the crystalline, high aspect ratio membranes curve into helical bilayers in the regime where electrostatic interactions are weak, but long-ranged. In particular, helical assemblies were observed for all three $\mathrm{C}_n\mathrm{K}_1$ molecular systems at elevated pH, where the degree of ionization was low. (3) Both MD simulations and SAXS experiments suggest that the nm-scale structure of the bilayer helices can be continuously tuned via electrostatic interactions. Particularly, the molecular tilt decreases, and helix radius increases with decreasing degree of ionization. (4) Electrostatic interactions can direct chiral shape selection: helicoidal scrolls (cochleates) are observed in saline solutions when the intermolecular electrostatic interactions are screened and short-ranged and helices are observed under conditions when the degree of ionization is low, but the electrostatic interactions are long-ranged. This finding was rationalized with an elementary theoretical model based on competition between membrane electrostatic and interfacial energies.

These results highlight the versatility of our designed simple molecular systems in exploring the phase space of chiral shapes, and pave way for further studies. For example, analyzing the assemblies at higher temperatures or for molecules with shorter tails may reveal other chiral shapes such as twisted ribbons with saddle-like curvature because previous theoretical [9] and experimental [71] investigations suggest helix to twisted ribbon transitions in the regime where the order in the molecular packing is reduced. The experiments and simulations can be extended to analyze how membrane bending rigidities and intermolecular chiral coupling affect the nanomesoscale structure (helix and cochleate radius, helix pitch, etc.). Overall, our studies experimentally detect and explain how achiral interactions can control shape selection and nanoscale structure in chiral assemblies. These results should be useful in attaining and optimizing distinct structures based on chiral building blocks for varied applications.

3 Chapter 3

“Nobody ever figures out what life is all about, and it doesn’t matter. Explore the world. Nearly everything is really interesting if you go into it deeply enough.”

-Richard P. Feynman

In this chapter we further explore the phase space of C$_n$K$_1$ molecular assemblies and suggest preliminary results that pave the way for future studies. We investigate more structural details of C$_n$K$_1$ assemblies through studies of varied ratios of C$_n$K$_1$ chiral enantiomers in assembly, simulations of C$_n$K$_1$ bilayer elastic properties, and a finding of an additional observed chiral assembly of twisted ribbons, highlighting C$_n$K$_1$ versatility as a system for exploring charged, chiral assemblies.

3.1 Introduction

The hierarchical self-assembly of chiral building blocks is manifested in diverse and fascinating shapes at nano- to meso-scale [1]. The most common shapes for chiral amphiphilic molecules are helical membranes, helical scrolls (cochleates) and twisted membranes, which have been observed in natural and synthetic systems [12, 24, 61, 73, 75, 101]. The design and properties of the building blocks are the core for hierarchical self-assembly into chiral nanostructures. Generally, the introduced chiral element of the molecules or units dictates the final supramolecular chirality, while the balance between different interactions directs the hierarchical self-assembly.

Soft chiral assemblies have potential nanotechnological applications that depend sensitively on the overall shape of the assembly. For example, semiconductors formed from chiral CdTe nanoparticles, carrying L- or D-cysteine amino acids as surface ligands showed that varying the geometry of helices via varying the assembly conditions enabled tunability of their chiroptical properties [102]. In addition, a class of materials containing charged, chiral assembling components known as peptide (i.e. multiple amino acids) amphiphiles (PAs) are of great interest due to there biocompatiability and wide-ranging functionalization [75]. For example, one such application of PA assemblies is for bioartificial nerve conduits where the PAs can function as biomimetic materials to help people suffering from peripheral nerve injury [103]. Design parameters would encompass aspects like adequate porosity of the PA assemblies to facilitate the delivery of nutrients to the regenerating neural cells. Characterizing the precise nano-scale details and understanding interconversion mechanisms between different morphologies is clearly crucial to such technological applications.

Despite the prevalence and potential use of charged chiral nanostructures, an understanding of the interconversion mechanisms between different morphologies of chiral building block assemblies is lacking. This knowledge gap is primarily due to the absence of a molecular system (i.e. building block) that enables a systematic exploration of the phase space of chiral shapes, and because the important electrostatic interactions are neglected in theoretical work. In this study, we were able to generate and thoroughly charaterize all the common chiral structures in perhaps the simplest chiral molecular series C_nK_1, where one amino acid [lysine (K)] is coupled to alkyl tails of n (= 10-18) carbons. Scroll-like assemblies were observed when the molecular degree of ionization was high, and the electrostatic interactions were short-ranged. By contrast, helical and twisted membranes are observed for long (n = 12-18) and short (n = 10) molecular tails, respectively, when the molecular degree of ionization was low and the electrostatic interactions were long-ranged. This was accomplished by tuning the solution ionic conditions. These results were derived by combining X-ray scattering and electron/atomic force microscopy and further investigated with molecular dynamics simulations. Overall, with the use of a simple system C_nK_1, our study reveals that electrostatic interactions can be used to guide chiral shape selection and nanoscale structure in molecular self-assemblies.

3.2 Method Specifications

3.2.1 Peptide Synthesis

Peptides were synthesized using a CEM Liberty Blue microwave- assisted peptide synthesizer. Standard fluoren-9-ylmethoxycarbonyl (Fmoc) solid-phase peptide synthesis was used with rink amide MBHA resin (100-200 mesh). Each coupling was performed using 4 equivalents of Fmoc-protected amino acid or fatty acid, 4 equivalents of N,N'- diisopropylcarbodiimide (DIC), and 8 equivalents of ethyl(hydroxyimino)cyanoacetate (Oxyma pure) in DMF. Removal of the Fmoc groups was achieved with 20% 4-methylpiperidine in DMF and 0.1 M 1-hydroxybenzotriazole (HOBt). Peptides were cleaved from the resin using a mixture of 95% trifluoroacetic acid (TFA), 2.5% water, and 2.5% triisopropylsilane for 3 h. Crude peptide was precipitated from this solution using cold diethyl ether. Purification was carried out on a Waters Prep 150 HPLC using a water/acetonitrile with 0.1% TFA solvent system and a Phenomenex Kinetex 30×150 mm C18 column. Eluting fractions were analyzed by Electrospray Ionization Mass Spectrometry (ESI-MS) using an Agilent 6520 Q-TOF LCMS before lyophilization and purity analysis by the same Agilent LCMS (water/acetonitrile with 0.1% formic acid solvent system and Phenomenex Proteo 100 × 1 mm column).

3.2.2 X-ray Scattering

SAXS/WAXS intensities (0.02 nm^{-1} < q < 30 nm^{-1}) were collected simultaneously using three Rayonix CCD detectors at the 5 ID-D undulator beamline of the Advanced Photon Source (APS) at Argonne National Laboratory. The beam size was 0.25 × 0.25 mm^2 , and the incident beam intensity was $\sim 3 \times 10^{11}$ photons/s. The sample solutions were injected through a capillary tube flow-cell (1.5 mm, quartz) at 2-5 mm/sec to reduce radiation damage. The capillary was embedded in a vacuum cell to avoid air scattering. A fast shutter was used to limit sample exposure to X-rays only during the data collection time (5-10 s for each measurement). For improving statistics, 5-10 measurements were made per sample. For background subtraction and for calibrating the intensities to an absolute scale, SAXS/WAXS patterns were also collected from the empty capillary and from the capillary containing pure water before measurements on every sample. Additional SAXS/WAXS measurements were performed at 12 ID-C,D. At this APS beamline, data was collected using a Pilatus single photon counting area detector placed at a sample to detector distance (SDD) of 2.27 m. 15 or 17 keV X-ray were used with X-ray wavelength λ = 0.0827 or 0.0729 nm. The beamsize at the sample position was $\sim$ 0.4mm $\times$ 0.2mm and the flux was 2 $\times$ 10^{12} photons/s. An exposure time of $\sim$1 s was used.

The 2D SAXS/WAXS patterns were converted into 1D intensity profiles by azimuthal integration while taking into account the polarization, solid-angle and transmission corrections. The data were also normalized for the scan time. For absolute intensity calibration, the normalized and corrected scattered intensity profiles from pure water (difference of the scattering from capillary filled with water and the empty capillary) were fitted to straight lines. The intercept of these lines was set to 0.0165 cm^{-1} , the expected scattered intensity from water at q = 0 on an absolute scale at T = 25°C. The data from the corresponding samples were thereafter scaled accordingly.

3.2.3 Cryo-TEM

Microscopy was performed with a Hitachi HT7700 tungsten emission TEM at 100 kV and data was collected on a Gatan Orius 2 k $\times$ 4.67 k digital camera. For sample preparation, 200-mesh Cu grids with a lacey carbon membrane were glow-discharged for 30 seconds in a Pelco easiGlow glow-discharger at 15 mA with a chamber pressure of 0.24 mBar. 4μL of 4 mM amphiphile solutions were then pipetted onto the grid and plunge-frozen into liquid ethane with an FEI Vitrobot Mark III cryo plunge freezing robot with 5 seconds of blotting and a blot offset of 0.5 mm. Grids were stored in liquid nitrogen until loaded into a Gatan 626.6 cryo transfer holder cooled down to -172°C.

3.2.4 Titration

5-6 mL solutions of 4 mM C_nK_1 were titrated with a 100 mM NaOH solution. The amphiphile and the NaOH solutions were freshly prepared in ultrapure water (resistivity = 18.2 MΩ·cm). The pH was measured using an Oakton pH 6 Acorn Series meter equipped with a Mettler Toledo micro electrode, which was calibrated at pH 4, 7 and 10 using buffers, prior to titration measurements.

3.2.5 MD Simulations

Classical coarse grained explicit solvent molecular dynamics (MD) simulations were performed to study the nanoscale order of $C_{12}K_1$ and $C_{16}K_1$ flat bilayers. All simulations are performed using GROMACS 2016.3 [77]. The coarse grained Martini 2.2P force field was employed to model C_nK_1 bilayers, which includes Coulomb electrostatic and Leonnard-Jones interactions as well as polarizable water molecules [104, 105, 106, 107, 108, 109, 110, 111, 112]. Martini uses an approximate 4:1 atomistic (heavy atoms) to CG bead mapping. The lysine amino acid head group was parameterized with 3 Martini beads [113] and the carbon tail with 2, 3, 4, and 5 beads corresponding to atomistic tail lengths of n = 8, 12, 16, 20 carbons. Bond lengths and angles of C_nK_1 molecules were mapped to to match atomistic trajectories within the CHARMM36 force field [61, 82].

For simulations, 10 lipid molecules (1x1 unit) were preassebled into a small bilayer to be used as a building block for larger bilayer (10x10 units) simulations. Bilayers were preassembled using the packmol [114] software and solvated with polarizable water (PW) molecules and Cl^- counterions for electroneutrality. PW was used to correct modeling of the partitioning of polar and charged compounds into a low dielectric medium, e.g. a lipid bilayer, which is known to be a challenge in coarse grained MD simulations [107]. All bilayer normals were oriented in the z direction. MD simulations were carried out using a rectangular box ($\sim$ 18 $\times$ 19 $\times$ 20 nm^3) with periodic boundary conditions in x, y, z directions. The bilayer/explicit solvent system is equilibrated using the V-rescale modified Berendsen thermostat for temperature (T=300 K). Pressure equilibration used Parrinello-Rahman semi-isotropic coupling with a reference value of 1 bar, compressibility of 3×10^{-4} bar^{-1} , and characteristic time of 12 ps. In addition, a relative dielectric constant $\epsilon_r = 2.5$ is used as customary for polarizable water Martini 2.2 simulations [107]. A global dielectric constant $\epsilon_r = 15$ is used in the standard MARTINI without polarizable water. In the polarizable model, the global dielectric constant is reduced to $\epsilon_r = 2.5$ to ensure a realistic dielectric behavior in the hydrophobic regions. Other force field parameters are the same as in standard MARTINI. After equilibration,

C_nK_1 bilayer production runs were carried out in the NPT (canonical) ensemble for 250 ns with a time step of 10 fs and semi-isotropic pressure coupling with the same Parrinello-Rahman coupling parameters. Periodic boundary conditions were employed in all dimensions during production simulations. Electrostatic interactions are all calculated using the particle mesh Ewald (PME) method with a 0.16 grid spacing. Real space cut-off values for electrostatic and Van der Waal forces were 1.1 nm.

3.3 Results and Discussion

3.3.1 C_nK_1 Cochleate Generality

3.3.1.1 C_nK_1 Assemblies with Added NaCl, n=12,14

In 1.3.1 and 1.3.2, we described how $C_{16}K_1$ molecules in aqueous solution will form flat bilayer ribbons and sheets that gradually transform into scroll-like (cochleate) assemblies with increasing ionic strength [73]. Specifically, 4mM solution of $C_{16}K_1$ showed 10:1 aspect ratio bilayer ribbons at 0mM NaCl. The aspect ratio of the planar assemblies decreased to $\sim$1:1 at a NaCl concentration of $\sim$3mM and then proceeded to roll into cochleates at 5mM NaCl (Figure 1.2**a-d**). In-situ X-ray scattering measurements robustly characterized the structural features of this transformation pathway as a function of NaCl concentration, which showed the spacing between the lamella in the scroll assemblies (D) decreased monotonically with an increase in ionic strength (c)(Figure 1.3).

We repeated in-situ scattering measurements for $C_{12}K_1$ and $C_{14}K_1$ to test the generality of the cochleate transformation. 4mM $C_{12}K_1$ solution showed minimal assembly behavior for [NaCl]<50 mM signified by a weak scattering signal (Figure 3.1A). At an [NaCl] concentration of 50mM, the scattering pattern is fit well by micellar (core-shell) assemblies. The assembly process can be described by basic electrostatic interactions. Driven by the hydrophobic alkyl tails, the assembly of the shorter tailed $C_{12}K_1$ is unable to overcome the strong electrostatic repulsion of the highly charged headgroups preventing assembly into closely packed structures like micelles. Upon an increase of NaCl, the inter-headgroup electrostatic interactions become highly screened and assembly is possible. Micelles, which have the lowest critical packing parameter (CPP), allow for the largest area-per-lipid (APL), and therefore lowest electrostatic repulsive forces, when compared to other assemblies such as cylindrical micelles or flat bilayers.

For $C_{14}K_1$, the increased tail length and hydrophobicity permits formation of micelle assemblies in low ionic strenth-, large screening length-environments (Figure 3.1B, red). Again, formation of micelles is expected as this type of packing allows for the highly charged headgroups to be spread out as much as sterically possible. Upon an increase of NaCl, we observe oscillatory and peak features in the scattering pattern that is akin to cochleate scattering patterns described in Figure 1.3 for $C_{16}K_1$ (Figure 3.1B, blue). The peak corresponding to the cochleate lamella for $C_{14}K_1$ cochleates at [NaCl]=10mM (highlighted purple) show a D-spacing of $\frac{2\pi}{0.32\ \text{nm}^{-1}} \simeq 19.6$ nm between sheets, similar to the spacing observed for $C_{16}K_1$ cochleate (Figure 3.1C, blue and green). In addition, at low $q < 0.08\text{nm}^{-1}$, we see a large primary oscillation peak, which is related the overall size of the cochleate (Figure 3.1C, blue and green). Such a peak is not visible for $C_{14}K_1$ at 10mM NaCl, but there is a trending increase at the low q limit ($q \simeq 0.025\ \text{nm}^{-1}$). For this reasons, we hypothesize that $C_{14}K_1$ form larger cochleate structures, but the large features are cut-off by the limit of our scattering data.

Upon a further increase of NaCl to 50mM, $C_{14}K_1$ cochleate scattering pattern features are asbsent and pronounced stacking peaks appear at $1 < q < 10\text{nm}^{-1}$, in stark contrast to the continued manifestation of $C_{16}K_1$ cochleate assemblies at higher ionic strengths (Figure 3.1B,C, green). The intensity peaks at $q \simeq 1.8$, 3.6, and 7.2 correspond to lamellar stacking behavior of bilayer sheets with a spacing of ~ 3.5 nm. Such as spacing is consistent with the average thickness of $C_{14}K_1$ bilayers $t = 3.6$ nm (2.8). The asbsense of cochleate at higher ionic strength is puzzling as one would expect similar behavior to $C_{16}K_1$ as the assembly-driving chiral and charged headgroups are the same for $C_{14}K_1$. One possible explanation is that the large radii $C_{14}K_1$ cochleate collapse onto each other before they are able to form closed scrolls. With multiple bilayers stacked together, the chiral twisting forces are insufficient to roll the assemblies into cochleate. Due to the limitations of numerical simulating intractable form factors like that of the cochleate (see B.1.2), we are unable to form robust conclusions about all the cochleate structural parameters.

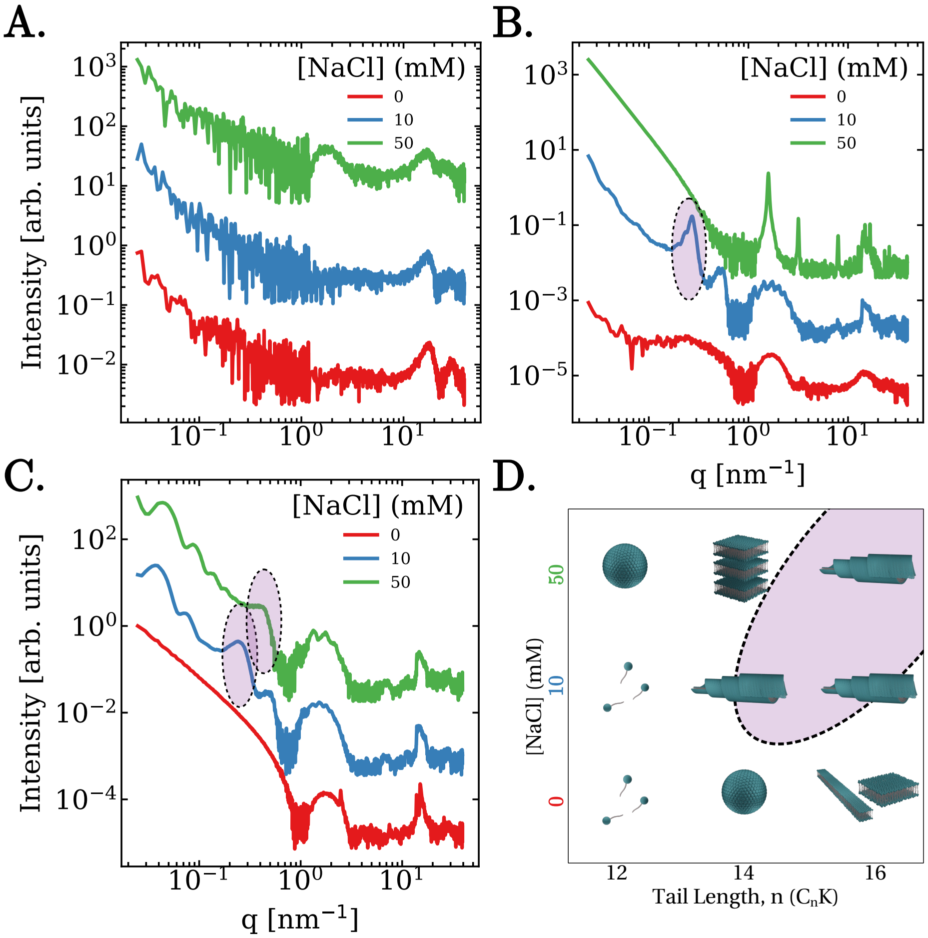

Figure 3.1: SAXS/WAXS measurements of C_nK_1 assemblies for **A.** n=12, **B.** n=14, **C.** and n=16. **D.** Phase diagram outlining the SAXS/WAXS inferred transformation pathways for $C_{12}K_1$,$C_{14}K_1$, and$C_{16}K_1$ assemblies for [NaCl]=0,10, and 50 mM. $C_{12}K_1$ have very low scattering at low NaCl concentrations and begin to form micelles at [NaCl]=50mM, but never form cochleates. Cochleates (purple) are formed by $C_{16}K_1$ assemblies for all [NaCl]$\geq$5mM. Similarly, $C_{14}K_1$ form cochleates at [NaCl]=10mM with sharp diffractions peaks, but oscillations in the low q regime, a signature of cochleate assemblies, are absent at higher salt concentrations (50mM) and the very sharp diffraction peaks at 1<q<3nm^{-1} correspond to lamellar stacking behavior.

3.3.1.2 $C_{16}K_1$ Cochleate: Varying the Chiral Coupling

In preceding sections, we have tuned the electrostatic interactions of the lyinse headgroups in C_nK_1 assemblies to achieve different chiral morphologies. In principle, the strength of the chiral interactions can also be altered by producing binary mixtures with varied ratios of molecules with right- (D) and left-handed (L) lysines. We test this procedure by characterizing $C_{16}K_1$ cochleate assemblies of varied ratios of lysine enantiomers in aqueous solutions of fixed ionic strength.

Figure 3.2A shows the measured SAXS/WAXS profiles of 4mM $C_{16}K_1$ assemblies in [NaCl]=20mM with amount ratios of L:D molecules. For 100% L-$C_{16}K_1$, oscillatory features of cochleate assemblies are present in the scattering pattern (3.2A, bottom), consistent with [73] (1.3.1). A peak at $q = 0.3$nm^{-1} corresponds to a D-spacing of the cochleate lamella of 20.9 nm (black dashed ellipse in Figure 3.2A). Upon increasing the relative amount of D-$C_{16}K_1$ to L-$C_{16}K_1$ molecules, certain scattering features are observed. 1) The cochleate oscillatory features are absent in the racemic mixture (%L:%D$\simeq$1:1, 3.2A, top). This supports the finding that the packing of the chiral molecules is what drives the chiral assembly process. Consider the classical analogy of the packing of screws. Opposite handed screws can pack closely within the grooves of an opposite handed neighbor. However, like-handed screws can only align their grooves by implementing a slight twist with respect to their neighbors. This ”molecular” twist is what gives rise to the meso-scopic twist in the ”screw” assemblies. 2) The diffraction peak position corresponding to the D-spacing of the cochleate assemblies (illustrated in Figure 3.2B) remains constant ($q = 0.3$nm^{-1}) for all ratios of %L:%D.

To model consequences of the latter finding, we implement the Helfrich-Prost free energy for cochleate assemblies described in [73], see 1.3.3. For a constant D-spacing, minimization of A.14 leads to cochleate of increasing radii for decreasing chiral coupling strength. Parameters used in the minimization include a maximum chiral coupling $\lambda_0 = 0.348 \times 10^{-11}$, bending rigidity $\kappa = 160 \times 10^{-21} = 39\, k_BT$, D spacing $D = 20.9$ nm and radius at $\lambda/\lambda_0 = 1$ of $R_0 = 173$ nm. Such parameters are consistent with previous implementations of the model [73]. Results of the minimization are shown in 3.2C. Tighter cochleates (smaller radius) with multiple lamella layers

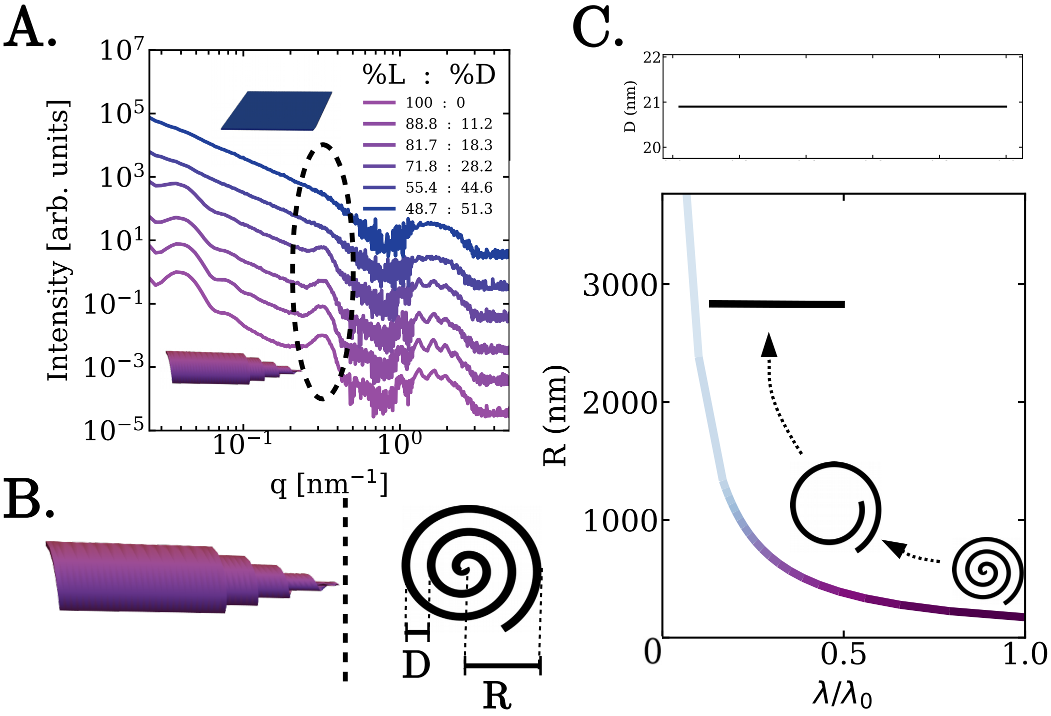

Figure 3.2: **A.** SAXS/WAXS patterns for C$_{16}$K$_1$ assemblies in [NaCl]=20mM for varied ratios of L- and D-C$_{16}$K$_1$ molecules. For 100% L-C$_{16}$K$_1$, the chiral coupling λ is maximum ($\lambda = \lambda_0$) and we observe prominent cochleate features. The peak at $q = 0.3$ nm^{-1} represents a D-spacing$=$ 20.9 nm of cochleate lamella shown by the schematic and cross-section of cochleate assemblies shown in **B.** With a decrease in the chiral coupling by an increase in ratio of D-C$_n$K$_1$ to L-C$_{16}$K$_1$ molecules, cochleate features are dimished until finally disappearing in the racemic mixture.**C.** For a fixed D-spacing (top), minimization of H_T shown in 1.3.3 results in a cochleate radius (bottom) that increases with decreasing chiral coupling strength. A proposed transformation pathway from cochleate to flat bilayer for fixed D-spacing is shown.

are formed by C$_{16}$K$_1$ molecules at $\lambda = \lambda_0$, or 100% L-C$_{16}$K$_1$ molecules in assemblies. Upon increasing the relative amount of D-C$_{16}$K$_1$ in assembly, the cochleate gradually increase in radius, leading to a decreased amount of lamellar overlap. This is consistent with the decreased intensity of the lamellar peak in 3.2A for decreased chiral coupling strength. Specifically, at a reduced chiral coupling strengh of $\lambda = \lambda_0/2$, the cochleate radius has increased from $R_0 = 173$ nm to $R = 379.6 \simeq 2R_0$ nm. At a certain point ($\lambda/\lambda_0 \simeq 0.25$), the radius diverges, consistent with flat bilayer structures which have zero curvature (infinite radius). Previously, studies have suggested applications of cochleate assemblies to drug delivery [12]. Our new finding pathway proposes methods of controlling amounts of encapsulated molecules by varying the number of enantiomers in a given assembly, which have a controllable degree of lamellar overlap.

3.3.2 C$_n$K$_1$ Ionization Behavior

3.3.2.1 C$_{18}$K$_1$ Helical Ribbon Characterization as a Function of pH

We performed in-situ SAXS/WAXS measurements of 4mM C$_{18}$K$_1$ solutions at varying pH from pH=4-11. Similar to 2, we fit the scattering patterns to helical ribbon bilayers helical bilayer membrane model depicted in Figure 2.3D. We have analyzed the measured scattered intensity from helical ribbons using the multilayer helical membrane form factor, which is an extension of the Pringle and Schmidt model [92, 93] (eqs 2.2 and 2.3). 3.3 shows the measured scattering profiles of C$_{18}$K$_1$ assemblies and model fits to the profiles. Specific helical ribbon parameters are shown in 3.1.

The transformation pathway for C$_{18}$K$_1$ is similar to C$_{16}$K$_1$ transformation pathway described in 2.3C. When initially put in pure water, where the C$_{18}$K$_1$ are expected to be in their ionized form, C$_{18}$K$_1$ molecules form flat semi-crystalline bilayer assemblies with of total thickness $t = 4.57$ nm (3.3, bottom), based on a three-slab form factor fit to the scattering profile. Such a thickness is consistent with previous measurements of bilayer thicknesses of C$_n$K$_1$, n<18 assemblies discussed in earlier chapters of this text. Electron densities used for the fit are $\rho_h = 410$ e/nm^2, $\rho_t = 318$ e/nm^2, and $\rho_{solv} = 334$ e/nm^2 where ρ_h corresponds to the electron density of the headgroup region, tail

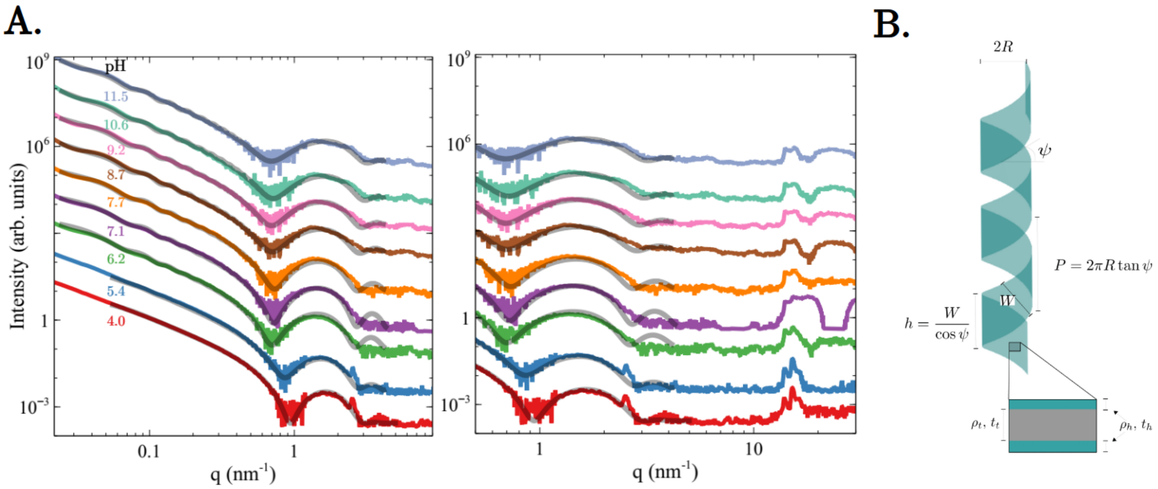

Figure 3.3: **A.** Scattering profiles for C$_{18}$K$_1$ molecules at various pH with corresponding form factor model fits (black overlay). At low pH (pH=4), C$_{18}$K$_1$ form flat bilayers that transform into helical ribbons upon in increase in pH with specific structural features including pitch angle ψ, radius R, width W, and bilayer thickness and electron densities described in **B**. Parameters for fits are shown in 3.1.

region, and surrounding solvent respectively. Upon an increase in pH, C$_{18}$K$_1$ bilayer ribbons twist into helical ribbon assemblies characterized by a radius R, pitch angle ψ, pitch p, width W, height to pitch ratio h/p, bilayer thickness t, and electron densities 3.3B. For all helical ribbon fits, a constant polydispersity of 10% is assumed. For pH=5.4 (3.3A, blue), a weighted form factor fit is used with 35% helical ribbon at pH=6.2 and 65% of flat bilayer at pH=4.0. In this way, we continuously capture the transformation from flat bilayer into helical ribbon.

Certain trends in the helical fit parameters for C$_{18}$K$_1$ are notable. 1) The width and radius both increase as a function of pH, in a manner similar to C$_{16}$K$_1$ helical ribbons described in [61]. As the width of the helical ribbon increases, the necessary bending energy required for twisting increases. With an assumed constant chiral twisting force due to the C$_{18}$K$_1$ lysine headgroups, this leads to an overall decrease in curvature (i.e. larger radius). 2) The bilayer thickness and electron density of the tail region decrease as a function of pH. This could be due to decreased degree of order and crystallinity of C$_{18}$K$_1$ assemblies at higher pH as C$_{18}$K$_1$ assemblies transform from ribbon to helical ribbon. Notably, diffraction peaks corresponding to molecular ordering (15<q<18 nm^{-1}) are

Table 3.1: $C_{18}K_1$ helical ribbon fit parameters

pH	R [nm]	h/p	W [nm]	ψ	ρ_t [e/nm^{-3}]	t [nm]	p [nm]
6.2	72.5	0.48	123.4	0.60	318	4.35	311.6
7.1	73.7	0.45	122.8	0.63	318	4.42	337.6
7.7	74.0	0.52	134.5	0.59	318	4.29	311.3
8.7	75.7	0.54	145.0	0.60	313	4.17	325.4
9.2	76.4	0.53	143.7	0.60	310	4.05	328.4
10.6	79.8	0.54	166.0	0.66	308	3.91	389.1
11.5	77.1	0.54	154.1	0.63	303	3.78	353.2

visible throughout the flat ribbon to helical ribbon transformation for $C_{18}K_1$. Therefore, the degree of ordering and crystalline lattice structure could in principle be modelled continuously for changing pH. This will be a part of future work.

3.3.2.2 C_nK_1 Titration Curves, n=10,18

In a similar manner to 2.3.1, we describe and discuss the relationship between pH and degree of ionization for C_nK_1 for n=10-18 by looking at measured titration curves. To further understand how the coupling between attractive van der Waals interactions and repulsive eletrostatic interactions affect the degree of ionization in C_nK_1 assemblies, we performed titrations for $C_{10}K_1$ and $C_{18}K_1$. We titrated 5 mL of a 4 mM L-$C_{18}K_1$ solution in pure water with a 0.1 M NaOH solution. For $n = 10$, the reduced hydrophobic tail length reduced the tendency of the amphiphilic molecules to assemble together leading to an increased critical micelle concentration. 4mM $C_{10}K_1$ lead to no observable assemblies in SAXS. Therefore, we titrated 5mL of 40mM $C_{10}K_1$, an order a magnitude higher than that for $n \geq 12$.

Figure 3.4A shows the measured titration curves for C_nK_1 for all n=10-18. These titration curve are modeled with the empirical Hill equation eq 2.1, as was done in 2.2. The best fit parameters are listed in Table 3.2. These measurements and the analysis show that the pK_a and location of the buffer region monotonically decreases with increasing n for n = 10-18 (Figure 3.2). Certain trends are apparent. 1) pK_a values increase for for decreasing tail length, from pK_a = 6.70, 7.66,

Table 3.2: C$_n$K$_1$ titration fit parameters

Tail Length (n)	Nominal Conc. [mM]	Fit Conc. [mM]	pK_a	m
10	40.0	40.0	9.10	1.40
12	4.0	4.0	8.69	0.92
14	4.0	3.2	8.01	0.60
16	4.0	3.3	7.66	0.63
18	4.0	2.0	6.70	0.43

8.01, 8.69, to 9.10 for n = 18, 16, 14, 12, and 10, respectively (3.2). Reducing the number of carbons in the alkyl tails enhances the propensity of the molecules to remain ionized as seen from the degree of ionization plots in 3.4B. Similarly, more rigid and crystalline packed structures are expected for increasing tail length due to van der Waals attractions which would lead to more closely packed charged assemblies. To accommodate the packing, molecules will tend to be deionized at pH values far below the individual site pK_a=p$K_{a,lysine} = 10.5$ [85]. 2) The Hill coefficient (m) increases for decreasing tail length. For $n \geq 14$, assemblies of C$_n$K$_1$ molecules show strong anti-cooperativity ($m < 1$) between ionizable sites which is due to the close packing of the lysine headgroups in different assemblies. The anti-cooperativity is most prounounced for $n = 18$ where $m = 0.43$. In the tightly packed, crystalline C$_{18}$K$_1$ assemblies (Figure 3.3A), it is electrostatically unfavorable for the headgroups to be in there protonated, charged state. For $n = 12$, the Hill coefficient approaches 1, corresponding the reduced cooperativity between sites. For $n = 10$, the Hill coefficient $m = 1.40$ is much greater than 1, indicating cooperativity between sites. That is, ionization of one individual lysine site increases the propensity of ionization of another site. This is manifested with a titration curve buffer region that is flatter than standard Henderson−Hasselbalch curves (Figure 3.4A, orange) which is observed in titration curves of assembly of amino acids in proteins [115]. This leads to a sharp, approximately step-wise, change in the degree of ionization at pH$\simeq$p$K_a = 9.10$ (Figure 3.4B, orange).

Interesting to note is the stark difference in titration curves between C$_{18}$K$_1$ and C$_{16}$K$_1$ which show similar assembly transformations pathways as a functions of pH (Figure 3.3, Figure 2.3C). C$_{18}$K$_1$ molecular assemblies have stronger intermolecular van der Waals attractions due to the

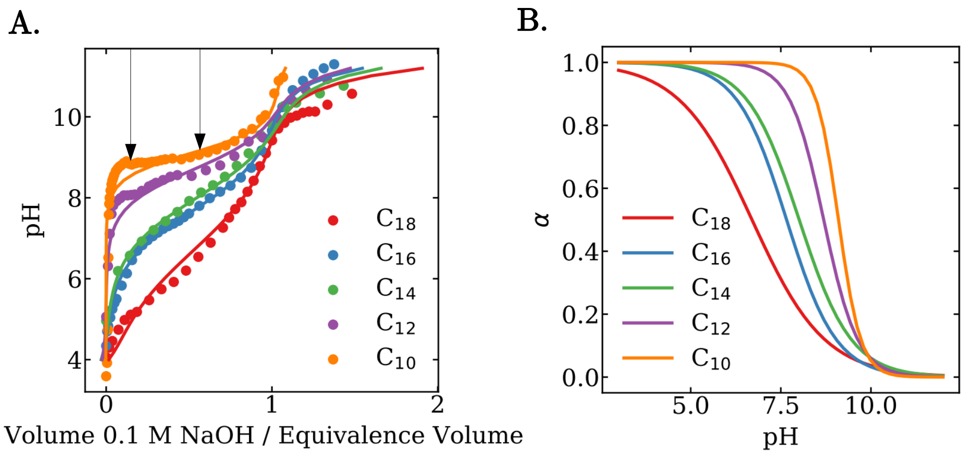

Figure 3.4: **A.** pH titration curves for 4mM C_nK_1 in pure water for n = 10, 12, 14, 16, and 18 along with fits based on the empirical Hill equation. Horizontal axis is the volume of NaOH with respect to the equivalence volume, defined as the point at which the derivative of the pH with respect to volume of NaOH is maximum [86]. Arrows indicate $C_{10}K_1$ cryo-TEM samples shown in Figure 3.5D. **B.** Corresponding degree of ionization vs pH deduced from Hill fits in **A.**

increased tail length of the molecules. This causes $C_{18}K_1$ to form more closely packed assemblies with increased degree of ordering as can be seen in the WAXS region ($q > 15$) of the scattering profiles (Figure 3.3A, right). While weakening in intensity with increasing pH, diffraction peaks arising from positional correlations of the tails persist throughout the helical ribbon transformation, which was not the case for $C_{16}K_1$ bilayers and helical ribbons (Figure 3.3A,[61]). Therefore, to reduce intermolecular headgroup electrostatic repulsions that are enhanced with the crystalline packing of the tails, there is a stronger tendency for the headgroups to be in their uncharged, deionized state.

Unclear is the differences between the nominal and fit concentrations used for $C_{14}K_1$, $C_{16}K_1$, and $C_{18}K_1$. In [61], it was suggested $C_{14}K_1$ and $C_{16}K_1$ differences in concentrations between the model and experiment could be due to imprecise measurement of difficult to handle powdery and flaky sample. However, the $C_{18}K_1$ fit concentration of different by a factor of 2, larger than any reasonable uncertainty in the measurement of sample. It is possible that the initial concentration used in fitting procedures is related to the initial fraction of charged C$_{16}$K$_1$ molecules, and not the total number of molecules. Future studies will focus on robustly quantifying the degree of ionization behavior for PA systems like C$_n$K$_1$ based on explicitly modelling the electrostatics to remedy this finding.

3.3.2.3 C$_{10}$K$_1$ Twisted Ribbon Assemblies

The intricate coupling between molecular packing/order and chiral assembly has been demonstrated experimentally, but theoretical models disagree on the degree of crystallinity in chiral lipid membranes and there is experimental evidence both for and against crystallinity in the assemblies [17]. An example demonstrating the importance of molecular ordering in chiral assemblies is diacetylenic phospholipids. The achiral spherical vesicle is the equilibrium morphology for the membranes in the high temperature fluid phase (molten lipid tails, Lα phase). By contrast, these same membranes in the low temperature condensed phase (tightly packed tilted lipid tails, Lβ' phase) bend into chiral tubules [19]. Studies have suggested that a twisted ribbon chiral morphology will become the more favorable when bilayers are more fluid [9, 23]. We hypothesized that decreasing the van der Waals attractions by decreasing the tail length of C$_n$K$_1$ molecules should reduce the rigidity of the bilayer structures (see 2.3.4). This hypothesis was supported by MD simulations to be discussed in the following section. Therefore, we suspected twisted ribbons should be a more favorable assembly morphology compared to the helical ribbon for short tailed C$_n$K$_1$ lipid molecules.

We considered C$_{10}$K$_1$. Visualizations of 40mM C$_{10}$K$_1$ ((pK_a = 9.1) twisted ribbons and stacking of the twisted ribbons can be seen in the cryo-TEM images shown in Figure 3.5D at pH = 8.8 (red) and pH = 9.3 (blue). Highlighted in the images are the twisting nodes of the high aspect ratio twisted ribbons (Figure 3.5D, white arrow) and the appearance of a one or multiple lamella in the twisted ribbon assembly (Figure 3.5D, white circle). The in-situ SAXS/WAXS profiles corresponding to these measurements show diffraction peaks in the $1.5 < q < 4$nm^{-1} and $15 < q < 18$nm^{-1} range due to crystalline features of the assemblies (Figure 3.5A,B). The lower q peaks arise from multiple bilayer structure of the twisted ribbons. Those peaks correspond to the first (n=1, $q_1 = 1.78$nm^{-1})

and second (n=2, $q_1 = 3.58$nm^{-1}) order diffraction peaks resulting from a $\frac{2\pi}{1.78} = 3.53$ nm lamella spacing of bilayer stacks (Figure 3.5C). Since the pH is around the pK_a of C$_{10}$K$_1$ molecules, large changes in the ionization state of C$_{10}$K$_1$ molecules are expected with small changes in the pH (Figure 3.4B). As the pH is increased and the pK_a is approached, the C$_{10}$K$_1$ molecules become deionized and the stacking behavior C$_{10}$K$_1$ becomes more prominent. A secondary doublet feature is associated to each order q_1 stacking peak (n=1, $q_2 = 1.89$nm^{-1}; n=2, $q_2 = 3.81$nm^{-1}). As of now, it is unclear what is responsible for this doublet feature. In order for such a feature to be present, there must be some

The q peaks at $15 < q < 18$nm^{-1} correspond to crystalline lattice structure of the C$_{10}$K$_1$ hydrophobic tail regions [61]. This result is surprising as the twisted ribbon morphology is not to be expected for crystalline assemblies due to large energetic consequences resulting from Gaussian curvature [9, 23]. However, our finding suggests that C$_{10}$K$_1$ twisted ribbon assemblies do indeed have crystalline ordering at both the molecular (sub nm) and assembly (100 - 1000 nm) length scales. This finding shows that the C$_{10}$K$_1$ molecular provides a simple and suitable system for analyzing the coupling between positional correlations and intermolecular forces without complications that arise in similar systems such as enhanced hydrogen bonding [52]. Such investigations will be a focus of future work.

3.3.3 Martini PW Molecular Dynamics for Bending Rigidity

In [61], it was shown that the radius of C$_n$K$_1$ helical ribbons increased with decreasing tail length (for n=12,14 and 16). One would expect the the bending rigidity of C$_n$K$_1$ bilayers follows the sequence $\kappa_{C_{12}} < \kappa_{C_{14}} < \kappa_{C_{16}}$ due to increased attraction of the tails that results from longer tails. However, models for helical ribbons of chiral molecules suggest that $R \sim \frac{\kappa}{\lambda_{HP}}$ ([17], see 0.2.3), resulting in a decreasing radius with decreasing tail length. The opposite effect to is observed for C$_n$K$_1$ helical ribbon assemblies. However, we note there are many details that affect the intricate coupling between molecular packing/order and chiral assembly [116] with different models focusing on different aspects including models which can lead to an anomalous scaling of the helical radius

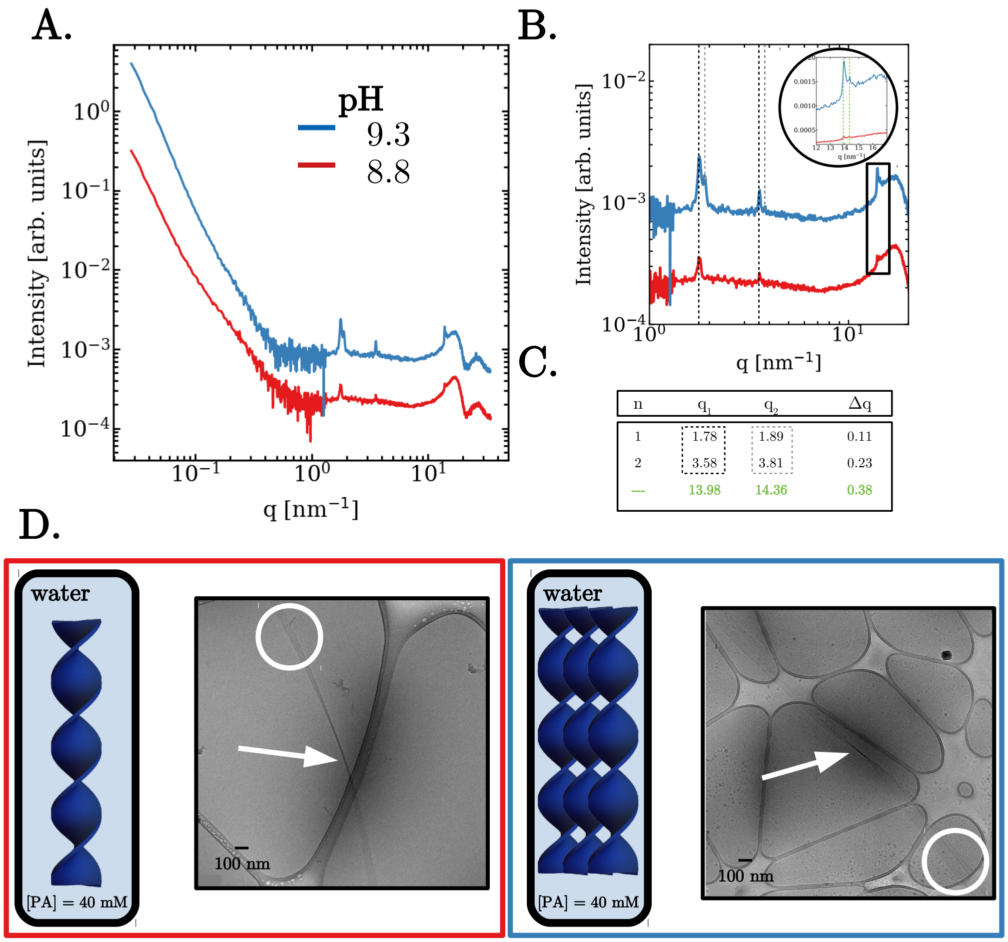

n	q_1	q_2	Δq
1	1.78	1.89	0.11
2	3.58	3.81	0.23
—	13.98	14.36	0.38

Figure 3.5: **A.** Scattering profiles for 40mM $C_{10}K_1$ assemblies at pH=8.8 and pH=9.3. Pronounced doublet stacking peaks appear at $1.5 < q < 4$nm^{-1} corresponding to stacking behavior of twisted ribbons. In addition, diffraction peaks at $15 < q < 18$nm^{-1} signify crystalline packing of $C_{10}K_1$ molecules. **B.** Detailed analysis of peaks in the low and high q regimes. listed in **C.** **D.** Cryo-TEM images of $C_{10}K_1$ twisted ribbons at pH = 8.8 (red) and pH = 9.3 (blue). Arrow points to the twisting node of a twisted ribbon. Circle highlights the difference between an individual twisted ribbon (red) and stacked twisted ribbon (blue) as shown in the schematics to the left.

that increases with increasing rigidity [17, 37].

In order to understand how the charged interactions affect the bending rigidity of C$_n$K$_1$ bilayer structures, we performed coarse grained molecular dynamics (MD) simulations using the Martini 2.2P force field described in 3.2 [105, 117]. Martini is a coarse-grained (CG) force field suitable for MD simulations of (bio-)molecular systems. It is based on mapping of two to four atoms (excluding hydrogen) to one CG particle. It allows the investigation of the behavior of large lipid membrane systems at spatial and timescales unachievable to atomistic MD simulations, while retaining enough resolution to give a microscopic and dynamic picture still unavailable in experiments [118]. In addition, extensions of the force field have led to success in decscribing amino acid interactions [113]. For these reasons, it is an suitable force field to use for C$_{16}$K$_1$ lipid molecules. It is worth noting that this force field parameterization, which does not contain a chiral center for the lysine amino acid, will inherently lose all any possible steric packing effects due to chirality. However, differences between L- and D-C$_{16}$K$_1$ are mentioned in C.1. Parameterization of the C$_{16}$K$_1$ molecule in the Martini 2.2P force field is shown in C, Figure C.2.

Atomistic representations of the C$_n$K$_1$ molecules were mapped from the CHARMM36 force field to the Martini 2.2P forcefield to preserve bond angle and length relationships (see C.2). 1000 C$_n$K$_1$ lipid molecules assembled in a bilayer structure were simulated for $\sim$250 ns after initial mizimization and equilibration. Some percentage of the molecules have their headgroups in the charged, ionized state while the remaining are uncharged, corresponding to different fixed charged percents of the bilayers throughout the simulations. Example bilayers for C$_n$K$_1$ with 40% of the headgroups are charged are shown in 3.6A-D corresponding hydrophobic tails of n = 8, 12, 16, and 20 carbon atoms or 2, 3, 4, and 5 Martini CG beads. Density plots across the bilayer normal (z-axis) shown to the right of each bilayer with $z = 0$ centered at the midplane of the bilayer demonstrate diffrences in the bilayer constiuents for different tail lengths. C$_{20}$K$_1$ bilayers shown strong sharp head group density peaks (blue) and tail region plateaus (gray) corresponding to highly stable and rigid bilayer structure (Figure 3.6D). These peaks broaden with decreasing tail length and for n = 8, molecules are found entirely dissociated from then bilayer, free in solution (Figure 3.6A). Counterion profiles (green) show a highly condense region of ions near the headgroup peaks as to be expected for

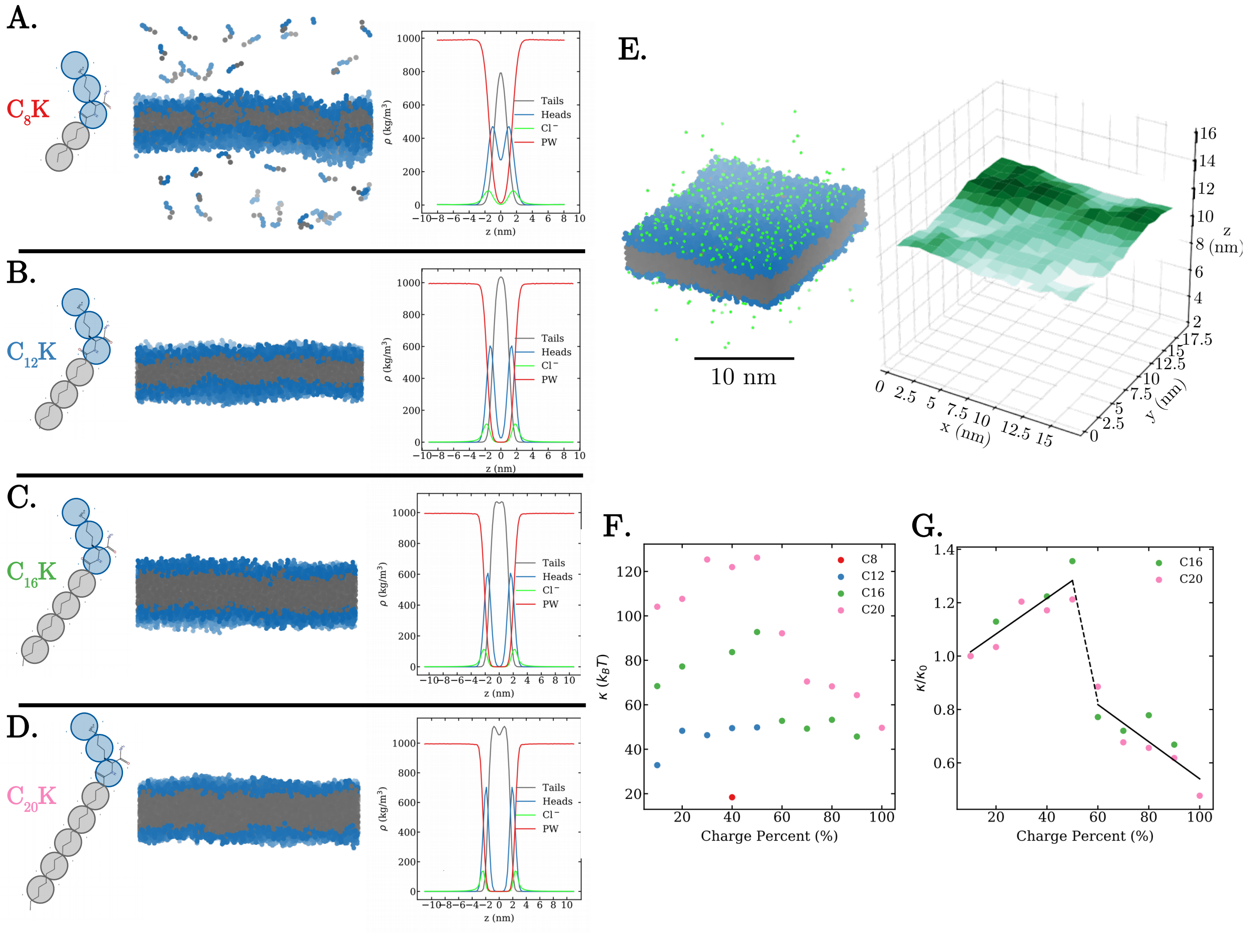

Figure 3.6: Martini coarse grained representations of C_nK_1 molecules and bilayer assemblies of the molecules with corresponding density plots across the bilayer normal (z-axis) for **A.**C_8K_1, **B.** $C_{12}K_1$, **C.**$C_{16}K_1$, and **D.** $C_{20}K_1$. All examples are shown for bilayers where 40% of the headgroups are in their charged stated. **E.** Full $C_{16}K_1$ Martini bilayer at 40% charge with scale bar for reference. A sheet representation of the average height of the same bilayer used for calculation of the bending rigidiy κ is shown to the right where the 1000 molecule bilayer is divided into $16\times16=256$ cells**F.** Bending rigidities for C_nK_1 Martini bilayers for different tail lengths (Cn) and charge percents (x-axis). **G.** Bending ridigities for $C_{16}K_1$ and $C_{20}K_1$ bilayers normalized by their respective bending rigidities at charge percent of 10%. Black lines show trends in the bending rigidities as a function of charge percent.

highly charged assemblies [119]. In addition, the water density plateaus at 1000kg/m^3 as expected for pure water.

We use linearized Helfrich theory to extract the bending rigidity of the bilayer [120, 121, 122, 123]. Derived from a free energy containing only a bending energy term ($F \sim \frac{\kappa}{2}C^2$, where C is the mean curvature), this fluid approximation of the membrane is appropriate for the CG bilayers which, by construction, lack chirality and therefore chiral interactions like the second term of eqn 7. The method is based on looking at fluctuations in the height profile of the bilayer over time, akin to the experimental technique flicker spectroscopy which can be used to estimate the bending rigidity of micelles [124]. This theory predicts a spectrum

$$L_x L_y \langle |h_q|^2 \rangle = \frac{k_B T}{\kappa q^4 + \Gamma q^2} \simeq \frac{k_B T}{\kappa q^4} \tag{3.1}$$

with $h(x, y) = \sum_{qx,qy} h_{q_x,q_y} e^{i(q_x x + q_y y)}$ being the vertical position of the (x, y) point of the bilayer measured from a reference plane. κ is the bending rigidity; Γ is the lateral tension, which is approximately zero for all bilayer simulations (i.e. tensionless membranes at equilibrium), and L_x,L_y ($L_x L_y \simeq L^2$) are the linear of the bilayer in the x and y directions, respectively . $\langle \ldots \rangle$ indicates the ensemble average. The system was divided in a grid of 16×16 cells as shown in Figure 3.6E. For each cell grid, we found the average position in the z direction of all beads belonging to that grid. We obtained h_q by computing fast Fourier transform of the height map, $h(x, y)$. The $|h_q|^2$ was averaged over approximately 500 different simulation snapshots over the coarse of the 250ns simulation.

Figure 3.6F shows the measurements of κ at different charge percents for C$_n$K$_1$ for different tail lengths. All bilayer bending rigidities (κ) are within 20-120 $k_B T$, consistent with measurements of κ for lipid systems [29, 125, 126, 127]. At low charge percents ($\leq$40%), the bending regidity increases with increasing tail length, as expected with the increased van der Waals attraction of the tail regions. Specfically, for C$_{12}$K$_1$, κ is measured to be around 50$k_B T$ which then increases by $\sim$ 30$k_B T$ for each additional Martini CG carbon tail bead, corresponding to 4 additional carbon atoms (Figure 3.6F). Such a finding verifies are initial hypothesis of increasing membrane fluidity

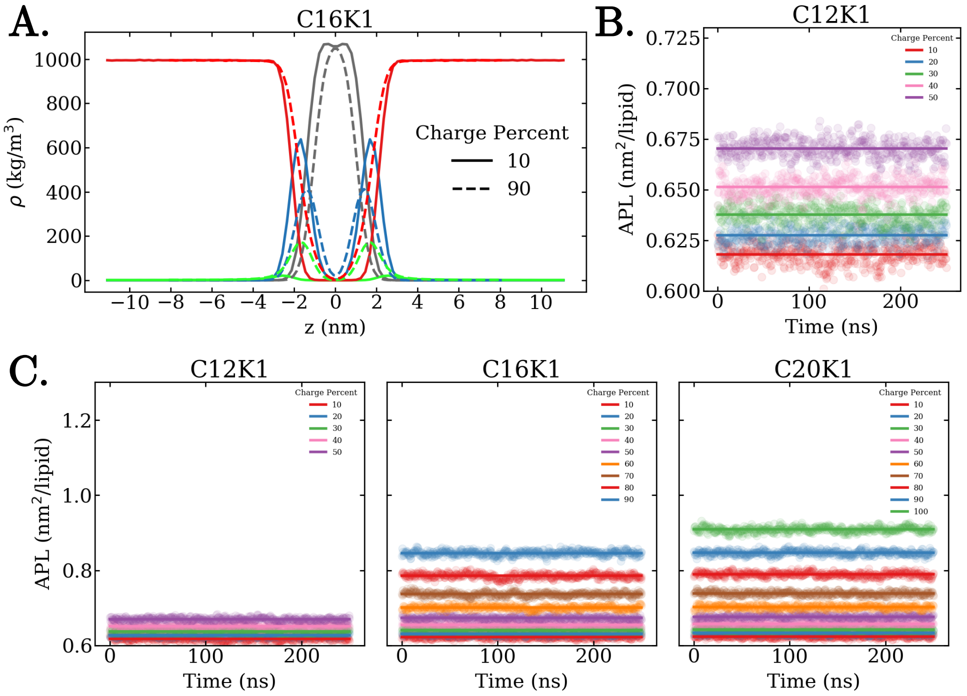

Figure 3.7: A. $C_{16}K_1$ density plot for 10% and 90% charged bilayers. Excess water density (red) is found within the headgroup density peaks (blue) at larger charge percents. Tail region (gray) plateau is absent at higher charge percents and is replaced by a peak. Counterion density (green) are increased for larger charge percents to maintain electroneutrality. **B.** Area per lipid (APL) increases with increasing charge percent for $C_{12}K_1$ bilayers. **C.** The effect is more pronounced for $C_{16}K_1$ and $C_{20}K_1$, where all APL measurements are shown to scale for comparison across tail length. There is no recognizable change in area per lipid between tail lengths of stable bilayer simulations.

by decreasing the tail length for C_nK_1 assemblies. Interestingly, there is abrupt decrease in κ at $50-60$% charge for $C_{16}K_1$ and $C_{20}K_1$ bilayers. We note that pH$\simeq$pK_a would correspond to 50% of the C_nK_1 molecules in their charged, ionized state. Electrostatic interactions have a nonmonotonic effect on κ. Upon scaling of the bending rigidities by κ_0, the bending rigidity at 10% charge, there appears an initial increase in the bending rigidity by followed by an abrupt drop at 50% charge, followed by a gradual decrease to around $\kappa/\kappa_0 \simeq 0.6$ (Figure 3.6G).

Absence of points in 3.6F is due to the inability to produce stable bilayers with a certain molecule at the given charge percent. For example, only bilayers of 40% charge were stable for C_8K_1 Martini simulations. Reasons for this may be due to limitations of the Martini CG force field in reproducing the crystalline ordering that is observed for C$_n$K$_1$ molecular assemblies. Although the MARTINI simulation model has a number of potential advantages, it has been found that it can lead to excessively strong (favorable) interactions between proteins (amino acids) in aqueous solution known as the ”stickiness” problem [112, 128]. Using the polarized version was an attempt to better capture the interactions of the charged lysine amin acid with the surrounding solution. However, this stickiness still seems to cause an overhydration of the lysine amino acid headgroups as water densities are high within the bilayer headgroup regions. This is manifested in a large increase of the area per lipid (APL) at higher charge percents shown in 3.7C, approximately calculated by $\frac{L_x L_y}{1000}$. In addition, interdigitation, reproducible in atomistic simulations [61], is considered to have a consolidation effect for membrane structures as it results in highly ordered packing [129]. Martini CG simulations were unable to reproduce ordered interdigitation effects. In general, constant, fixed charge simulations are limited in their application to charge regulation processes which are dynamically related to the pH of the solution occurring in assemblies of ionizable molecules, like C$_n$K$_1$. Recently, a Martini charge regulating model known as Martini Sour (titratable Martini) was developed for simulations of ionizable molecules at constant pH [112, 130, 131, 132]. Attempts to simulate C$_{16}$K$_1$ with Martini Sour are shown in section C.3. Nevertheless, such a trend in the bilayer bending rigidity present preliminary efforts in measuring elastic properties of C$_n$K$_1$ bilayer assemblies.

3.4 Summary and Future Work

In conclusion, this chapter has described the success of C$_n$K$_1$ as a simple and suitable molecular system for the exploration of the charged, chiral assembly phase space. We have provided descriptions of a variety of findings including: (1) the generality of the cochleate structure for $n \neq 16$ was tested and the control of $n = 16$ scroll-like cochleate assemblies properties by varied levels of enantiomers (L-/D-C$_{16}$K$_1$) in the assembly was proposed, (2) the ionization tendencies of C$_n$K$_1$ assemblies was analyzed through the measurement of titration curves, (3) the morphology and crystallinity of helical ribbon assemblies of C$_{18}$K$_1$ molecules and twisted ribbon assemblies of C$_{10}$K$_1$ was analyzed and characterized, and (4) coarse MD simulations provided insights into the elastic properties and nanoscale details of C$_n$K$_1$ bilayer assemblies. Future work will focus on refined characterization of each of these preliminary findings as well as further exploration of the chiral shape phase space of C$_n$K$_1$ assemblies.

4 Chapter 4

“The important thing in science is not so much to obtain new facts as to discover new ways of thinking about them.”

-Sir William Lawrence Bragg

The previous chapters have illustrated the precise interplay between chiral and electrostatic forces in charged, chiral molecular assemblies. This chapter focuses on a similar molecular system, $C_{16}K_2$, where the electrostatic interactions play a dominating role over the relatively weak chiral interactions. Such molecular assemblies are observed to be achiral. The study aims to gain a better insight into the electrostatics of soft ionizable assemblies.

4.1 Introduction

Electrostatic interactions play a fundamental role in soft matter and bio-physical systems [133]. Many bio-molecules and bio-materials have non-zero charge in solution. This phenomenon results from the association and dissociation of ionizable molecular fragments. In aqueous suspensions, these certain molecular groups can become ionized and that ionization state depends on the ionic conditions of the surrounding solution environment. For example, the amino acids that constitute proteins have ionizable carboxyl and ammonium groups which can be protonated and deprotonated depending on the pH of the solution in which they are suspended. Thus, understanding ionization behavior is vital to studies of biological assemblies. The ionization (protonation) state is controlled by the chemical equilibrium between hydronium ions (pH$= -\log_{10}[\mathrm{H}^+]$) and the functional groups described. In general, this ion-exchange process is known as charge regulation (CR) [31, 134, 135]. Recent studies have focused on incorporating CR effects into computational models for charged soft matter due to their importance in colloidal and bio-molecular assemblies [30, 136, 137] The CR process can lead to nano-scale structural changes in assemblies of ionizable molecules. When ionizable molecules are in assembly, their ionization tendencies change due to interactions with their ionizable neighbors. One way to assemble such molecules is to couple them to non-polar components which prefer to be shielded from the surrounding solution, e.g. alkyll chains. The combined hydrophobic and hydrophillic properties cause the molecules to self-assemble into different energy minimizing equilibrium structures depending on the ionization state of the head group. For example, peptide amphiphiles (PAs) are a general class of biocompatible and biodegradable protein-based amphiphillic materials whose assembly structure depends directly on the ionization state of the head groups of the constituent molecules [52, 75]. Fascinating, and controllable, hierarchical structures including nanotubes, helical and twisted membranes, and scroll-like assemblies can be generated by tuning PA charged components [20, 61]. PA molecular assemblies are of particular interest due to their potential biochemical engineering applications, such as bioartificial nerve conduits [103].

In proteins, protonatable residues can be rarely separated from each other. They mutually interact more or less strongly. A sign of this interaction is that titration curves of amino acids in proteins are often flatter than standard Henderson−Hasselbalch curves (1) or show even an irregular shape. (2-4) It follows that half-points (pH at which the protonation probability is 50

Typically, ionization states of molecules are characterized by an ion dissociation constant, or pK_a, which is used to estimate the fraction of ionized sites at a given pH, commonly labelled α (the degree of ionization) [40]. Experimentally, one measures pK_a values through titrations of the molecule of interest and application of acid-base equilibrium models such as Henderson-Hasselbach (HH), or Langmuir model [138, 139, 140]. The HH model is useful for characterizing solutions of dilute, non-interacting ionizable molecules. However, when ionizable molecules are gathered into larger supra-molecular assemblies, the HH model fails to capture changes in ionization behavior [141]. For example, in proteins, which consists of a large number amino acids and protonatable sites, protonable sites cannot be separated from one another and titration curves show irregular shapes [115, 142]. pK_a values shift due to cooperativity between the ionizable sites and ionization behavior does not follow the HH approximation leading to classifications of experimental titration curves with an effective p$K_{a,\,\text{eff}}$.[143] The observed pK_a shifts result from the binding process of small electrolytes (e.g. H^+ or OH^-) to an ionizable molecule becoming highly correlated with the electrostatic potential generated by other ionizable molecules in the molecular assembly [144]. To account for deviations, the Hill model is typically employed which includes an extra parameter known as the Hill coefficient that quantifies the cooperativity of ionizable sites [145, 146, 147, 148]. It is commonly used for quantitative analysis of drug-receptor interactions and gating models of ion channels in the medical sciences [149, 150]. Despite accurately fitting experimental titration data, intuitive understanding and physical mechanism for observed changes in titration behavior are lacking. As this cooperativity between ionizable sites has an electrostatic origin, a more appropriate approach to analyzing titration behavior of ionizable molecules in assembly is to directly incorporate electrostatic interactions.

The relationship between the charge distribution of ions in solution and the structure of the aggregate necessitates a self-consistent solution for the electrostatic potential and degree of ionization. Within the mean-field Poisson–Boltzmann (PB) formalism, this is known as the CR boundary condition [134, 151, 152]. One can stipulate the isolated pK_a of the molecule, the number density of molecules, ionic condition of the solution, and the size/geometry of the assembly and then self-consistently solve for the ionization state of the molecular assembly. In this way, one can capture the interdependence of the ionization state of the molecules with the morphology of the assembly and ionic environment. Studies have demonstrated the success of PB for describing charge of biomolecular systems of simple geometries [153]. Despite this, a study of a system describing the coupling of assembly geometry and charge regulation in relation to experimental titration measurements is lacking. Achieving this combination requires precise characterization of the nano-scale structure of the aggregates as well as an appropriate experimental system.

To address this, we designed a PA $C_{16}K_2$ consisting of a two ionizable amino acid headgroup (lysine, K) that is covalently coupled to alkyl tails consisting of sixteen carbon atoms (4.1A). Polylysine amphiphiles $C_{16}K_n$ (n = 1–3) have been explored in the past in the context of antimicrobial properties [76]. The molecular charge can be tuned via pH as one protonates and deprotanes the lysine head group side chains and the range of electrostatic interactions (screening length λ_D) can be controlled by adjusting the salt concentration ([NaCl]) (4.1B,C). Previous work using X-ray scattering, microscopy, and theoretical techniques revealed that the molecular design of $C_{16}K_2$ and adjustments of pH result in assembly structures including micelles, cylindrical micelles, and planar assemblies [14, 86]. Such shapes are tractable within the PB formalism[154] making $C_{16}K_2$ an appropriate experimental system. A nonlinear PB electrostatic model was employed to extract the shape and size-dependent degree of ionization and compared directly to experimental tirations. Table 4.1 shows the comparison of the degree of ionization (α) for the electrostatic model with the HH and Hill models. In this way, we aim to accurately model charge of the PA assemblies and show the effect of assembly geometry on the degree of ionization without adjustable parameters. The advantages to our approach to understanding CR lie in the detailed in-situ characterization of the assembly nano-scale structure using X-ray scattering and the direct comparison of a simple PB model for electrostatics to experimental titration measurements. We found our model can accurately reproduce titration behavior in low ionic strength using only structural information about the assemblies without adjustable parameters. In addition, we demonstrate the effects of spherical, cylindrical, and planar assembly geometries on the degree of ionization in soft-ionizable assemblies.

The rest of the chapter is organized in the following manner. We first present the experimental methodology consisting of small-angle X-ray scattering (SAXS), titration, and Zeta (ζ) potential measurements. We then outline the self-consistent electrostatic model for titration measurements. The results and discussion consist of 3 subsections: (1) characterization of $C_{16}K_2$ assembly structure in different ionic environments, (2) description of the electrostatics and effect of geometry on titration curves and the degree of ionization at varyng ionic strengths, and (3) comparison of the charge of assemblies calculated with the electrostatic model and that from a Zeta potential measurement. Finally, in the last section, we present the conclusions of the present work.

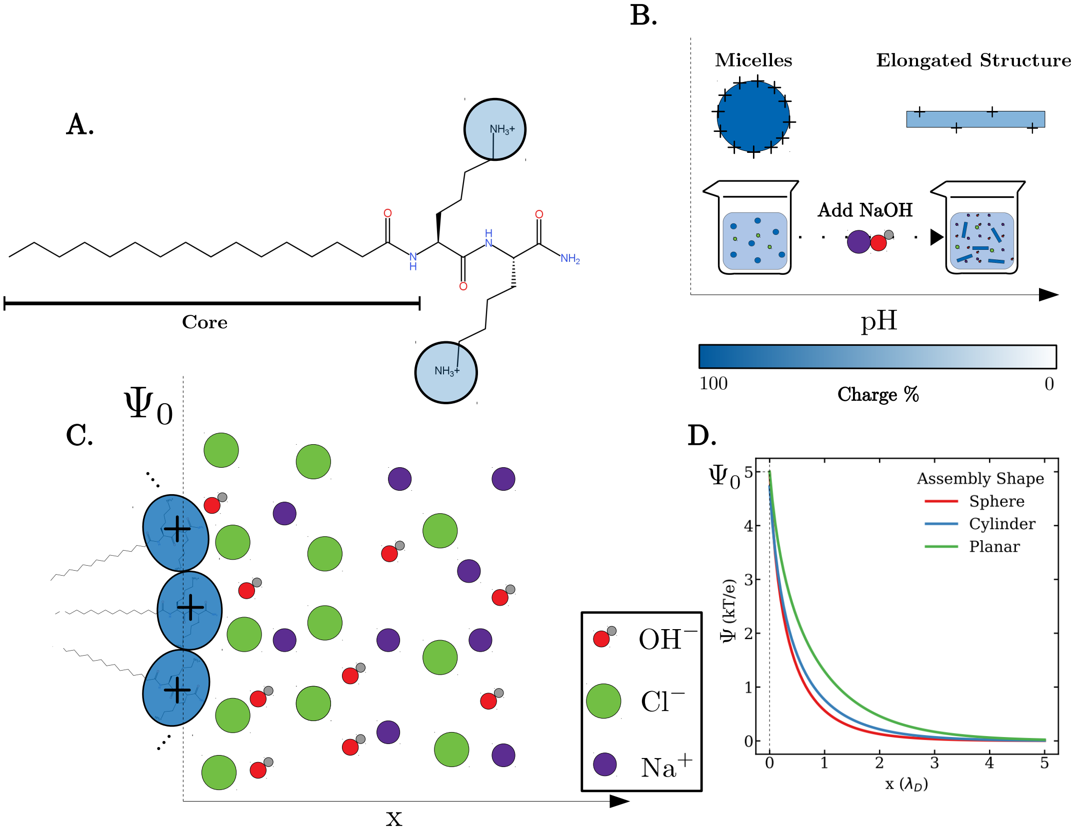

Figure 4.1: $C_{16}K_2$ assemblies and ionic environment A. Chemical structure $C_{16}K_2$ molecule. Highlighted in blue are the amine side chains whose ionization state changes with the ionic environment. **B.** Cartoon describing types of $C_{16}K_2$ assemblies formed in solution. The pH dictates the assembly morphology by changing the ionization state of the $C_{16}K_2$ molecules (decreasing charge with increasing pH). **C.** Close up view of B. and the ionic environment surrounding $C_{16}K_2$ assemblies. Ions consist of counterions ($\sim$ Cl^-) and added NaOH or NaCl (salt). Ψ_0 is the electrostatic potential at the surface of the assembly **D.** Electrostatic potentials (normalized by kT/e) for sphere, cylinder, and planar surface using approximate solutions to the 1D nonlinear PB equation for monovalent electrolytes (see A.4 for functional forms) [154]. $a \equiv \frac{R}{\lambda_D} = 0.5$, $\Psi_0 = 5 \simeq 125$ mV for the plots shown. A more closely packed assembly of charged molecules (e.g. planar) results in higher electrostatic potential.

Table 4.1: Titration models

Name	Assumption	Parameters	α, Degree of Ionization
HH	Dilute solution: no interaction between ionizable sites	pK$_{a,\text{ eff}}$	$\alpha = \frac{1}{10^{\text{pH}-\text{pK}_{a,\text{ eff}}}+1}$
Hill	(Anti-) Cooperativity between sites: implicit interactions between sites based on Hill coefficient $m > 1$ ($m < 1$)	pK$_{a,\text{ eff}}$; m	$\alpha = \frac{1}{10^{m(\text{pH}-\text{pK}_{a,\text{ eff}})}+1}$
Electrostatic	Electrostatic interaction between sites and ions: explicit Poisson Boltzmann electrostatic potential of ionizable surface, ψ_0, and fixed pK$_a$=pK$_{a,isolated}$	—	$\alpha = \frac{1}{10^{\text{pH}-\text{pK}_a}e^{-\beta e\psi_0}+1}$

4.2 Method Specifications

4.2.1 X-ray Scattering

SAXS/WAXS intensities (0.02 nm^{-1} < q < 15 nm^{-1}) were collected simultaneously using three Rayonix CCD detectors at the 5 ID-D undulator beamline of the Advanced Photon Source (APS) at Argonne National Laboratory. The beam size was 0.25 × 0.25mm^2, and the incident beam intensity was 3×10^{11} photons/s at 17 keV. The sample solutions were injected through a capillary tube flow-cell (1.5 mm, quartz) at 2-5 mm/sec to reduce radiation damage. The capillary was embedded in a vacuum cell to avoid air scattering. A fast shutter was used to limit sample exposure to X-rays only during the data collection time (5-10 s for each measurement). For improving statistics, 10 measurements were made per sample. For background subtraction and for calibrating the intensities to an absolute scale, SAXS/WAXS patterns were also collected from the empty capillary and from the capillary containing pure water before measurements on every sample. Additional SAXS/WAXS measurements were performed at 12 ID-C,D. At this APS beamline, data was collected using a Pilatus single photon counting area detector placed at a sample to detector distance (SDD) of 2.27 m. 18 keV X-ray were used. The beamsize at the sample position was $\sim$ 0.4mm $\times$ 0.2mm and the flux was 2×10^{12} photons/s. An exposure time of $\sim$ 1 s was used.

The 2D SAXS/WAXS patterns were converted into 1D intensity profiles by azimuthal integration while taking into account the polarization, solid-angle and transmission corrections. The data were also normalized for the scan time. For absolute intensity calibration, the normalized and corrected scattered intensity profiles from pure water (difference of the scattering from capillary filled with water and the empty capillary) were fitted to straight lines. The intercept of these lines was set to 0.0165 cm^{-1}, the expected scattered intensity from water at $q = 0$ on an absolute scale at $T = 25°$C. The data from the corresponding samples were thereafter scaled accordingly.

4.2.2 Titration

5-8 mL solutions of 4 mM $C_{16}K_2$ were titrated with a 0.1 M NaOH solution. The amphiphile, NaOH, and NaCl solutions were freshly prepared in ultrapure water (resistivity = 18.2 $M\Omega$·cm). The pH was measured using an Oakton pH 6 Acorn Series meter equipped with a Mettler Toledo micro electrode, which was calibrated at pH 4, 7 and 10 using buffers, prior to titration measurements.

4.2.3 Zeta (ζ) Potential

Zeta potential measurements were performed on 4 mM $C_{16}K_2$ solution in NaCl concentrations ranging from 0-250 mM. The amphiphile, NaOH, and NaCl solutions were again freshly prepared in ultrapure water (resistivity = 18.2 $M\Omega$·cm) The Zeta potential (and conductivity) was measured using a Zetasizer Nano ZS instrument with Zetasizer Nano Series disposable folded capillary cells (DTS1070) in the NUANCE facility at Nortwestern University. Cells were filled using syringes slip fitted to the cell openings to prevent bubble formation. Electrophoretic Light Scattering (ELS) is used to measure the electrophoretic mobility of particles in dispersion, or molecules in solution. This mobility is converted to a Zeta potential.

4.2.4 Electrostatic Model for Titration

The molecular charge of a $C_{16}K_2$ individual ionizable site is expected to decrease with increasing pH according to (4.1).

$$\mathrm{p}K_a = \mathrm{pH} - \log_{10} \frac{[\mathrm{NH_2}]}{[\mathrm{NH_3^+}]} \tag{4.1}$$

K_a is the reaction coefficient (i.e. dissociation constant) of an isolated lysine ($\mathrm{p}K_{a,\text{lysine}}$ = $\mathrm{p}K_{a,\text{isolated}}$=10.5). All lysines are treated equivalently in the modelling of $C_{16}K_2$.

We work in the continuum approximation of the PB formalism for electrostatics. This follows from Ninham-Parsegian model for CR where the density of ion-exchanging molecules (e.g. OH^-) follows a Boltzmann distribution with respect to the electrostatic potential of the ionizable surface ($\rho_{surface} \sim \rho_{bulk} e^{-\beta e \psi_0}$), where $\beta = \frac{1}{k_B T}$ (k_B is the Boltzmann constant, T is temperature), e is the elementary charge, and ψ_0 is the electrostatic potential at the surface [134]. The 1D nonlinear PB equation for monovalent electrolytes is

$$\frac{d^2\Psi}{dx^2} = \sinh \Psi \tag{4.2}$$

where $\Psi = e\psi / k_B T$ is the normalized electrostatic potential and the coordinate x is normalized by the Debye length $\kappa^{-1} = \lambda_D$. Equation (4.2) has approximate analytical solutions for the spherical, cylindrical, and planar geometries [154]. Example plots of the solutions are shown in 4.1D. A.4 contains the full functional forms for a sphere ($\Psi_S(x, a, \Psi_0)$), cylinder ($\Psi_C(x, a, \Psi_0)$) and planar ($\Psi_P(x, \Psi_0)$), where $a = \frac{R}{\lambda_D}$. We describe our ionizable surface with a charge density $\sigma = \frac{\alpha e}{S}$, where S is the area per ionizable group ($= \frac{1}{2} \times$ area per lipid, due to the 2 ionizable amine side chains of the lysines in the head group of $C_{16}K_2$) and $\alpha \equiv \frac{[\mathrm{NH_3^+}]}{[\mathrm{NH_3^+}]+[\mathrm{NH_2}]}$ is the degree of ionization. To account for CR effects, we impose the CR boundary condition.

$$\left.\frac{d\Psi}{dx}\right|_{x=x_0} = \frac{4\pi l_B \alpha}{S} \tag{4.3}$$

$$\alpha = \frac{1}{1 + 10^{\mathrm{pH} - \mathrm{p}K_a} \exp^{-\Psi_0}} \tag{4.4}$$

where $x = x_0$ is located at the ionizable surface, $l_B = \frac{e^2}{4\pi\epsilon_0\epsilon_w k_B T}$ is the Bjerrum length, and pK_a is the dissociation constant of the isolated ionization site. Equation (4.3) is Gauss's law for an arbitrary surface of charge density σ. The boundary condition of (4.3) is valid if the electric field does not penetrate the hydrophobic core of the $C_{16}K_2$ assemblies, which is true here since the dielectric constant of the hydrocarbons is much less than the dielectric constant of water ($\epsilon_{core}/\epsilon_w \simeq 2/80$). (4.4) is the electrostatic model for the degree of ionization α. These two equations are solved for self-consistently to acquire α and Ψ_0. From there, we back-calculate titration curves by relating α (or Ψ_0) to experimental parameters like concentration (e.g. pH$= -\log_{10}([H^+])$ by using equation (4.4) (see B.2). In this way, we characterize the ionizable assembly surface in terms of the electrostatic potential of the surface that arises from the geometry and the number density of ionizable sites each with dissociation constant pK_a. The electrostatics is now explicitly incorporated into the resulting degree of ionization behavior as opposed to phenomenologically accounted for with a p$K_{a,\text{eff}}$.

Inputted into the model is the pK_a for an isolated ionizable site (pK_a = p$K_{a,\text{lysine}} = 10.5$),[85] the ionic strength ([NaCl]+2[$C_{16}K_2$]), the appropriate functional form of the electrostatic potential for a given geometry, and nano-scale structural information about $C_{16}K_2$ assemblies extracted from SAXS/WAXS profiles. For example, the aggregation number of a micelle (sphere) determines how many ionizable sites are included which is directly related to the area per ionizable site, $S_{mic} = \frac{4\pi R^2}{2N_{agg}} = \frac{3N_{e,core}}{2R\rho_{core}}$, where $N_{e,core}$ is the number of electrons in a single C_{16} hydrocarbon tail and ρ_{core} is the electron density of the hydrocarbon core region. Similarly, the area per ionizable site of a cylindrical micelle (cylinder) is $S_{cyl} = \frac{N_{e,core}}{R\rho_{core}}$ and of a bilayer (planar) structure is $S_{bil} = \frac{2N_{e,core}}{t\rho_{core}}$, where t is the thickness of the hydrophobic region of the bilayer.

We emphasize here that within this model, pK_a is a fixed value based on the ionizable site behavior when it is in dilute solution. Shifts from pK_a to p$K_{a,\text{ eff}}$ are no longer necessary as all interaction behavior (or cooperativity) is explicitly accounted for in Ψ_0. And there are no adjustable parameters as the structural information that determines the electrostatic potential of the assemblies is acquired via SAXS.

4.3 Results and Discussion

4.3.1 Characterization of $C_{16}K_2$ assemblies in varying ionic strength

The structures of $C_{16}K_2$ assemblies in varying ionic strength ([NaCl]+2[$C_{16}K_2$]) were analyzed over a micro- to nano-meter length-scales by in-situ small- and wide-angle X-ray scattering (SAXS/WAXS). $C_{16}K_2$ assemblies, in the absence of added NaCl, were analyzed in a similar manner in previous work [14]. Structures formed by 4mM solutions of $C_{16}K_2$ in aqueous solutions varying from 0-800 mM NaCl and pH 4-11 were analyzed. The background substracted SAXS/WAXS intensities are measured as a function of scattering vector $q = 4\pi \sin\theta/\lambda$ where λ is the X-ray wavelength and 2θ is the scattering angle.

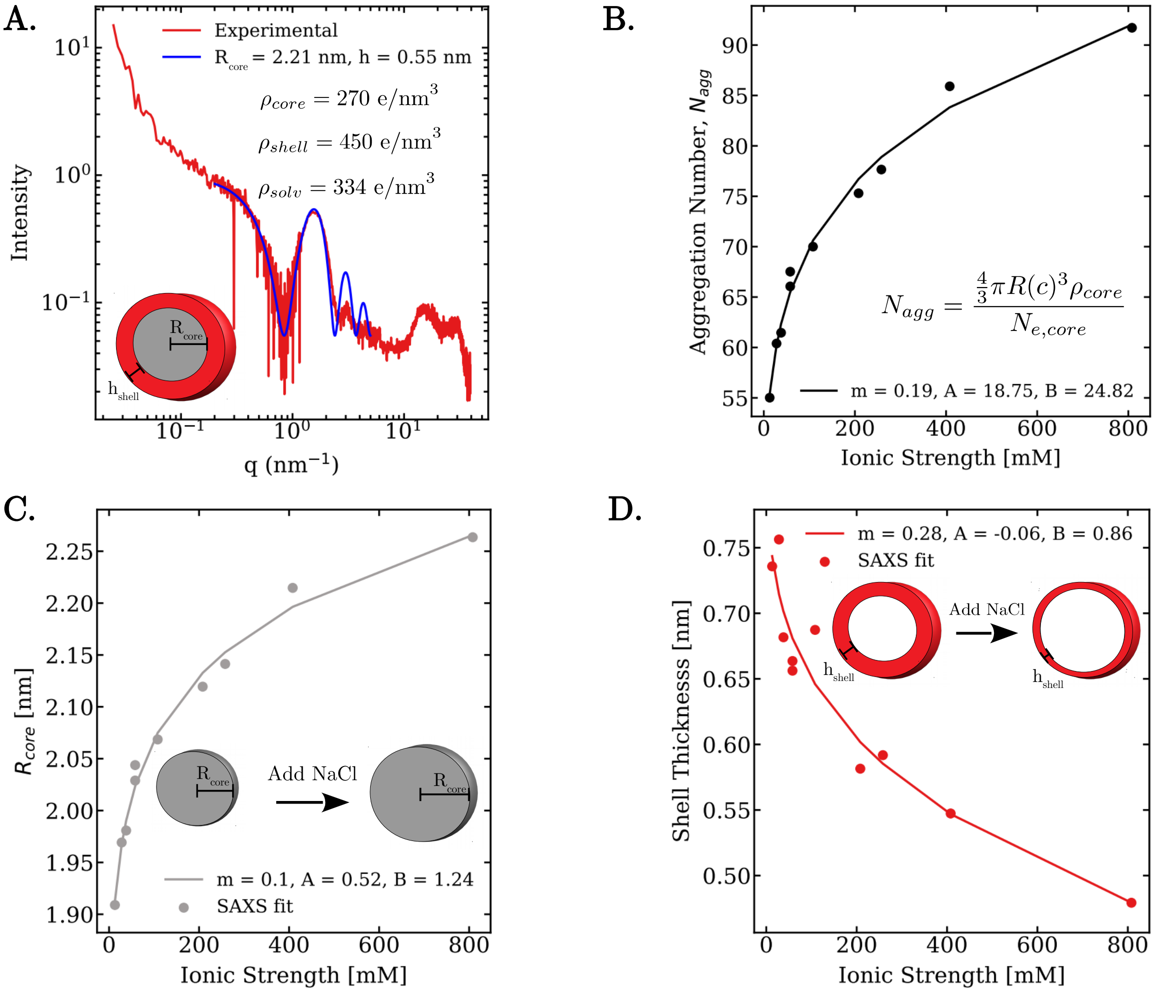

Figure 4.2: Micelle characterization A. SAXS pattern (red) and corresponding core-shell form factor fit (blue) for $C_{16}K_2$ in 400mM NaCl. Radius and shell thickness for $C_{16}K_2$ assemblies in different salt concentrations were all extracted with this method. **For B.,C.,D.**: Points are experimental results based on form factor fit. Lines are a power law trend $f(c) = Ac^m + B$, where A,B, m are paremeters and c is ionic strength. **B.** Aggregation number per core-shell (micelle) aggregate as a function of ionic strength using equation shown in plot ($N_{e,core} = 143$ is number of electrons in an individual molecular core component) **C.** Data and power law fits as a function of salt concentration for observed trend in core radius and **D.** shell thickness. Cartoons in inset of C. and D. describe the increasing core radius and decreasing of shell thickness for fixed core, shell, and solvent electron densities. The structural parameters and power laws from SAXS analysis of C16K2 micelles are used for the electrostatic modelling of titration and degree of ionization.

4.3.1.1 $C_{16}K_2$ micelles with added salt

For low pH (pH$<=6$), when the PA headgroups are expected to be more charged on average as compared to higher pH levels, the SAXS intensity profiles could be fitted by spherical core-shell form factor models at all NaCl concentrations up to 800mM (4.2A). For the fitting of SAXS profiles, the electron density of the core (assumed to comprise of hydrophobic tails) was constrained to be $\rho_{\text{core}} = 270e/\text{nm}^3$. This assumption is around 80% of that for pure water ($\rho_w = 334e/\text{nm}^3$) and is consistent with a noncrystalline, fluid-like packing of alkyl tails as to be expected for micelle assemblies [155]. Fitting parameters are the spherical core radius (R_{core}) and shell thickness (h), as well as a scale factor and a uniform background. R_{core} increases from 1.90 to 2.28 nm while h decreases from 0.86 nm to 0.48 nm (4.2C,D). Power law fits to the trends in R_{core} and h are also shown.

The increasing core radius with increasing NaCl can be explained in terms of nearest neighbor electrostatic interactions. As the salt concentration increases, the range of the electrostatic interactions decreases. This permits more closely packed $C_{16}K_2$ molecules. A manifestation of this proposition is the simultaneous increase in the aggregation number of the micelles (4.2B). $N_{e,\,core} = 143$ is defined as the number of electrons in atoms of the alkyl tails included up to but not including the α-carbon of the first lysine in the head group (4.1C). In both cases, the increasing trend seems to level off at the highest salt concentrations, assumed to be where the alkyl tails are at their critical (maximum) chain length. A critical chain length of hydrocarbon tail consisting of 16 carbons can be estimated at 2.18 nm by the Tanford equation [156]. The higher plateau at around 2.28 nm in our measurements comes from the inclusion of additional atoms up to the first α-carbon of $C_{16}K_2$ in the definition of of R_{core}.

Conversely, the shell thickness decreases with increasing salt concentration. The shell constituents are not only the charged lysine head groups, but also water and any other ions near the surface of the micelle. Condensed layers of ions near the surface are to be expected for charged colloidal assemblies. For this reason, the assumption of a constant electron density for the shell ($\rho_{shell} = 450e/\text{nm}^3$) leads to conclusions about not only the head groups, but also the solution environment around the charged micelles. We now note here that the decreasing shell thickness is consistent with the compression of the electrical double layer for increasing salt in colloidal assemblies that is seen for other charged assembly systems [157, 158]. We will use this finding to compare surface charge density calculation methods of $C_{16}K_2$ micelles in section 4.3. With the assumptions of constant electron densities, overall radius ($R_{\text{core}} + h$) varies between 2.65 and 2.77 nm and does not follow an monotonic increasing or decreasing trend (Figure 4.3).

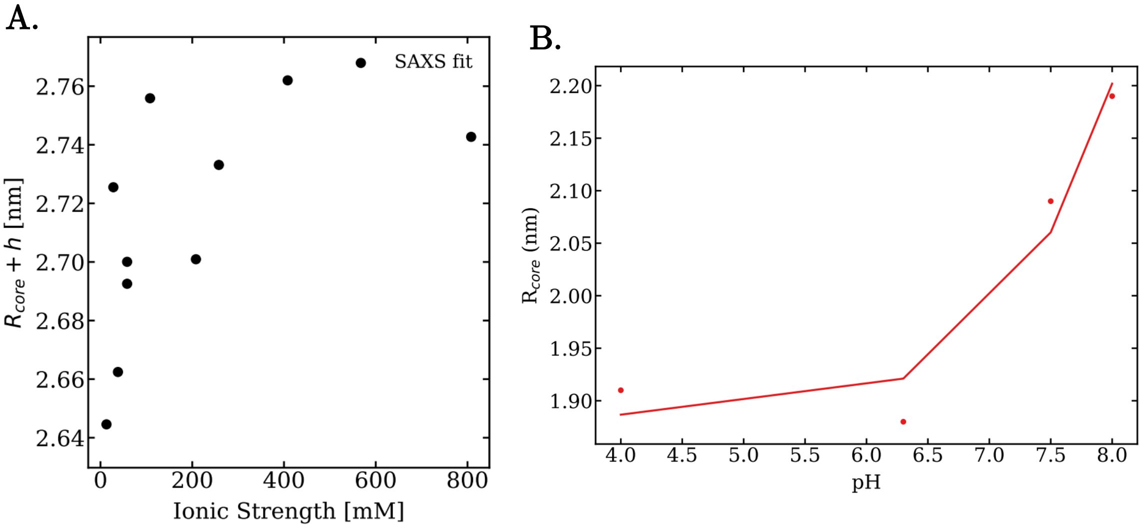

Figure 4.3: **A.** The total radius ($R_{core} + h$) increases non-monotonically with increasing salt concentration. **B.** The radius of $C_{16}K_2$ micelles remains relatively constant up to the transformation from micelle to cylindrical micelle transition point (pH∼7.5).

4.3.1.2 $C_{16}K_2$ shape transitions as a function of pH in 5mM NaCl (low ionic strength) and 250mM NaCl (high ionic strength)

As pH is tuned the ionization state of the lysine head groups in $C_{16}K_2$ will change due to the changing concentration of OH^-. This, in turn, triggers certain assembly transitions. We have seen that increasing the concentration of NaCl alone does not result in a transition of overall geometry (4.2). Reducing the range of electrostatic interactions is insufficient to trigger morphological transitions for $C_{16}K_2$ assemblies. For $C_{16}K_2$ in 5mM added NaCl, as the pH is increased, there is a transition

Table 4.2: Volume fractions used in form factor fits (4.4) and combined titration curve (4.4A)

pH	Isolated	Micelle (Sphere)	Cylindrical Micelle (Cylinder)	Bilayer (Planar)
6.3	0.76	0.24	0	0
7.5	0.52	0.48	0	0
8.0	0	1.0	0	0
8.1	0	0	1.0	0
8.4	0	0	0.20	0.80
8.9	0	0	0	1.0
9.8	0	0	0	1.0

from small unidentified structures or monomers to micelles to cylindrical micelles to planar bilayer/lamellar stacks. 4.4B shows the SAXS intensity profiles along with form factor fits for $C_{16}K_2$ in 5mM NaCl for pH = 4.0, 6.3, 7.5, 8.0, 8.1, 8.4, 8.9, and 9.8 from which this transitional pathway was extracted. For $0.08 < q < 0.3$nm^{-1} , within the low q regime, the I vs q slope becomes steeper for increasing pH. These changes in the slope are related to the changes in the overall morphology of the assembly. The slope from best fit lines (black lines, 4.4B) for the SAXS region of well defined assemblies for increasing pH are -0.47 to -0.52 to -1.45 to -2.03 to -2.05 to -2.48. Such slope changes are highlighted in 4.4B. The increasing magnitude of the slope with increasing pH are related to the changes in the overall morphology of the assembly. Larger magnitudes correlate to higher dimensional structures: from point-like (0D) micelles to 1D rod like elongated structures to 2D planar surfaces. The pH value at which the transition from micelle to cylindrical micelle occurs is around pH$= 8.1$. This is around the p$K_{a,\text{eff}}$ value shown in 4.4A as to be discussed in a later section. At higher pH (>=8.9, low degree of ionization), a pronounced diffraction peak appears $q_p = 5.45$ nm^{-1}. This corresponds to a length $\frac{2\pi}{q_p} = 1.15$ nm. This value is consistent with proposed lattice structure for $C_{16}K_2$ bilayers in previous work [14]. Due to this, we attribute the peak to membrane crystallization behavior when the degree of ionization is very low.

Form factor models were used to fit the scattering patterns from 0.1 nm$^{-1} < q < 10$ nm^{-1} (grey lines, 4.4B). For pH 4.0, 6.3, 7.5, 8.0, 8.1, and 8.9, fits employed a single form factor of core-shell, cylindrical core-shell, or a symmetric three-slab model to represent micelle, cylindrical micelle, or bilayer structure respectively. Electron densities were held fixed for all form factor model fits with $\rho_{solv} = 334e/\text{nm}^3$, $\rho_{shell} = \rho_{outer\ slabs} = 450e/\text{nm}^3$, and $\rho_{core} = \rho_{core\ slab} = 270e/\text{nm}^3$. For pH 4.0, 6.3, 7.5, and 8.0, the scattering patterns are fit well with a core-shell form factor with $R_{\text{core}} = 1.91$, 1.88, 2.09, and 2.19 nm and $h = 0.74$, 0.78, 0.75, and 0.71 nm, respectively. At lower pH, the core radius of C_{16}K_2 remains relatively constant. As the pH approaches the transition point from micelle to cylindrical micelle (pH 8.0-8.1), the core radius of C_{16}K_2 micelles begins to increase. For pH 8.1, the scattering pattern is fit well with a cylindrical core-shell form factor with $R_{\text{c, core}} = 1.54$ nm and $h_c = 0.90$ nm. The transition from micelle to cylindrical micelle can now be envisioned as a smaller micelle becoming as large as sterically possible up to some $R_{\text{core}} = R_{\text{critical}}$ before it changes to cylindrical morphology and adopts a more compact structure once again. From a critical packing parameter (CPP) perspective, the relationship between the micelle chain length and cylindrical micelle chain length at the transition should be around $\frac{1/3}{1/2} = \frac{2}{3}$. For C_{16}K_2, we find $\frac{R_{c,core}}{R_{critical}} = 0.70 \simeq \frac{2}{3}$, supporting this morphology transformation characterization. In addition, the scale factors associated to the micelle fits increase monotonically from pH 4.0 to pH 8.0. At pH 8.0, we expect there to be only micelles and minimal amounts of isolated molecules in solution. By comparing the magnitudes of the form factor fit scale factors relative to pH 8.0, we can approximate the volume fraction of C_{16}K_2 molecules that are assembled into micelles and those that are isolated in solution. The volume fraction values are tabulated in Table 4.2.

At pH 8.9, a symmetric three-slab model of $t_{\text{core}} = 3.45$ nm and $h_b = 1.35$ nm fits the scattering pattern. For pH 8.4, a weighted sum of the pH 8.1 and pH 8.9 fits are used to reproduce the scattering pattern. In this way, we can capture the volume fraction of each structure as the C_{16}K_2 undergo a shape transformation from cylindrical micelle to bilayer (Table 4.2). At very high pH=9.8, a simple three-slab form factor model is unable to reproduce the scattering pattern. However, due to large slope in the SAXS regime (-2.48), we deduce C_{16}K_2 is forming aggregations of planar-like assemblies. The closeness of molecular packing for each of the above reported assemblies proceeds as isolated molecules/small clusters < micelle < cylindrical micelle < bilayer. Therefore, we can immediately see that with an increase in pH, as the lysine head groups prefer to be in there uncharged deprotonated state, the closer pack assemblies are more favorable by attractive van der

Waals interactions in the hydrocarbon tails. In other words, the magnitude of electrostatic repulsion between the head groups is reduced, permitting the molecules to pack more closely together in an energetically favorable configuration.

A similar shape transition pathway is observed for $C_{16}K_2$ in 250mM NaCl (4.7B). Owing to the decreased range of electrostatic interactions, $C_{16}K_2$ molecules in 250mM NaCl immediately form into well-defined micelles when put in aqueous solution without changing the pH. As the pH is increased, the assemblies become cylindrical micelles and then planar bilayer stacks with low q slope changes from -0.71 to -0.80 to -1.86 to -2.68, in a similar manner as 5mM NaCl. Form factor core shell fits for micelles with the same electron density as used for [NaCl]=5mM are $R_{core} = 2.14$nm, $h = 0.59$nm for pH 6.0 and $R_{core} = 2.22$nm, $h = 0.57$nm for pH 8.5. Similarly, $R_{c,core} = 1.64$nm and $h_c = 1.0$nm for cylindrical core-shell (cylindrical micelle) at pH 9.3. Therefore, we believe this shape transition of $C_{16}K_2$ to be general for any ionic strength. The difference between 5mM and 250mM NaCl structural transition pathways is the pH value of the transitions, which shifts to higher values for 250mM NaCl (4.7B). The micelle to cylindrical micelle transition occurs around pH 9 and cylindrical micelle to bilayer around pH 9.5. As stated earlier, transitions are typically found near the buffer region, pH=p$K_{a,\text{eff}}$ and the p$K_{a,\text{eff}}$ of $C_{16}K_2$ in 250mM NaCl is around 8.8. The location of the buffer region increases with increasing salt concentration: p$K_{a,\text{eff, 5mM}}$<p$K_{a,\text{eff, 50mM}}$<p$K_{a,\text{eff, 250mM}}$<p$K_{a,\text{eff, 500mM}}$ (4.7A). This finding is consistent with the idea that ionization behavior should tend towards free lysine behavior (p$K_{a,\text{lysine}} = 10.5$) for decreased range of electrostatic interactions. As the salt concentration is increased, the ionization sites behave more like isolated lysine sites as they are electrostatically screened from their neighbors. Finally, the increased relative intensity of the high $q_p = 5.45$ nm^{-1} peak for 250 mM NaCl compared to 5 mM NaCl suggests that the lamellar crystallization at high pH is more pronounced with higher NaCl concentration.

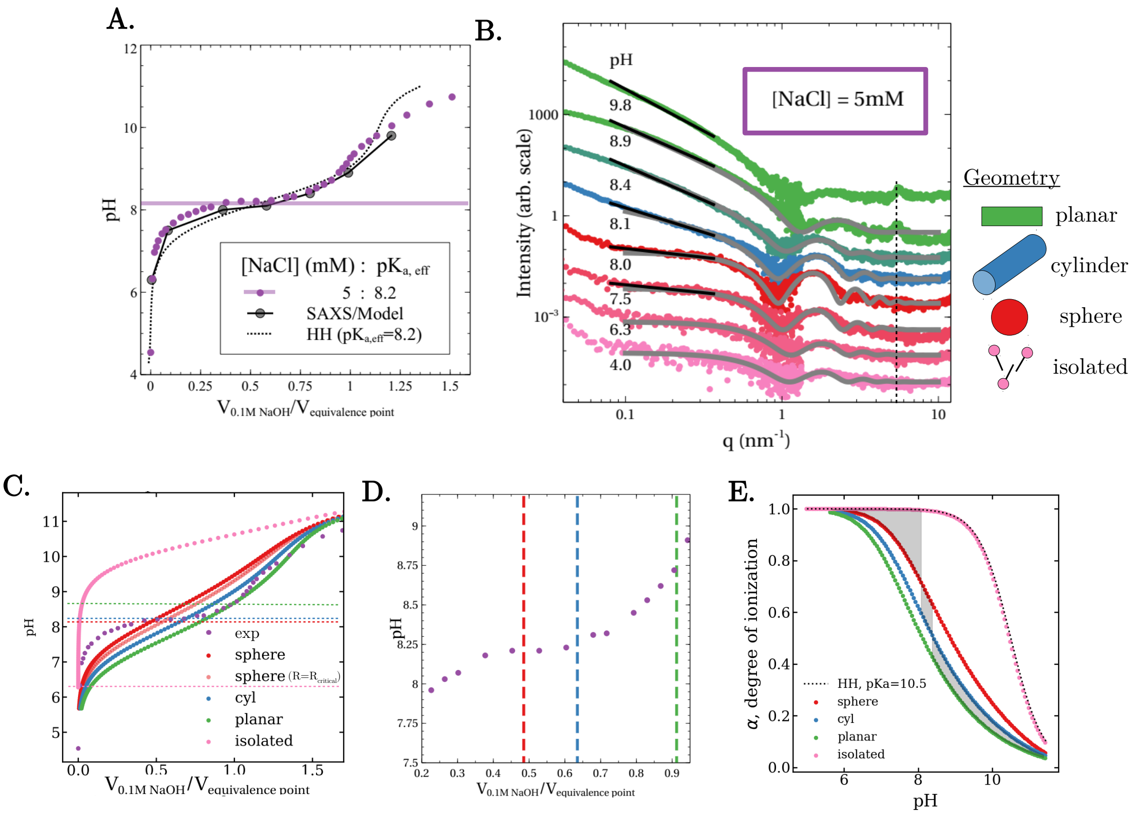

Figure 4.4: Shape and size dependent titration and degree of ionization **A.** Titration experimental data for $\mathrm{C}_{16}\mathrm{K}_2$ in 5 NaCl. Approximate p$K_{a,\text{ eff}}$ are given by a straight line fit to the flat buffer region in titration curves. Black points and line correspond to the reproduced titration curve by combining structural information from SAXS and the electrostatic model for titration. Also shown is the HH model with p$K_{a,\text{ eff}} = 8.2$ for comparison. **B.** SAXS patterns for $\mathrm{C}_{16}\mathrm{K}_2$in 5mM with increasing pH. The assembly transition pathway with increasing pH (decreasing degree of ionization) is unidentifiable small assemblies (pink) to micelle (red) to cylindrical micelle (blue), to bilayer/planar lamella (green). Coexistences of multiple types of assemblies are represented by a color gradient between the transition pathway structures. For example, at pH 8.4 there is coexistence of cylindrical miclles and bilayers (blueish green). Best fit lines for the low q region (black) characterizing these structures increase with increasing pH (-0.47 to -0.52 to -1.45 to -2.03 to -2.05 to -2.48). Locations for transition from micelle to cylindrical micelle are slightly above the p$K_{a,\text{eff}}$ values shown in **A.**, within the buffer region. A diffraction peak at $q_p = 5.45$ nm^{-1} is identified (black dotted). **C.** Titration curve with corresponding electrostatic model of titration for 5mM NaCl. Shown are the back calculated titration curves for sphere, sphere (at $R = R_{critical}$), cylinder, planar, and isolated (HH) assembly. Intersection of experimental titration curves with different electrostatic model shapes are close to the experimentally measured transitions. Flat buffer regions can be explained by these transitions of assembly shapes. **D.** To the right is a zoom in of the buffer region which shows at what fractional equivalence volume of added titrant the models intersect the titration curve. **E.** The degree of ionization (and comparison to bulk lysine) is shown. A purposed shape-dependent degree of ionization is overlayed with a black shading, where the degree of ionization lies somewhere within the shaded region based on the structures observed with SAXS.

4.3.2 Effect of geometry on titration curves and degree of ionization

4.3.2.1 Low ionic strength

To quantitatively relate pH and the degree of ionization, we titrated 4 mM $C_{16}K_2$ solution in pure water with 0.1 M NaOH solution. 4.4A shows the measured titration curve for $C_{16}K_2$ in 5 mM NaCl. This correspond to Debye screening length $\lambda_D = \frac{0.3\text{[nm]}}{\sqrt{\text{ionic strength [M]}}}$= 2.63 nm where ionic strength is defined as the concentration of NaCl plus the concentration of counter-ions ($2 \times$ [$C_{16}K_2$]=8 mM). The titration curves are plotted as a function of the fractional equivalence volume, defined as the total added volume of 0.1 M NaOH solution divided by the volume of the equivalence point ($V_{0.1M\ \text{NaOH}}/V_{\text{equivalence point}}$). The equivalence point volume is defined as the volume of added NaOH at which the derivative of the pH with respect to volume of added NaOH is maximum (inflection point). Thereafter this point, the added NaOH is assumed to only increase the solution pH. Using the fractional equivalence volume permits a general comparison between titration experiments independent of total volume. The overall goal is to reproduce experimental titration curves in while taking into account the morphological transitions by modelling the electrostatic potential for the given assembly surface geometry as can be seen in 4.4A.

A region of interest within titration curves is the buffer region, characterized by a flat plateau. This is where the majority of ion exchange from the solvent and assembly head groups is expected to occur. Buffer regions are typically located around HH or Hill fitted p$K_{a,\text{eff}}$ values. For $C_{16}K_2$ in 5 mM added NaCl, we measured a buffer region at pH~ 8.2. This is around the location of SAXS inferred morphological transitions for the assemblies in the same ionic conditions. In general, assembly transitions commonly occur within the buffer region of the titration curve, such as the micelle to vesicle transition in fatty acids which frequently occur at pH $\sim$ p$K_{a,\text{eff}}$ [159]. The flat appearance of the buffer region is interconnected with the interchanging between different assembly morphologies. This can be seen in 4.4C with the reproduction of titration curves for various geometries from the electrostatic model and their comparison to the experimentally measured titrations of $C_{16}K_2$ in 5mM NaCl. In the electrostatic model, the micelle morphology is approximated in the continuum by a sphere (radius equal to R_{core}). Since the micelle radius remains relatively constant as we increase pH up to the transition point, we use the micelle radius in [NaCl]=5 mM at unchanged pH ($R = R_{core} = 1.91$ nm) in the reproduction of titration curves with the electrostatic model. A reproduction of the titration curve for a sphere at the critical radius ($R = R_{critical}$) is also shown in 4.4C to show the effect of a $\sim$ 0.3 nm increase in radius. Similarly, the cylindrical micelle is approximated with an (infinite) cylinder and planar bilayer with an (infinite) plane, all within the nonlinear PB formalism.

The electrostatic model curves intersect the experimental titration curve at pH values corresponding to approximate locations of assembly morphology transitions. The pH location of the intersection of the sphere (red dashed) and cylinder (blue dashed) are very close to one another within the buffer region. 4.4D zooms in on this region and highlights where the electrostatic models intersect the titration curve. The difference in the intersection pH (y-axis) between the sphere and cylinder is minimal, but there is a noticeable difference in the fractional equivalence volume (x-axis). This makes the fractional equivalence volume a useful parameter when predicting the location of morphological transition. By taking appropriate volume fractions of the different structures deduced from SAXS (4.4B) and applying those volume fraction weights to the reproduced titration curves for the different geometries (4.4C), we can reproduce a $C_{16}K_2$ titration curve without any adjustable parameters. Table 4.2 contains volume fraction information used to generate black points in 4.4A. Discrepancies between the titration model and titration curve in the buffer regiong may be attributed to titration curves varying slightly between synthetic batches of $C_{16}K_2$. These differences could be due to variations in the concentration of the amphiphile or of residual salts after purification and lyophilization. In addition, at low degree of ionization (high pH), we observed crystallization behavior in $C_{16}K_2$ planar assemblies. In this region, we do not expect PB electrostatic interactions to be the dominating factor in determining the ionization behavior of the system, but rather short range correlations that determine the crystal structure. Therefore, at high reduced equivalence volume, we see deviations between the model and experiment.

Titration curves are typically measured for the purpose of quantifying the degree of ionization (i.e. charge fraction). For $C_{16}K_2$, the assembly geometry can have a dramatic effect on the degree of ionization for 5mM NaCl (4.4E). For example, at pH=8, isolated (HH) lysine sites have a degree of ionization of $\alpha = 1.0$, corresponding to all lysine amine side chains being in their charged, protonated state. However, for lysines assembled in a spherical geometry at the same pH=8, $\alpha \simeq 0.75$. Similarly, for a cylinder, $\alpha \simeq 0.62$, and for a planar surface $\alpha \simeq 0.50$. The differences in the degree of ionization is due to the difference in electrostatic potential and structural details for these different types of geometries. On the basis of the electrostatic titration model and the reproduced tiration curve, the pH values for structural transitions and coexistence regions correspond to % ranges for the degree of ionization of the headgroup lysines (black shaded regions 4.4E). For mixtures of small unidentifiable structures or isolated monomers and micelles, the degree of ionization is $70 - 100$%. For micelles and cylindrical micelles, it is $45 - 70$%. And for cylindrical micelles and planar bilayer stacks, it is < 45%. This follows the intuition that more closely packed structures will be less charged, but now we can explicitly see where morphological transition occur and how those transitions affect the degree of ionization.

4.3.2.2 High ionic strength

4.7C shows an attempt, and failure, at reproducing the titration curve for $C_{16}K_2$ assemblies in 250mM NaCl using the equivalent method that led to success for 5mM NaCl. Further electrostatic considerations in the description of $C_{16}K_2$ assemblies illustrate reasons for the failure and remedies to the model. Within the PB framework, the electrostatic potential at the surface (and so-called bare charge density) increases indefinitely with increasing salt concentration. However, for large surface potentials and low screening lengths, the electrostatics away from the colloidal surface ($x \sim \lambda_D$) becomes completely insensitive to the surface potential and charge. Specifically, within the nonlinear-PB theory, the electrostatic potential that a nearby charged ion experiences due to a strongly charged colloidal assembly appears to plateau at a saturation effective potential values of $\Psi_0 \rightarrow \Psi_{eff}$ which is on the order of unity [160, 161]. Therefore, ionizing molecules near the surface will not be sensitive to the surface potential Ψ_0, but rather to an effective potential (and effective charge density) of the charged assembly [162]. The essential idea is that the surrounding ions, which suffer a high electrostatic coupling with the charged assembly, accumulate in its immediate vicinity such that the decorated assembly may be considered as a single entity which carries an effective charge, much lower (in absolute value) than the structural one. Therefore, to remedy the electrostatic modelling at higher ionic strengths and account for ions accumulating near the surface, we hypothesize a decorated assembly consisting of one monolayer of ions and consider the electrostatic potential at distance of one monolayer of ions above the charged surface ($r_{ion} = d_{ion}/2 = 0.18$ nm). The diameter $d_{ion} = 0.36$ nm is consistent with a traditional monovalent ionic diameter. Figure 4.7D-E shows the reproduction of titration curves for $C_{16}K_2$ assemblies in 50, 250, and 500 mM NaCl (corresponding to $d/\lambda_D = 0.29$, 0.61, and 0.86).

Modelling of the titration curves with Ψ_{eff} reproduces main features of the experimental titration curves for [NaCl] = 50, 250, and 500 mM in a manner similar to [NaCl]=5mM discussed in the previous section. For [NaCl] = 250mM, we use the SAXS fitted radii for the sphere (micelle) and cylinder (cylindrical micelle). Since the difference between the cylindrical micelle radius at 5mM (1.54 nm) and 250mM NaCl (1.64 nm) is relatively small, we approximate the size of 50mM and 500mM NaCl cylindrical micelles with these same values, respectively. The corresponding degree of ionization plots are shown in the Figure 4.5.

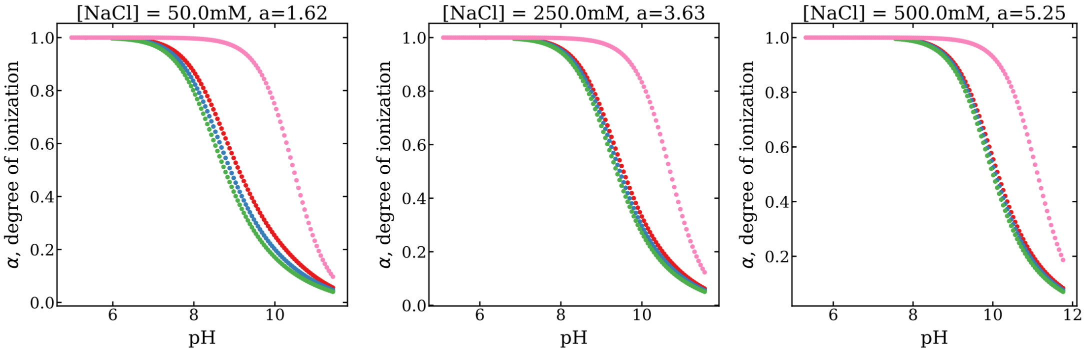

Figure 4.5: Degree of ionization for $C_{16}K_2$ assemblies as a function of pH for 50, 250, and 500mM added NaCl. The ionization behavior shifts towards bulk lysine behavior with increasing salt. In addition, the effects of assembly geometry become less important.

We note here that using Ψ_{eff} for [NaCl] = 5 mM results in some changes to the reproduced titration curves shown in 4.4C. However, the effect is less pronounced than at higher ionic strengths due to the increased screening length. We do not believe our Ψ_{eff} hypothesis should hold at

Table 4.3: Zeta potential with changing ionic strength

Ionic Strength [mM]	ζ[mV]	Conductivity [mS/m^2]
8	42.7	0.35
13	57.3	1.05
18	62.1	1.18
33	59.8	2.58
58	55.0	4.76
258	41.0	19.80

these lower ionic strengths for the same reason. Of particular importance, as the ionic strength is increased, differences in the reproduced titration curves for the different assembly geometries is greatly reduced as the curves essentially overlap at 500mM NaCl (4.7) While intuitive to understand, it leaves an absence in explaining the observed structural pathway for C$_{16}$K$_2$ assemblies. On the one hand, it would seem that assembly geometry effects should be less pronounced for increased screening between charged sites. However, the existence of consistently measured structural transitions suggest a persistent importance of geometry for C$_{16}$K$_2$ assemblies. We attribute this to a limitation of the nonlinear PB formalism and our approach to dealing with saturation potentials of C$_{16}$K$_2$ assemblies for different geometries. In addition, we note here that there interesting effects in the titration curves at higher ionic strengths. In particular,there are noticable humps in the titration behavior of C$_{16}$K$_2$ in both 250 and 500 mM NaCl, where further increasing the relative amount of NaOH led to anomalous decrease in pH (black arrows, 4.7A. It is unclear what is causing this phenomenon and we are unable to reproduce the effect with out model. Such a feature has been seen in previous titration of C$_{16}$K$_n$ systems [86]. The next section will further investigate the bare and effective charge densities of C$_{16}$K$_2$ assemblies to further test our modelling hypothesis.

4.3.3 Charge of micelle assemblies: A Zeta potential and PB Comparison

The electrostatic potential of a charged surface is directly related to the charge density of that surface. As stated in the previous section, at a particular point the charge density of a surface becomes independent of the surface potential when the system reaches a saturation point and an effective potential more appropriately describes the electrostatics (4.8A). A comparison of the bare electrostatic potential and the effective electrostatic potential used to fit the titration curves in the previous section is shown 4.8C. The bare electrostatic potential increases monotonically for all ionic strengths. The effective potential has a maximum value at an ionic strength around 23 mM (corresponding to $a = R/\lambda_D = 1$) and then proceeds to decrease due to the increased screening of the electrostatic potential at higher ionic strengths. It is at this point, the switch between bare and effective charge description seems necessary.

In general, within the electrostatic model of titration, the charge and electrostatic potential at a specific pH are related through equation (4.3), which due to the non-linearity of the PB equation, takes into account non-linear effects that become important near the surface of charged assemblies as the linearized (Debye-Huckel) version greatly overestimates Ψ in this region (4.8B). We can also indirectly measure the charge density of micellar assemblies by a Zeta potential measurement, which probes electrophoretic mobility of colloidal suspensions in an applied electric field. The Zeta potential is the electrostatic potential difference between the surround bulk solution and the slipping plane of the assembly. Table 4.3 shows the measured Zeta potential of $C_{16}K_2$ assemblies in different ionic strengths. Zeta potentials measured for $C_{16}K_2$ are similar to those found in previous studies of electrolyte concentration effects on ionizable assemblies [163, 164, 165].

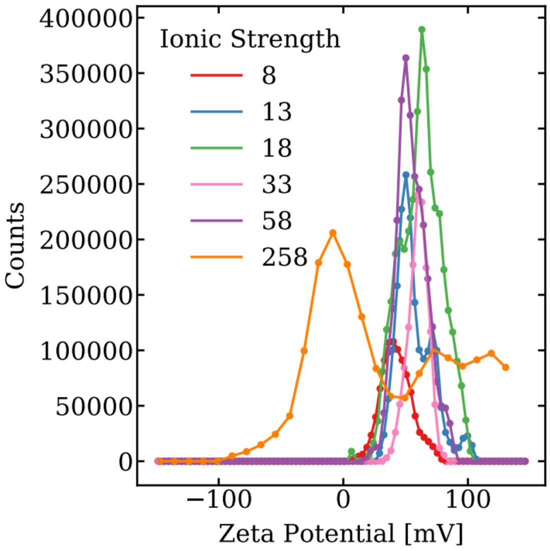

Figure 4.6: Zeta potential measurements for $C_{16}K_2$ micelle assemblies in different ionic strengths. 4.3 contain fit values for these measurements based on experimental apparatus software (see 4.2).

The conductivity, measured concurrently with the Zeta potential, are also consistent with the expectation that increasing the number of ions in solution should increase its ability to conduct electricity. We want to compare the charge density based on the electrostatic potential at the surface of the spherical assemblies calculated using equation (4.3) and the effective charge density with the charge density extracted from the Zeta potential measurements.

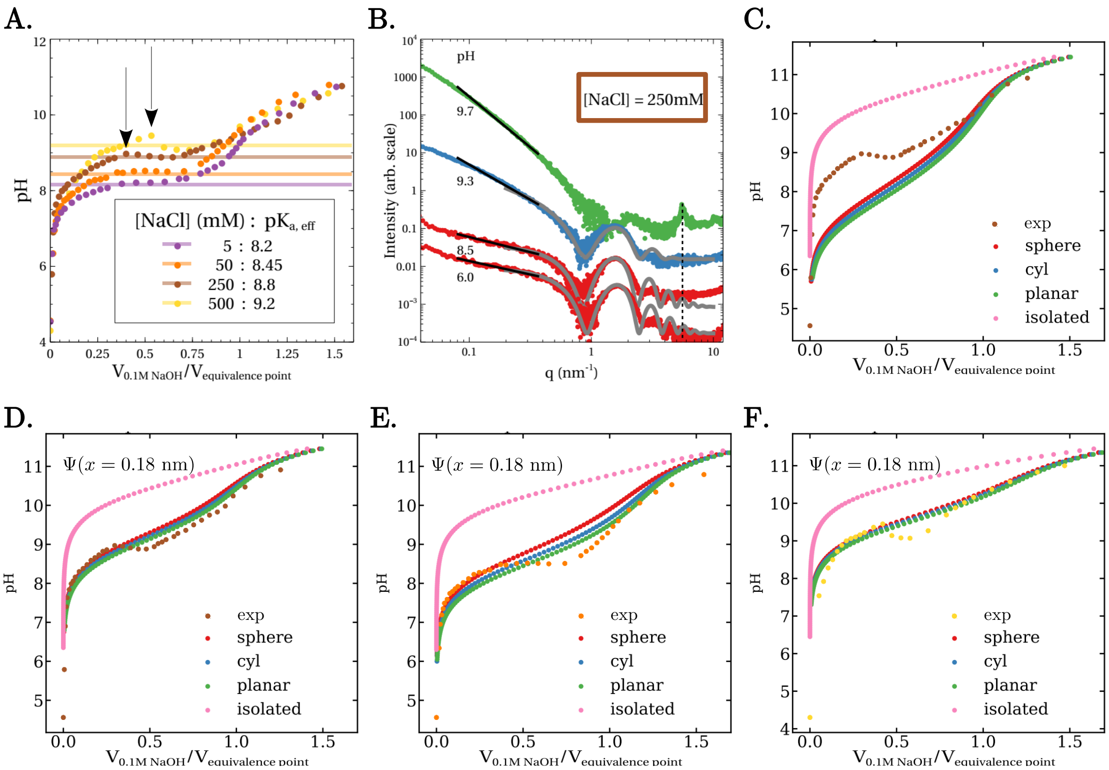

Figure 4.7: Titration curves at higher ionic strength A. Titration curves of $C_{16}K_2$ in 5, 50, 250, and 500 mM added NaCl. The p$K_{a,\text{ eff}}$ shifts upwards with increasing salt concentration towards bulk lysine behavior. Note, arrows are highlighting prominent bumps in titration curves at higher ionic strength. **B.** SAXS data for $C_{16}K_2$ assemblies in 250 mM NaCl at pH 6.0, 8.5, 9.3, 9.7. Best fit lines for the low q region for 250mM NaCl increase with increasing pH (-0.7 to -0.8 to -1.9 to -2.7) The transtions from micelle to cylindrical micelle and cylindrical micelle to bilayer shift to higher pH (in the same manner as p$K_{a,\text{ eff}}$. **C.** The electrostatic model based on the bare surface potential Ψ_0 is unable to reproduce titration behavior at 250 mM NaCl. Reproduced titration curves using the effective electrostatic potential $\Psi_0 \rightarrow \Psi_{eff} = \Psi(x = 0.18$ nm$)$ in 4.4 leads to better agreement for **D.** 250 mM ,**E.** 50 mM,**F.** and 500 mM

From the Zeta potential, we calculate the charge density of $C_{16}K_2$ assemblies by calculating the electrostatic potential at the surface using the Zeta potential as a constraint: namely, $\zeta \equiv \psi_S(h + x_{slip}, a, \psi_0)$. We take the slipping plane to be $x_{slip} = 0.24$ nm above the condensed layer of ions which is assumed to be equal to h (4.8B). h is the same shell thickness value measured from SAXS in 4.2D. This location of the slipping plane above the condensed layer of ions is consistent with previous results [157, 166, 167]. The resultant ψ_0 from this constraint, called $\psi_0(\zeta)$, is then used in the Grahame equation for curved surfaces to calculate the charge density (4.5) [162].

$$\sigma_{curved}(\psi_0(\zeta)) = \frac{2\epsilon\epsilon_0\kappa}{\beta e}\Big[\sinh\Big(\frac{\beta e\psi_0(\zeta)}{2}\Big) + \frac{2}{\kappa R}\tanh\Big(\frac{\beta e\psi_0(\zeta)}{4}\Big)\Big] \tag{4.5}$$

Similarly, for flat surfaces

$$\sigma_{flat}(\psi_0(\zeta)) = \frac{2\epsilon\epsilon_0\kappa}{\beta e}\sinh\Big(\frac{\beta e\psi_0(\zeta)}{2}\Big) \tag{4.6}$$

where ψ_P is now used instead of ψ_S for the functional form of the potential ($\zeta \equiv \psi_S = P(h + x_{slip}, a, \psi_0)$). A comparison between the curved (blue, equation 4.5) and flat (yellow, equation 4.6) Grahame equation calculation is shown in 4.8D to demonstrate the importance in considering geometric curvature effects when calculating the charge density of assemblies. Flat surfaces have lower charge densities than curved surfaces due to closer packing constraints. However, we note that the flat geometry would also change the measured Zeta potential (e.g. spherical and planar structures have different diffusion coefficients affecting mobility) and the location of condensed ions (i.e. h) so this comparison is only an approximation for the purpose of demonstrating geometric effects on charged assemblies.

4.8D shows the comparison of charge density calculated using various methods at pH$\simeq 6$ (high degree of ionization, $\alpha = 1$). There is reasonable agreement between the charge density calculated from the Zeta potential and curved Grahame equation (blue, equation 4.5) and the charge density calculated from the electrostatic model of titration using the bare charge (green dashed, equation 4.3) at low ionic strength. However, around an ionic strength of 23.3 mM, which corresponds to $a = R/\lambda_D = 1$, the bare charge begins to overestimate the charge compared to that measured using the Zeta potential. At this point, as was demonstrated in the previous section, it is more appropriate to use some type of effective charge and effective potential to describe the micellar assemblies (green solid). The agreement between the effective charge density and the charge density measured using the Zeta potential becomes better at higher ionic strengths. Limitations arise in middle regions of ionic strength where it is unclear if the bare charge or effective charge should be used to model the micellar assemblies. In addition, there may be limitations to our hypothesized Ψ_{eff}.

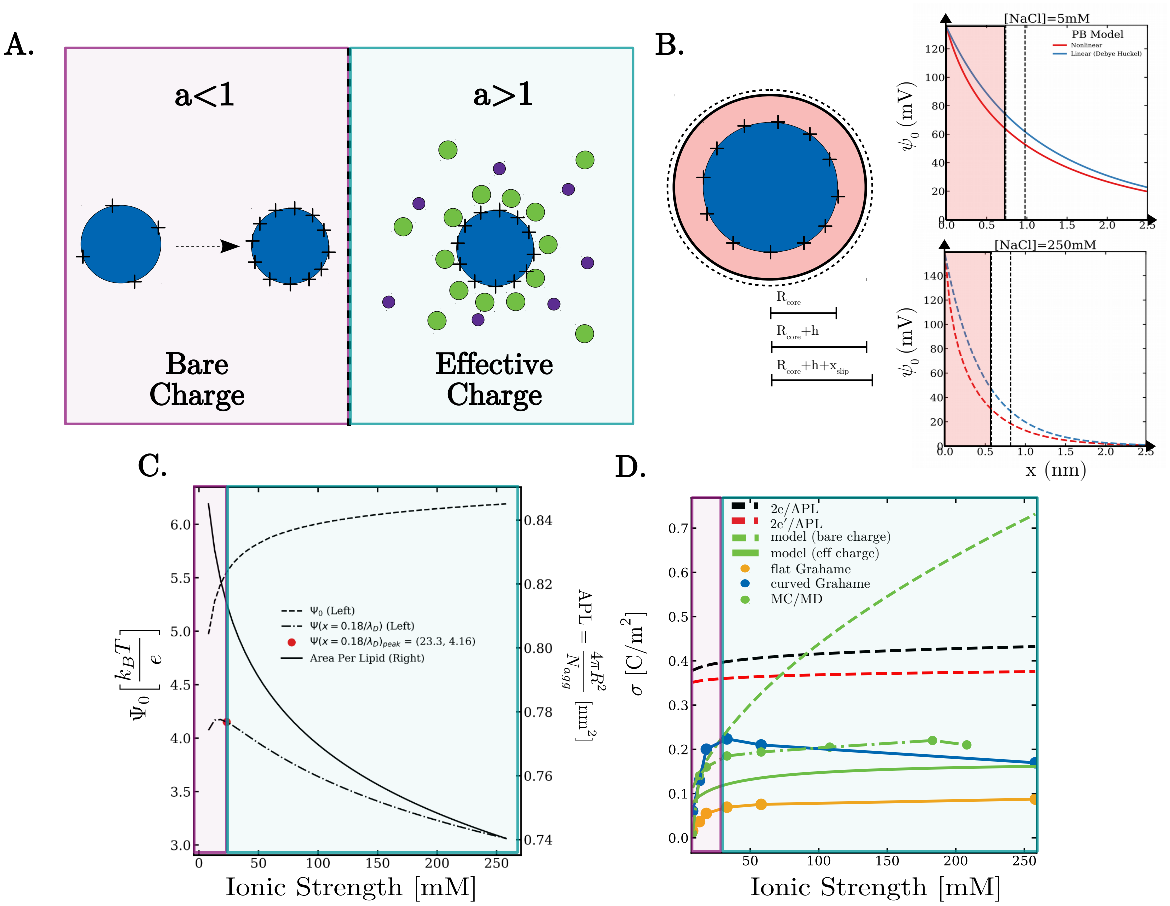

Figure 4.8: Calculating Charge through Zeta potential and PB model A. Schematic of bare charge vs effective charge. The bare charge increases monotonically for increasing electrostatic surface potential whereas the effective charge plateaus due condensed ions near the charged surface. **B.** The micelle core, shell, and slipping plane regions are shown in a schematic. A comparison of the electrostatic potential as a function of distance from the surface of the nonlinear and linearized PB models for $C_{16}K_2$ micelles in [NaCl] = 5mM and 250mM (55 mV=2.15 kT/e). The nonlinear PB model has a sharp decrease near the surface of the assemblies, within the shell and slip plane regions, due to the nonlinearity. **C.** The electrostatic potential on the surface of the micelle, the effective potential at $x = 0.18$nm away from the surface, and the area per lipid as a function of ionic strength. The labelled red point corresponds to the transition point for $a = R/\lambda_D$ proceeds from <1 to >1. We note it is very close to the peak effective potential value. **D.** Comparison of charge density as a function of salt concentration using various methods discussed in text is shown.

To more accurately model the effective charge of $C_{16}K_2$ assemblies we performed hybrid Monte

Carlo/Molecular Dynamics (MCMD) simulations, which take into effect charge regulation effects as well as finite sized ion dynamics. MCMD simulations were run at pH 6 (where micelle headgroups are all expected to be ionized) for 0, 5, 10, 25, 50, 100, 175, and 200 mM added NaCl. The charge density in those simulations is calculated from the radial distribution function, $g(r)$, of negatively charged ions (ρ_{-}) surrounding the positively charged micelle assembly (4.7). Details can be found in C.4.

$$\sigma = \frac{N_{-}e}{4\pi R^2} \tag{4.7}$$

where $N_{-} = 4\pi\rho_{-}\int_0^{r_{max}} r^2 g(r)dr$. r_{max} encompasses the first prominent peak in the radial distribution function corresponding to the first layer of negatively charged ions surrounding the micelle. Charge density calculation results from the MCMD simulations are shown in Figure 4.8D, which lie in between the bare charge and hypothesized effective charge and show good agreement with zeta potential measurements at even the intermediate salt concentrations. In contrast with the nonlinear PB continuum treatment, ions are of a finite size in MD simulations. Thus, while Ψ_0 provides an accurate estimate of charge denisty at low ionic strength (< 25 mM) and Ψ_{eff} provides an estimate of the charge density at higher ionic strength (> 200 mM), discrete ion size effects need to be included for estimating the charge of C$_{16}$K$_2$ micelles in the intermediate region. MCMD simulations more accurately model the effective charge for all ionic strengths at the cost of computational efficiency compared to the analytical continuum treatment.

The upper limit of charge density calculated based on the area per lipid (black dashed, 4.8D) is also shown. This calculates the charge density from the area per lipid using 2e/APL upper limit with all lysines in their charged state (APL $= 2 \times S$) (4.8C). The 2e/APL upper limit ($\simeq 0.4$ C/m^2 $\simeq$ 2 electronic charge$/0.8$ nm^2) ignores ionic environment effects. The Grahame equation and our electrostatic model do account for the surrounding ionic environment. The degree of ionization can be somewhat corrected in a similar manner as the charge and potential to an effective degree of ionization by considering a Manning condensation layer of ions: $\alpha' \rightarrow \frac{r}{l_B}\alpha$, where $r \simeq \sqrt{S}$ is the average distance between the ionizable sites [119, 168, 169]. With this correction to the 2e/APL limit (4.8D, red dashed) we still see that the effective charge of C$_{16}$K$_2$ molecules in assembly is lower than expected. Such findings may be important to consider in other PA systems with multiple amino acids in the head group. We note one interesting possibility is that the inner lysine of $C_{16}K_2$ may be less prone to be in its charged state due to its vicinity to the non-polar hydrophobic core leading to more alterations on the effective degree of ionization. The current model treats all lysines in $C_{16}K_2$ equivalently so we can not make any conclusions regarding this finding.

4.4 Summary and Future Work

In conclusion, we have provided an intuitive understanding to titration curves of soft ionizable assemblies and the effect of geometry on charge regulation. (1) We provided a methodology for analyzing titration curves by combining structural information from SAXS and an electrostatic model based on principles of physics. (2) We showed that a nonlinear PB electrostatic model can capture degree of ionization behavior without the need for a $\mathrm{p}K_{a,\mathrm{eff}}$ parameter. (3) We calculated the charge of $C_{16}K_2$ assemblies and discussed discrepancies.

Future work will be focused on the numerical modelling of charge regulation and ion distributions in more complex geometries. PAs assemble into a variety of supramolecular shapes including twisted and helical ribbons that can be controlled by tuning the ionic enviroment. Combining charge regulation concepts and other X-ray scattering techniques would provide a robust way to characterize surface charges of PA assemblies.

5 Conclusion and outlook

"*If you are a true student, you will be more dissatisfied with yourself when you graduate than you are now.*"

-Sir Frederick Grant Banting

5.1 Summary of Findings

Our combined experimental, computational, and theoretical study yields insight into attaining a variety chiral assembly structures and controlling their internal architecture by tuning the electrostatics of the system. In this way, we have shown that electrostatic interactions can direct chiral shape selection. To reiterate a key finding, helicoidal scrolls (cochleates) are observed in salt solutions when the intermolecular electrostatic interactions are screened and short-ranged and helical ribbons are observed under conditions when the degree of ionization is low, but the electrostatic interactions are long-ranged. We provided a methodology for further analyzing degree of ionization behavior in highly charged ionizable assemblies by analyzing titration curves with an electrostatic model that combined nano-scale structural details and fundamental principles of physics of electrostatic interactions in solution. We have demonstrated that the simple (if not simplest) charged, chiral molecule, C_nK_1, is a suitable molecular system for the exploration of the charged, chiral assembly phase space. In this way, we have provided a step towards a rational bottom-top electrostatic-based design framework for the hierarchical structure of charged, chiral molecular materials.

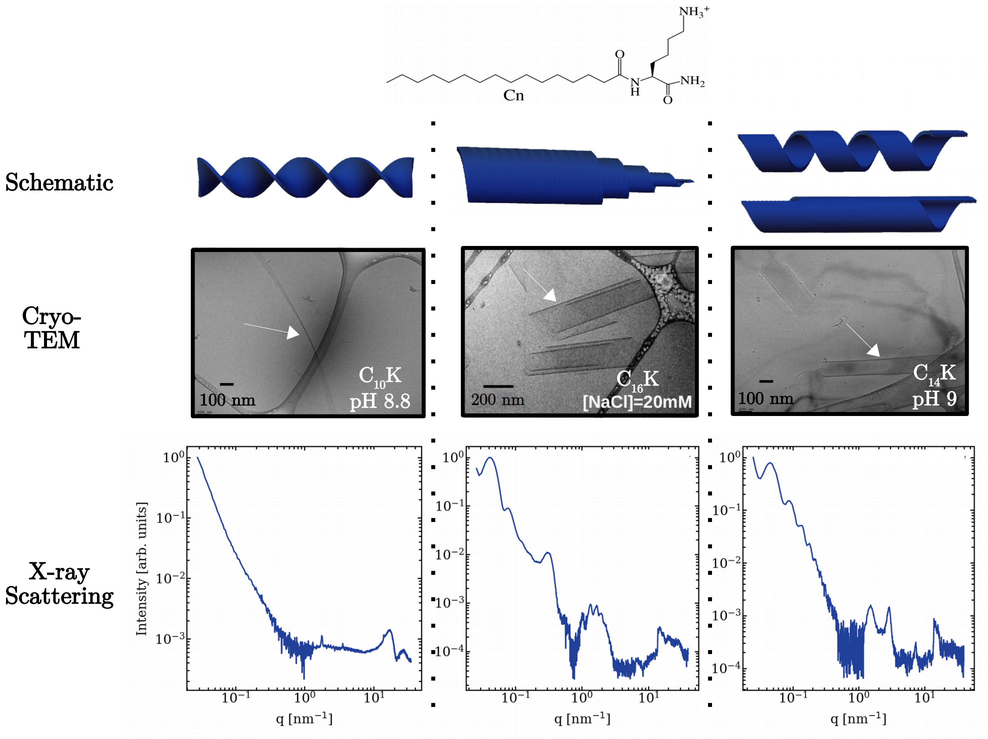

Figure 5.1: Experimental observations of the C_nK_1 molecular series is outlined via a schematic, a real-space cryo-TEM image, and a reciprocal-space scattering profile for different structures formed by C_nK_1 solutions in different ionic environments. Left: 40mM $C_{10}K_1$ solutions show molecules assemble into twisted ribbon bilayers upon an increase of pH. Center: 4mM $C_{16}K_1$ solution show molecules assemble into scroll-like cochleate assemblies upon an increase of monovalent salt concentraion, [NaCl]. Right: 4mM $C_{14}K_1$ solutions show molecules assemble into helical ribbon bilayers upon an increase of pH that stack on top of one another.

5.2 Future and Outlook

This study has provided preliminary results in controlling chiral shape selection of charged chiral molecules, but many questions remain unanswered.

5.2.1 Further exploration of C_nK_1 phase space

Chapter 3 demonstrated a necessity for refined characterization of crystallinity in $C_{10}K_1$ twisted ribbon bilayers. For example, the doublet diffraction peak discussed in 3.3.2.3, a seeming signature of twisted ribbon C$_{10}$K$_1$ assemblies, is not well understood. In addition, understanding precise pathways for how C$_n$K$_1$ assembly parameters (such as radius, pitch, and width) depend on elastic and electrostatic properties of membranes has remained elusive. Attempts were made to calculate elastic properties of C$_n$K$_1$ bilayers to relate assembly structures to measured bending rigidities, but current MD simulations lack the crystalline order features that are apparent in scattering profiles. Finally, further characterization of C$_n$K$_1$ tail tilt and headgroup ordering in the different bilayer assembies (cochleate, helical ribbon, twisted ribbon) is necessary to compare findings to existing models of chiral molecular assemblies. Chapter 2 showed preliminary efforts in this regard using MD simulations, but robust characterization of the WAXS in different assembly geometries would provide definitive conclusions. For example, C$_{18}$K$_1$ showed persistent diffraction peaks related to molecular ordering throughout the planar ribbon to helical ribbon transformation that require further WAXS modelling and analysis.

5.2.2 Long term stability and dynamics of helical ribbons (and other chiral assemblies)

Studies have suggested the instability of the helical ribbon morphology (Figure 5.2) [1, 21, 74, 116]. For example, cryo-TEM measurements of C$_{14}$K$_1$ helical ribbons, performed a few days after sample preparation, show aggregations of helical structures with minimal helical windings visible, but still containing a slanted terminal edge consistent with a closed helical ribbon morphology (5.1, right). Due to the relatively weak non-covalent interactions that hold together the assemblies and the dynamic features, studies chiral nanostructures mainly focus on systems at equilibrium, as done in this study. During the thermodynamically equilibrated self-assembly, metastable chiral assemblies may be formed firstly, but finally transform into a more thermodynamically stable state with a different chiral structures. Thermodynamically equilibrated nanostructures can persist for a long time due to their thermodynamic stability. The size of the energy barrier between a stable and metastable state dictates whether or not a metastable state can be maintained or not. Understanding these properties of C$_n$K$_1$ systems would allow for the generation and control of additional chiral assembly states. External physical stimuli, such as sonication, stirring, could accelerate the interconversion from a metastable state to stable by eliminating the energy barriers. Maintaining an metastable state with a low energy barrier would require a continuous supply of energy to maintain their structures, as is the case in living biological systems. Continuous energy-driven transformation makes it possible to construct more elaborate far-from-equilibrium structures with additional functions.

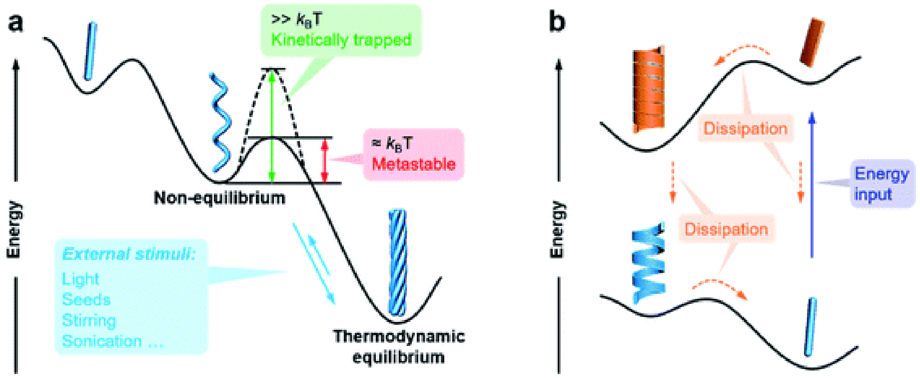

Figure 5.2: Taken from [1]. Energy landscapes illustrating the formation and transformation of different chiral nanostructures through hierarchical self-assembly. (a) Non-equilibrium, thermodynamic equilibrium, and (b) far-from-equilibrium self-assembly.

Finally, it is worth noting that a system in thermodynamic equilibrium conditions may still be dynamic. Specifically, although the overall system does not change over time, monomers continuously assemble/disassemble or ionize/deionize at a certain rate. This can bring the system to new thermodynamic equilibrium conditions and were not taken into account in this work. Understanding the dynamics of the charge regulation process in complicated geometries is vital to controlling C_nK_1 assemblies with electrostatics/electrodynamics. These further studies, in conjunction with investigations of the dynamics of C_nK_1 nanostructures, would allow for the transformation of chiral nanostructures to additional assembly states.

References

[1] Sang, Y. and M. Liu, “Hierarchical self-assembly into chiral nanostructures”, en, Chemical Science **13**, 633–656 (2022) (cit. on pp. 17, 18, 84, 139, 140).

[2] Nakashima, N., S. Asakuma, and T. Kunitake, “Optical microscopic study of helical superstructures of chiral bilayer membranes”, en, Journal of the American Chemical Society **107**, 509–510 (1985) (cit. on pp. 17, 18, 48).

[3] Georger, J. H., A. Singh, R. R. Price, J. M. Schnur, P. Yager, and P. E. Schoen, “Helical and tubular microstructures formed by polymerizable phosphatidylcholines”, en, Journal of the American Chemical Society **109**, 6169–6175 (1987) (cit. on pp. 17, 18, 48, 50, 68, 72).

[4] Schnur, J. M., B. R. Ratna, J. V. Selinger, A. Singh, G. Jyothi, and K. R. K. Easwaran, “Diacetylenic Lipid Tubules: Experimental Evidence for a Chiral Molecular Architecture”, en, Science **264**, 945–947 (1994) (cit. on pp. 17, 30, 48, 50, 72).

[5] Shimizu, T., M. Masuda, and H. Minamikawa, “Supramolecular Nanotube Architectures Based on Amphiphilic Molecules”, en, Chemical Reviews **105**, 1401–1444 (2005) (cit. on pp. 17, 21, 48, 49).

[6] Barclay, T. G., K. Constantopoulos, and J. Matisons, “Nanotubes Self-Assembled from Amphiphilic Molecules via Helical Intermediates”, en, Chemical Reviews **114**, 10217–10291 (2014) (cit. on pp. 17, 21, 48, 49).

[7] Zhang, L., T. Wang, Z. Shen, and M. Liu, “Chiral Nanoarchitectonics: Towards the Design, Self-Assembly, and Function of Nanoscale Chiral Twists and Helices”, en, Advanced Materials **28**, 1044–1059 (2016) (cit. on pp. 17, 48).

[8] Pashuck, E. T. and S. I. Stupp, “Direct Observation of Morphological Tranformation from Twisted Ribbons into Helical Ribbons”, en, Journal of the American Chemical Society **132**, 8819–8821 (2010) (cit. on pp. 17, 48).

[9] Oda, R., I. Huc, M. Schmutz, S. J. Candau, and F. C. MacKintosh, “Tuning bilayer twist using chiral counterions”, en, Nature **399**, 566–569 (1999) (cit. on pp. 17, 48, 49, 83, 99, 100).

[10] Sangji, M. H., H. Sai, S. M. Chin, S. R. Lee, I. R Sasselli, L. C. Palmer, and S. I. Stupp, “Supramolecular Interactions and Morphology of Self-Assembling Peptide Amphiphile Nanostructures”, en, Nano Letters **21**, 6146–6155 (2021) (cit. on pp. 17, 48).

[11] Papahadjopoulos, D., W. Vail, K. Jacobson, and G. Poste, “Cochleate lipid cylinders: formation by fusion of unilamellar lipid vesicles”, en, Biochimica et Biophysica Acta (BBA) - Biomembranes **394**, 483–491 (1975) (cit. on pp. 17, 18, 34, 48, 50, 72).

[12] Pawar, A., C. Bothiraja, K. Shaikh, and A. Mali, “An insight into cochleates, a potential drug delivery system”, en, RSC Advances **5**, 81188–81202 (2015) (cit. on pp. 17, 18, 20, 33, 34, 48–50, 72, 84, 94).

[13] Nagarsekar, K., M. Ashtikar, F. Steiniger, J. Thamm, F. Schacher, and A. Fahr, “Understanding cochleate formation: insights into structural development”, en, Soft Matter **12**, 3797–3809 (2016) (cit. on pp. 17, 18, 34, 35, 48, 50, 72).

[14] Gao, C., H. Li, Y. Li, S. Kewalramani, L. C. Palmer, V. P. Dravid, S. I. Stupp, M. Olvera De La Cruz, and M. J. Bedzyk, “Electrostatic Control of Polymorphism in Charged Amphiphile Assemblies”, en, The Journal of Physical Chemistry B **121**, 1623–1628 (2017) (cit. on pp. 17, 35, 39, 58, 76, 111, 117, 121).

[15] Ouyang, G., L. Ji, Y. Jiang, F. Würthner, and M. Liu, “Self-assembled Möbius strips with controlled helicity”, en, Nature Communications **11**, 5910 (2020) (cit. on pp. 17, 48).

[16] Harris, A. B., R. D. Kamien, and T. C. Lubensky, “Molecular chirality and chiral parameters”, en, Reviews of Modern Physics **71**, 1745–1757 (1999) (cit. on pp. 17, 49).

[17] Selinger, J. V., M. S. Spector, and J. M. Schnur, “Theory of Self-Assembled Tubules and Helical Ribbons”, en, The Journal of Physical Chemistry B **105**, 7157–7169 (2001) (cit. on pp. 17, 23–25, 43, 46, 49, 77, 99, 100, 102).

[18] Frenz, *Origin of Life-An Explanation of What is Needed for Abiogenesis (or Biopoiesis)*, en, July 2020 (cit. on p. 18).

[19] Thomas, B. N., C. R. Safinya, R. J. Plano, and N. A. Clark, “Lipid Tubule Self-Assembly: Length Dependence on Cooling Rate Through a First-Order Phase Transition”, en, Science **267**, 1635–1638 (1995) (cit. on pp. 18, 49, 50, 61, 72, 99).

[20] Uesaka, A., M. Ueda, A. Makino, T. Imai, J. Sugiyama, and S. Kimura, “Morphology Control between Twisted Ribbon, Helical Ribbon, and Nanotube Self-Assemblies with His-Containing Helical Peptides in Response to pH Change”, en, Langmuir **30**, 1022–1028 (2014) (cit. on pp. 18, 50, 109).

[21] Adamcik, J. and R. Mezzenga, “Adjustable twisting periodic pitch of amyloid fibrils”, en, Soft Matter **7**, 5437 (2011) (cit. on pp. 19, 34, 50, 74, 76, 139).

[22] Siegel, E., *This Is The One Symmetry That The Universe Must Never Violate*, en (cit. on p. 19).

[23] Brizard, A., R. Oda, and I. Huc, “Chirality Effects in Self-assembled Fibrillar Networks”, in *Low Molecular Mass Gelator*, Vol. 256 (Springer Berlin Heidelberg, Berlin, Heidelberg, 2005), pp. 167–218 (cit. on pp. 20, 24, 99, 100).

[24] Chung, D. S., G. B. Benedek, F. M. Konikoff, and J. M. Donovan, “Elastic free energy of anisotropic helical ribbons as metastable intermediates in the crystallization of cholesterol.”,

en, Proceedings of the National Academy of Sciences **90**, 11341–11345 (1993) (cit. on pp. 20, 25, 48, 73, 84).

[25] Yang, B., S. Kamiya, Y. Shimizu, N. Koshizaki, and T. Shimizu, "Glycolipid Nanotube Hollow Cylinders as Substrates: Fabrication of One-Dimensional Metallic−Organic Nanocomposites and Metal Nanowires", en, Chemistry of Materials **16**, 2826–2831 (2004) (cit. on pp. 20, 49).

[26] Sone, E. D., E. R. Zubarev, and S. I. Stupp, "Semiconductor Nanohelices Templated by Supramolecular Ribbons", en, Angewandte Chemie International Edition **41**, 1705–1709 (2002) (cit. on pp. 20, 34, 49).

[27] Zhou, Y. and T. Shimizu, "Lipid Nanotubes: A Unique Template To Create Diverse One-Dimensional Nanostructures", en, Chemistry of Materials **20**, 625–633 (2008) (cit. on p. 21).

[28] Schnur, J. M., "Lipid Tubules: A Paradigm for Molecularly Engineered Structures", en, Science **262**, 1669–1676 (1993) (cit. on pp. 21, 49).

[29] Israelachvili, J., *Intermolecular and Surface Forces*, en (Elsevier, 2011) (cit. on pp. 21, 104).

[30] Curk, T. and E. Luijten, "Charge Regulation Effects in Nanoparticle Self-Assembly", en, Physical Review Letters **126**, 138003 (2021) (cit. on pp. 23, 109, 174).

[31] Kirkwood, J. G. and J. B. Shumaker, "Forces between Protein Molecules in Solution Arising from Fluctuations in Proton Charge and Configuration", en, Proceedings of the National Academy of Sciences **38**, 863–871 (1952) (cit. on pp. 23, 109).

[32] Selinger, J. V. and J. M. Schnur, "Theory of chiral lipid tubules", en, Physical Review Letters **71**, 4091–4094 (1993) (cit. on pp. 23, 43, 45, 46, 49, 77).

[33] Harris, A. B., R. D. Kamien, and T. C. Lubensky, "Microscopic Origin of Cholesteric Pitch", en, Physical Review Letters **78**, 1476–1479 (1997) (cit. on p. 23).

[34] Canham, P., "The minimum energy of bending as a possible explanation of the biconcave shape of the human red blood cell", en, Journal of Theoretical Biology **26**, 61–81 (1970) (cit. on pp. 24, 73).

[35] Helfrich, W., "Elastic Properties of Lipid Bilayers: Theory and Possible Experiments", en, Zeitschrift für Naturforschung C **28**, 693–703 (1973) (cit. on pp. 24, 73).

[36] Helfrich, W. and J. Prost, "Intrinsic bending force in anisotropic membranes made of chiral molecules", en, Physical Review A **38**, 3065–3068 (1988) (cit. on pp. 24, 43–46, 49, 77, 158, 159).

[37] Nelson, P. and T. Powers, "Renormalization of chiral couplings in titled bilayer membranes", Journal de Physique II **3**, 1535–1569 (1993) (cit. on pp. 25, 102).

[38] Tu, Z. C. and U. Seifert, “Concise theory of chiral lipid membranes”, en, Physical Review E **76**, 031603 (2007) (cit. on p. 25).

[39] Als-Nielsen, J. and D. McMorrow, *Elements of Modern X-ray Physics*, en, 1st ed. (Wiley, Mar. 2011) (cit. on pp. 28, 62).

[40] Cantor, C. R. and P. R. Schimmel, *Biophysical chemistry* (W. H. Freeman, San Francisco, 1980) (cit. on pp. 30, 109).

[41] Rodger, A. and B. Nordén, *Circular dichroism and linear dichroism*, Oxford chemistry masters 1 (Oxford University Press, Oxford ; New York, 1997) (cit. on p. 30).

[42] Bramer, T., N. Dew, and K. Edsman, “Pharmaceutical applications for catanionic mixtures”, en, Journal of Pharmacy and Pharmacology **59**, 1319–1334 (2010) (cit. on p. 33).

[43] Torchilin, V. P., “Recent advances with liposomes as pharmaceutical carriers”, en, Nature Reviews Drug Discovery **4**, 145–160 (2005) (cit. on p. 33).

[44] Rösler, A., G. W. Vandermeulen, and H.-A. Klok, “Advanced drug delivery devices via self-assembly of amphiphilic block copolymers”, en, Advanced Drug Delivery Reviews **53**, 95–108 (2001) (cit. on p. 33).

[45] Goldberg, M., R. Langer, and X. Jia, “Nanostructured materials for applications in drug delivery and tissue engineering”, en, Journal of Biomaterials Science, Polymer Edition **18**, 241–268 (2007) (cit. on p. 33).

[46] Matson, J. B. and S. I. Stupp, “Self-assembling peptide scaffolds for regenerative medicine”, en, Chem. Commun. **48**, 26–33 (2012) (cit. on p. 33).

[47] Hosseinkhani, H., P.-D. Hong, and D.-S. Yu, “Self-Assembled Proteins and Peptides for Regenerative Medicine”, en, Chemical Reviews **113**, 4837–4861 (2013) (cit. on p. 33).

[48] Yemini, M., M. Reches, J. Rishpon, and E. Gazit, “Novel Electrochemical Biosensing Platform Using Self-Assembled Peptide Nanotubes”, en, Nano Letters **5**, 183–186 (2005) (cit. on p. 33).

[49] Kazantsev, R. V., A. J. Dannenhoffer, A. S. Weingarten, B. T. Phelan, B. Harutyunyan, T. Aytun, A. Narayanan, D. J. Fairfield, J. Boekhoven, H. Sai, A. Senesi, P. I. O’Dogherty, L. C. Palmer, M. J. Bedzyk, M. R. Wasielewski, and S. I. Stupp, “Crystal-Phase Transitions and Photocatalysis in Supramolecular Scaffolds”, en, Journal of the American Chemical Society **139**, 6120–6127 (2017) (cit. on pp. 33–35, 72).

[50] Weingarten, A. S., R. V. Kazantsev, L. C. Palmer, M. McClendon, A. R. Koltonow, A. P. S. Samuel, D. J. Kiebala, M. R. Wasielewski, and S. I. Stupp, “Self-assembling hydrogel scaffolds for photocatalytic hydrogen production”, en, Nature Chemistry **6**, 964–970 (2014) (cit. on pp. 33, 35).

[51] Kaufman, Y., A. Berman, and V. Freger, “Supported Lipid Bilayer Membranes for Water Purification by Reverse Osmosis”, en, Langmuir **26**, 7388–7395 (2010) (cit. on p. 33).

[52] Hamley, I. W., “Self-assembly of amphiphilic peptides”, en, Soft Matter **7**, 4122 (2011) (cit. on pp. 34, 100, 109).

[53] Cui, H., M. J. Webber, and S. I. Stupp, “Self-assembly of peptide amphiphiles: From molecules to nanostructures to biomaterials”, en, Biopolymers **94**, 1–18 (2010) (cit. on p. 34).

[54] Castelletto, V., I. W. Hamley, J. Perez, L. Abezgauz, and D. Danino, “Fibrillar superstructure from extended nanotapes formed by a collagen-stimulating peptide”, en, Chemical Communications **46**, 9185 (2010) (cit. on p. 34).

[55] Cui, H., T. Muraoka, A. G. Cheetham, and S. I. Stupp, “Self-Assembly of Giant Peptide Nanobelts”, en, Nano Letters **9**, 945–951 (2009) (cit. on pp. 34, 39).

[56] Cui, H., A. G. Cheetham, E. T. Pashuck, and S. I. Stupp, “Amino Acid Sequence in Constitutionally Isomeric Tetrapeptide Amphiphiles Dictates Architecture of One-Dimensional Nanostructures”, en, Journal of the American Chemical Society **136**, 12461–12468 (2014) (cit. on p. 34).

[57] Yao, Z. and M. Olvera De La Cruz, “Electrostatics-Driven Hierarchical Buckling of Charged Flexible Ribbons”, en, Physical Review Letters **116**, 148101 (2016) (cit. on p. 34).

[58] Weingarten, A. S., R. V. Kazantsev, L. C. Palmer, D. J. Fairfield, A. R. Koltonow, and S. I. Stupp, “Supramolecular Packing Controls H $_2$ Photocatalysis in Chromophore Amphiphile Hydrogels”, en, Journal of the American Chemical Society **137**, 15241–15246 (2015) (cit. on p. 35).

[59] Lehrman, J. A., H. Cui, W.-W. Tsai, T. J. Moyer, and S. I. Stupp, “Supramolecular control of self-assembling terthiophene–peptide conjugates through the amino acid side chain”, en, Chemical Communications **48**, 9711 (2012) (cit. on p. 35).

[60] Rappe, A. K., C. J. Casewit, K. S. Colwell, W. A. Goddard, and W. M. Skiff, “UFF, a full periodic table force field for molecular mechanics and molecular dynamics simulations”, en, Journal of the American Chemical Society **114**, 10024–10035 (1992) (cit. on p. 36).

[61] McCourt, J. M., S. Kewalramani, C. Gao, E. W. Roth, S. J. Weigand, M. Olvera de la Cruz, and M. J. Bedzyk, “Electrostatic Control of Shape Selection and Nanoscale Structure in Chiral Molecular Assemblies”, en, ACS Central Science **8**, 1169–1181 (2022) (cit. on pp. 38, 43, 84, 88, 95, 98, 100, 106, 109).

[62] Wallace, J. M., “Applications of atomic force microscopy for the assessment of nanoscale morphological and mechanical properties of bone”, en, Bone **50**, 420–427 (2012) (cit. on p. 39).

[63] Huang, Q., H. Wu, P. Cai, J. B. Fein, and W. Chen, “Atomic force microscopy measurements of bacterial adhesion and biofilm formation onto clay-sized particles”, en, Scientific Reports **5**, 16857 (2015) (cit. on p. 39).

[64] Komura, S., H. Shirotori, and T. Kato, “Phase behavior of charged lipid bilayer membranes with added electrolyte”, en, The Journal of Chemical Physics **119**, 1157–1164 (2003) (cit. on p. 44).

[65] Onuki, A., “Surface tension of electrolytes: Hydrophilic and hydrophobic ions near an interface”, en, The Journal of Chemical Physics **128**, 224704 (2008) (cit. on p. 44).

[66] Harden, J. L., C. Marques, J. F. Joanny, and D. Andelman, “Membrane curvature elasticity in weakly charged lamellar phases”, en, Langmuir **8**, 1170–1175 (1992) (cit. on pp. 45, 159).

[67] Rowat, A. C., P. L. Hansen, and J. H. Ipsen, “Experimental evidence of the electrostatic contribution to membrane bending rigidity”, Europhysics Letters (EPL) **67**, 144–149 (2004) (cit. on p. 45).

[68] Norrish, K., “The swelling of montmorillonite”, en, Discussions of the Faraday Society **18**, 120 (1954) (cit. on p. 46).

[69] Tester, C. C., S. Aloni, B. Gilbert, and J. F. Banfield, “Short- and Long-Range Attractive Forces That Influence the Structure of Montmorillonite Osmotic Hydrates”, en, Langmuir **32**, 12039–12046 (2016) (cit. on p. 46).

[70] Nagarsekar, K., M. Ashtikar, J. Thamm, F. Steiniger, F. Schacher, A. Fahr, and S. May, “Electron Microscopy and Theoretical Modeling of Cochleates”, en, Langmuir **30**, 13143–13151 (2014) (cit. on p. 46).

[71] Hamley, I. W., A. Dehsorkhi, and V. Castelletto, “Self-assembled arginine-coated peptide nanosheets in water”, en, Chemical Communications **49**, 1850 (2013) (cit. on pp. 48, 76, 83).

[72] Qi, R., J. Liu, N. Zhang, X. Ji, Y. Han, and Y. Wang, “Assembly and Evolution of Gemini-Type Peptide Amphiphile with a Di-Lysine Spacer”, en, Langmuir **35**, 6154–6160 (2019) (cit. on p. 48).

[73] Gao, C., S. Kewalramani, D. M. Valencia, H. Li, J. M. McCourt, M. Olvera De La Cruz, and M. J. Bedzyk, “Electrostatic shape control of a charged molecular membrane from ribbon to scroll”, en, Proceedings of the National Academy of Sciences **116**, 22030–22036 (2019) (cit. on pp. 48, 49, 51, 60, 72, 81, 84, 89, 92).

[74] Ziserman, L., H.-Y. Lee, S. R. Raghavan, A. Mor, and D. Danino, “Unraveling the Mechanism of Nanotube Formation by Chiral Self-Assembly of Amphiphiles”, en, Journal of the American Chemical Society **133**, 2511–2517 (2011) (cit. on pp. 49, 61, 74, 76, 139).

[75] Dehsorkhi, A., V. Castelletto, and I. W. Hamley, “Self-assembling amphiphilic peptides”, en, Journal of Peptide Science **20**, 453–467 (2014) (cit. on pp. 50, 84, 85, 109).

[76] Makovitzki, A., J. Baram, and Y. Shai, "Antimicrobial Lipopolypeptides Composed of Palmitoyl Di- and Tricationic Peptides: *In Vitro* and *in Vivo* Activities, Self-Assembly to Nanostructures, and a Plausible Mode of Action †", en, Biochemistry **47**, 10630–10636 (2008) (cit. on pp. 51, 111).

[77] Hess, B., C. Kutzner, D. Van Der Spoel, and E. Lindahl, "GROMACS 4: Algorithms for Highly Efficient, Load-Balanced, and Scalable Molecular Simulation", en, Journal of Chemical Theory and Computation **4**, 435–447 (2008) (cit. on pp. 55, 88).

[78] Gowers, R., M. Linke, J. Barnoud, T. Reddy, M. Melo, S. Seyler, J. Domański, D. Dotson, S. Buchoux, I. Kenney, and O. Beckstein, "MDAnalysis: A Python Package for the Rapid Analysis of Molecular Dynamics Simulations", in (2016), pp. 98–105 (cit. on p. 55).

[79] Michaud-Agrawal, N., E. J. Denning, T. B. Woolf, and O. Beckstein, "MDAnalysis: A toolkit for the analysis of molecular dynamics simulations", en, Journal of Computational Chemistry **32**, 2319–2327 (2011) (cit. on p. 55).

[80] Schrödinger, LLC, "The PyMOL Molecular Graphics System, Version 1.8", Nov. 2015 (cit. on p. 55).

[81] Humphrey, W., A. Dalke, and K. Schulten, "VMD: Visual molecular dynamics", en, Journal of Molecular Graphics **14**, 33–38 (1996) (cit. on p. 55).

[82] Huang, J., S. Rauscher, G. Nawrocki, T. Ran, M. Feig, B. L. De Groot, H. Grubmüller, and A. D. MacKerell, "CHARMM36m: an improved force field for folded and intrinsically disordered proteins", en, Nature Methods **14**, 71–73 (2017) (cit. on pp. 55, 88).

[83] MacKerell, A. D., D. Bashford, M. Bellott, R. L. Dunbrack, J. D. Evanseck, M. J. Field, S. Fischer, J. Gao, H. Guo, S. Ha, D. Joseph-McCarthy, L. Kuchnir, K. Kuczera, F. T. K. Lau, C. Mattos, S. Michnick, T. Ngo, D. T. Nguyen, B. Prodhom, W. E. Reiher, B. Roux, M. Schlenkrich, J. C. Smith, R. Stote, J. Straub, M. Watanabe, J. Wiórkiewicz-Kuczera, D. Yin, and M. Karplus, "All-Atom Empirical Potential for Molecular Modeling and Dynamics Studies of Proteins", en, The Journal of Physical Chemistry B **102**, 3586–3616 (1998) (cit. on p. 55).

[84] Cantor, C. R. and P. R. Schimmel, *The behavior of biological macromolecules*, Their Biophysical chemistry ; pt. 3 (W. H. Freeman, San Francisco, 1980) (cit. on pp. 56, 58, 166).

[85] Haynes, W. M., D. R. Lide, and T. J. Bruno, *CRC handbook of chemistry and physics: a ready reference book of chemical and physical data*, eng, 93rd ed (CRC, Boca Raton, 2012) (cit. on pp. 58, 97, 116).

[86] Zaldivar, G., S. Vemulapalli, V. Udumula, M. Conda-Sheridan, and M. Tagliazucchi, "Self-Assembled Nanostructures of Peptide Amphiphiles: Charge Regulation by Size Regulation", en, The Journal of Physical Chemistry C **123**, 17606–17615 (2019) (cit. on pp. 58, 76, 98, 111, 129).

[87] Selinger, R. L. B., J. V. Selinger, A. P. Malanoski, and J. M. Schnur, “Shape Selection in Chiral Self-Assembly”, en, Physical Review Letters **93**, 158103 (2004) (cit. on pp. 60, 61).

[88] Sawa, Y., F. Ye, K. Urayama, T. Takigawa, V. Gimenez-Pinto, R. L. B. Selinger, and J. V. Selinger, “Shape selection of twist-nematic-elastomer ribbons”, en, Proceedings of the National Academy of Sciences **108**, 6364–6368 (2011) (cit. on p. 60).

[89] Cevc, G., “How membrane chain melting properties are regulated by the polar surface of the lipid bilayer”, en, Biochemistry **26**, 6305–6310 (1987) (cit. on p. 61).

[90] Nallet, F., R. Laversanne, and D. Roux, “Modelling X-ray or neutron scattering spectra of lyotropic lamellar phases : interplay between form and structure factors”, Journal de Physique II **3**, 487–502 (1993) (cit. on pp. 63, 71).

[91] Ocko, B. M., X. Z. Wu, E. B. Sirota, S. K. Sinha, O. Gang, and M. Deutsch, “Surface freezing in chain molecules: Normal alkanes”, en, Physical Review E **55**, 3164–3182 (1997) (cit. on pp. 63, 74).

[92] Pringle, O. A. and P. W. Schmidt, “Small-angle X-ray scattering from helical macromolecules”, Journal of Applied Crystallography **4**, 290–293 (1971) (cit. on pp. 65, 94).

[93] Terech, P., S. K. P. Velu, P. Pernot, and L. Wiegart, “Salt Effects in the Formation of Self-Assembled Lithocholate Helical Ribbons and Tubes”, en, The Journal of Physical Chemistry B **116**, 11344–11355 (2012) (cit. on pp. 65, 94).

[94] Jaehnig, F., K. Harlos, H. Vogel, and H. Eibl, “Electrostatic interactions at charged lipid membranes. Electrostatically induced tilt”, en, Biochemistry **18**, 1459–1468 (1979) (cit. on p. 80).

[95] Aroti, A., E. Leontidis, E. Maltseva, and G. Brezesinski, “Effects of Hofmeister Anions on DPPC Langmuir Monolayers at the Air−Water Interface”, en, The Journal of Physical Chemistry B **108**, 15238–15245 (2004) (cit. on p. 80).

[96] Kewalramani, S., H. Hlaing, B. M. Ocko, I. Kuzmenko, and M. Fukuto, “Effects of Divalent Cations on Phase Behavior and Structure of a Zwitterionic Phospholipid (DMPC) Monolayer at the Air−Water Interface”, en, The Journal of Physical Chemistry Letters **1**, 489–495 (2010) (cit. on p. 80).

[97] Katsaras, J., “Structure of the Subgel (Lc’) and Gel (L.beta.’) Phases of Oriented Dipalmitoylphosphatidylcholine Multibilayers”, en, The Journal of Physical Chemistry **99**, 4141–4147 (1995) (cit. on p. 80).

[98] Harutyunyan, B., A. Dannenhoffer, S. Kewalramani, T. Aytun, D. J. Fairfield, S. I. Stupp, and M. J. Bedzyk, “Molecular Packing of Amphiphilic Nanosheets Resolved by X-ray Scattering”, en, The Journal of Physical Chemistry C **121**, 1047–1054 (2017) (cit. on pp. 81, 168).

[99] Klauda, J. B., R. M. Venable, J. A. Freites, J. W. O’Connor, D. J. Tobias, C. Mondragon-Ramirez, I. Vorobyov, A. D. MacKerell, and R. W. Pastor, “Update of the CHARMM All-Atom

Additive Force Field for Lipids: Validation on Six Lipid Types”, en, The Journal of Physical Chemistry B **114**, 7830–7843 (2010) (cit. on p. 81).

[100] Leung, C.-Y., L. C. Palmer, B. F. Qiao, S. Kewalramani, R. Sknepnek, C. J. Newcomb, M. A. Greenfield, G. Vernizzi, S. I. Stupp, M. J. Bedzyk, and M. Olvera De La Cruz, “Molecular Crystallization Controlled by pH Regulates Mesoscopic Membrane Morphology”, en, ACS Nano **6**, 10901–10909 (2012) (cit. on p. 81).

[101] Liu, Z., Y. Yao, X. Tao, J. Wei, and S. Lin, “Helical Self-Assembly of Amphiphilic Chiral Azobenzene Alternating Copolymers”, en, ACS Macro Letters **10**, 1174–1179 (2021) (cit. on p. 84).

[102] Yan, J., W. Feng, J.-Y. Kim, J. Lu, P. Kumar, Z. Mu, X. Wu, X. Mao, and N. A. Kotov, “Self-Assembly of Chiral Nanoparticles into Semiconductor Helices with Tunable near-Infrared Optical Activity”, en, Chemistry of Materials **32**, 476–488 (2020) (cit. on p. 85).

[103] Tan, A., J. Rajadas, and A. M. Seifalian, “Biochemical engineering nerve conduits using peptide amphiphiles”, en, Journal of Controlled Release **163**, 342–352 (2012) (cit. on pp. 85, 109).

[104] Marrink, S. J., A. H. de Vries, and A. E. Mark, “Coarse Grained Model for Semiquantitative Lipid Simulations”, en, The Journal of Physical Chemistry B **108**, 750–760 (2004) (cit. on p. 88).

[105] Marrink, S. J., H. J. Risselada, S. Yefimov, D. P. Tieleman, and A. H. De Vries, “The MARTINI Force Field: Coarse Grained Model for Biomolecular Simulations”, en, The Journal of Physical Chemistry B **111**, 7812–7824 (2007) (cit. on pp. 88, 102, 172).

[106] De Jong, D. H., G. Singh, W. F. D. Bennett, C. Arnarez, T. A. Wassenaar, L. V. Schäfer, X. Periole, D. P. Tieleman, and S. J. Marrink, “Improved Parameters for the Martini Coarse-Grained Protein Force Field”, en, Journal of Chemical Theory and Computation **9**, 687–697 (2013) (cit. on p. 88).

[107] Yesylevskyy, S. O., L. V. Schäfer, D. Sengupta, and S. J. Marrink, “Polarizable Water Model for the Coarse-Grained MARTINI Force Field”, en, PLoS Computational Biology **6**, edited by M. Levitt, e1000810 (2010) (cit. on p. 88).

[108] Vögele, M., C. Holm, and J. Smiatek, “Properties of the polarizable MARTINI water model: A comparative study for aqueous electrolyte solutions”, en, Journal of Molecular Liquids **212**, 103–110 (2015) (cit. on p. 88).

[109] Rossi, G., L. Monticelli, S. R. Puisto, I. Vattulainen, and T. Ala-Nissila, “Coarse-graining polymers with the MARTINI force-field: polystyrene as a benchmark case”, en, Soft Matter **7**, 698–708 (2011) (cit. on p. 88).

[110] Vögele, M., C. Holm, and J. Smiatek, “Coarse-grained simulations of polyelectrolyte complexes: MARTINI models for poly(styrene sulfonate) and poly(diallyldimethylammonium)”, en, The Journal of Chemical Physics **143**, 243151 (2015) (cit. on p. 88).

[111] Van Teijlingen, A., M. C. Smith, and T. Tuttle, “Short Peptide Self-Assembly in the Martini Coarse-Grain Force Field Family”, en, Accounts of Chemical Research **56**, 644–654 (2023) (cit. on p. 88).

[112] Marrink, S. J., L. Monticelli, M. N. Melo, R. Alessandri, D. P. Tieleman, and P. C. T. Souza, “Two decades of Martini: Better beads, broader scope”, en, WIREs Computational Molecular Science **13**, `10.1002/wcms.1620` (2023) (cit. on pp. 88, 106).

[113] Monticelli, L., S. K. Kandasamy, X. Periole, R. G. Larson, D. P. Tieleman, and S.-J. Marrink, “The MARTINI Coarse-Grained Force Field: Extension to Proteins”, en, Journal of Chemical Theory and Computation **4**, 819–834 (2008) (cit. on pp. 88, 102, 172).

[114] Martínez, L., R. Andrade, E. G. Birgin, and J. M. Martínez, “PACKMOL: A package for building initial configurations for molecular dynamics simulations”, en, Journal of Computational Chemistry **30**, 2157–2164 (2009) (cit. on pp. 88, 173).

[115] Bombarda, E. and G. M. Ullmann, “pH-Dependent p K_a Values in Proteins—A Theoretical Analysis of Protonation Energies with Practical Consequences for Enzymatic Reactions”, en, The Journal of Physical Chemistry B **114**, 1994–2003 (2010) (cit. on pp. 97, 110).

[116] Armon, S., H. Aharoni, M. Moshe, and E. Sharon, “Shape selection in chiral ribbons: from seed pods to supramolecular assemblies”, en, Soft Matter **10**, 2733–2740 (2014) (cit. on pp. 100, 139).

[117] Periole, X. and S.-J. Marrink, “The Martini Coarse-Grained Force Field”, in *Biomolecular Simulations*, Vol. 924, edited by L. Monticelli and E. Salonen (Humana Press, Totowa, NJ, 2013), pp. 533–565 (cit. on p. 102).

[118] Bruininks, B. M. H., P. C. T. Souza, and S. J. Marrink, “A Practical View of the Martini Force Field”, en, in *Biomolecular Simulations*, Vol. 2022, edited by M. Bonomi and C. Camilloni (Springer New York, New York, NY, 2019), pp. 105–127 (cit. on p. 102).

[119] Manning, G. S., “Limiting Laws and Counterion Condensation in Polyelectrolyte Solutions I. Colligative Properties”, en, The Journal of Chemical Physics **51**, 924–933 (1969) (cit. on pp. 104, 135).

[120] Seifert, U., “Configurations of fluid membranes and vesicles”, en, Advances in Physics **46**, 13–137 (1997) (cit. on p. 104).

[121] Sknepnek, R., G. Vernizzi, and M. Olvera De La Cruz, “Charge renormalization of bilayer elastic properties”, en, The Journal of Chemical Physics **137**, 104905 (2012) (cit. on p. 104).

[122] Doktorova, M., D. Harries, and G. Khelashvili, “Determination of bending rigidity and tilt modulus of lipid membranes from real-space fluctuation analysis of molecular dynamics simulations”, en, Physical Chemistry Chemical Physics **19**, 16806–16818 (2017) (cit. on p. 104).

[123] Venable, R. M., F. L. Brown, and R. W. Pastor, “Mechanical properties of lipid bilayers from molecular dynamics simulation”, en, Chemistry and Physics of Lipids **192**, 60–74 (2015) (cit. on p. 104).

[124] Faizi, H. A., S. L. Frey, J. Steinkühler, R. Dimova, and P. M. Vlahovska, “Bending rigidity of charged lipid bilayer membranes”, en, Soft Matter **15**, 6006–6013 (2019) (cit. on p. 104).

[125] Steinkühler, J., E. Sezgin, I. Urbančič, C. Eggeling, and R. Dimova, “Mechanical properties of plasma membrane vesicles correlate with lipid order, viscosity and cell density”, en, Communications Biology **2**, 337 (2019) (cit. on p. 104).

[126] Boroudjerdi, H., Y. Kim, A. Naji, R. Netz, X. Schlagberger, and A. Serr, “Statics and dynamics of strongly charged soft matter”, en, Physics Reports **416**, 129–199 (2005) (cit. on p. 104).

[127] Boal, D. H., *Mechanics of the cell*, eng, 2nd ed, OCLC: 801405893 (Cambridge University Press, Cambridge, 2012) (cit. on p. 104).

[128] Stark, A. C., C. T. Andrews, and A. H. Elcock, “Toward Optimized Potential Functions for Protein–Protein Interactions in Aqueous Solutions: Osmotic Second Virial Coefficient Calculations Using the MARTINI Coarse-Grained Force Field”, en, Journal of Chemical Theory and Computation **9**, 4176–4185 (2013) (cit. on p. 106).

[129] Jung, J. H., S. Shinkai, and T. Shimizu, “Spectral Characterization of Self-Assemblies of Aldopyranoside Amphiphilic Gelators: What is the Essential Structural Difference Between Simple Amphiphiles and Bolaamphiphiles?”, Chemistry - A European Journal **8**, 2684 (2002) (cit. on p. 106).

[130] Grünewald, F., P. C. T. Souza, H. Abdizadeh, J. Barnoud, A. H. De Vries, and S. J. Marrink, “Titratable Martini model for constant pH simulations”, en, The Journal of Chemical Physics **153**, 024118 (2020) (cit. on pp. 106, 172).

[131] Hossain, S., A. Parrow, A. Kabedev, R. C. Kneiszl, Y. Leng, and P. Larsson, “Explicit-pH Coarse-Grained Molecular Dynamics Simulations Enable Insights into Restructuring of Intestinal Colloidal Aggregates with Permeation Enhancers”, en, Processes **10**, 29 (2021) (cit. on p. 106).

[132] Sami, S., F. Grünewald, P. C. T. Souza, and S. J. Marrink, “A Guide to Titratable Martini Simulations”, en, in *A Practical Guide to Recent Advances in Multiscale Modeling and Simulation of Biomolecules*, edited by Y. Wang and R. Zhou (AIP Publishing LLCMelville, New York, Jan. 2023), pp. 4–1–4–16 (cit. on pp. 106, 173).

[133] C. Holm, P. Kékicheff, and R. Podgornik, eds., *Electrostatic Effects in Soft Matter and Biophysics* (Springer Netherlands, Dordrecht, 2001) (cit. on p. 108).

[134] Ninham, B. W. and V. A. Parsegian, “Electrostatic potential between surfaces bearing ionizable groups in ionic equilibrium with physiologic saline solution”, en, Journal of Theoretical Biology **31**, 405–428 (1971) (cit. on pp. 109, 110, 115).

[135] Lund, M. and B. Jönsson, “Charge regulation in biomolecular solution”, en, Quarterly Reviews of Biophysics **46**, 265–281 (2013) (cit. on p. 109).

[136] Bakhshandeh, A., D. Frydel, A. Diehl, and Y. Levin, “Charge Regulation of Colloidal Particles: Theory and Simulations”, en, Physical Review Letters **123**, 208004 (2019) (cit. on p. 109).

[137] Bakhshandeh, A., D. Frydel, and Y. Levin, “Theory of Charge Regulation of Colloidal Particles in Electrolyte Solutions”, en, Langmuir, acs.langmuir.2c02313 (2022) (cit. on p. 109).

[138] Po, H. N. and N. M. Senozan, “The Henderson-Hasselbalch Equation: Its History and Limitations”, en, Journal of Chemical Education **78**, 1499 (2001) (cit. on p. 109).

[139] Langmuir, I., “THE CONSTITUTION AND FUNDAMENTAL PROPERTIES OF SOLIDS AND LIQUIDS. PART I. SOLIDS.”, en, Journal of the American Chemical Society **38**, 2221–2295 (1916) (cit. on p. 109).

[140] Langmuir, I., “THE ADSORPTION OF GASES ON PLANE SURFACES OF GLASS, MICA AND PLATINUM.”, en, Journal of the American Chemical Society **40**, 1361–1403 (1918) (cit. on p. 109).

[141] Onufriev, A., D. A. Case, and G. M. Ullmann, “A Novel View of pH Titration in Biomolecules”, en, Biochemistry **40**, 3413–3419 (2001) (cit. on p. 109).

[142] Bashford, D. and M. Karplus, “Multiple-site titration curves of proteins: an analysis of exact and approximate methods for their calculation”, en, The Journal of Physical Chemistry **95**, 9556–9561 (1991) (cit. on p. 110).

[143] Wang, D., R. J. Nap, I. Lagzi, B. Kowalczyk, S. Han, B. A. Grzybowski, and I. Szleifer, “How and Why Nanoparticle’s Curvature Regulates the Apparent p K_a of the Coating Ligands”, en, Journal of the American Chemical Society **133**, 2192–2197 (2011) (cit. on p. 110).

[144] Bashford, D., D. A. Case, C. Dalvit, L. Tennant, and P. E. Wright, “Electrostatic calculations of side-chain pKa values in myoglobin and comparison with NMR data for histidines”, en, Biochemistry **32**, 8045–8056 (1993) (cit. on p. 110).

[145] Hill, A. V., “The mode of action of nicotine and curari, determined by the form of the contraction curve and the method of temperature coefficients”, en, The Journal of Physiology **39**, 361–373 (1909) (cit. on p. 110).

[146] Hill, A. V., A. V. Hill, and A. Paganini-Hill, “The possible effects of the aggregation of the molecules of haemoglobin on its dissociation curves”, The Journal of Physiology **40**, 4–7 (1910) (cit. on p. 110).

[147] Weiss, J. N., “The Hill equation revisited: uses and misuses”, en, The FASEB Journal **11**, 835–841 (1997) (cit. on p. 110).

[148] Goutelle, S., M. Maurin, F. Rougier, X. Barbaut, L. Bourguignon, M. Ducher, and P. Maire, “The Hill equation: a review of its capabilities in pharmacological modelling”, en, Fundamental & Clinical Pharmacology **22**, 633–648 (2008) (cit. on p. 110).

[149] Yifrach, O., “Hill Coefficient for Estimating the Magnitude of Cooperativity in Gating Transitions of Voltage-Dependent Ion Channels”, en, Biophysical Journal **87**, 822–830 (2004) (cit. on p. 110).

[150] Colquhoun, D., “The quantitative analysis of drug–receptor interactions: a short history”, en, Trends in Pharmacological Sciences **27**, 149–157 (2006) (cit. on p. 110).

[151] Markovich, T., D. Andelman, and R. Podgornik, “Charge regulation: A generalized boundary condition?”, EPL (Europhysics Letters) **113**, 26004 (2016) (cit. on p. 110).

[152] Herrero, C. and L. Joly, “Poisson-Boltzmann formulary: Second edition”, `10.48550/ARXIV.2105.00720` (2021) (cit. on p. 110).

[153] Fogolari, F., P. Zuccato, G. Esposito, and P. Viglino, “Biomolecular Electrostatics with the Linearized Poisson-Boltzmann Equation”, en, Biophysical Journal **76**, 1–16 (1999) (cit. on p. 110).

[154] Tuinier, R., “Approximate solutions to the Poisson–Boltzmann equation in spherical and cylindrical geometry”, en, Journal of Colloid and Interface Science **258**, 45–49 (2003) (cit. on pp. 111, 112, 115, 162).

[155] Fukuto, M., R. K. Heilmann, P. S. Pershan, S. M. Yu, C. M. Soto, and D. A. Tirrell, “Internal segregation and side chain ordering in hairy-rod polypeptide monolayers at the gas/water interface: An x-ray scattering study”, en, The Journal of Chemical Physics **119**, 6253 (2003) (cit. on p. 119).

[156] Oliver, R. C., J. Lipfert, D. A. Fox, R. H. Lo, S. Doniach, and L. Columbus, “Dependence of Micelle Size and Shape on Detergent Alkyl Chain Length and Head Group”, en, PLoS ONE **8**, edited by L. Kreplak, e62488 (2013) (cit. on p. 119).

[157] Chibowski, E. and A. Szcześ, “Zeta potential and surface charge of DPPC and DOPC liposomes in the presence of PLC enzyme”, en, Adsorption **22**, 755–765 (2016) (cit. on pp. 120, 133).

[158] Hurwitz, G., G. R. Guillen, and E. M. Hoek, “Probing polyamide membrane surface charge, zeta potential, wettability, and hydrophilicity with contact angle measurements”, en, Journal of Membrane Science **349**, 349–357 (2010) (cit. on p. 120).

[159] Monnard, P.-A. and D. W. Deamer, “Membrane self-assembly processes: Steps toward the first cellular life”, en, The Anatomical Record **268**, 196–207 (2002) (cit. on p. 125).

[160] Levin, Y., E. Trizac, and L. Bocquet, “On the fluid–fluid phase separation in charged-stabilized colloidal suspensions”, Journal of Physics: Condensed Matter **15**, S3523–S3536 (2003) (cit. on p. 127).

[161] Trizac, E., L. Bocquet, and M. Aubouy, “Simple Approach for Charge Renormalization in Highly Charged Macroions”, en, Physical Review Letters **89**, 248301 (2002) (cit. on p. 127).

[162] Behrens, S. H. and D. G. Grier, “The charge of glass and silica surfaces”, The Journal of Chemical Physics **115**, 6716–6721 (2001) (cit. on pp. 127, 133).

[163] Franks, G. V., “Zeta Potentials and Yield Stresses of Silica Suspensions in Concentrated Monovalent Electrolytes: Isoelectric Point Shift and Additional Attraction”, en, Journal of Colloid and Interface Science **249**, 44–51 (2002) (cit. on p. 130).

[164] Saka, E. E. and C. Güler, “The effects of electrolyte concentration, ion species and pH on the zeta potential and electrokinetic charge density of montmorillonite”, en, Clay Minerals **41**, 853–861 (2006) (cit. on p. 130).

[165] Leroy, P., N. Devau, A. Revil, and M. Bizi, “Influence of surface conductivity on the apparent zeta potential of amorphous silica nanoparticles”, en, Journal of Colloid and Interface Science **410**, 81–93 (2013) (cit. on p. 130).

[166] Satoh, K., “Determination of binding constants of Ca2+, Na+, and Cl- ions to liposomal membranes of dipalmitoylphosphatidylcholine at gel phase by particle electrophoresis”, en, Biochimica et Biophysica Acta (BBA) - Biomembranes **1239**, 239–248 (1995) (cit. on p. 133).

[167] Zueva, O. S., V. S. Rukhlov, and Y. F. Zuev, “Morphology of Ionic Micelles as Studied by Numerical Solution of the Poisson Equation”, en, ACS Omega **7**, 6174–6183 (2022) (cit. on p. 133).

[168] Moazzami-Gudarzi, M., P. Maroni, M. Borkovec, and G. Trefalt, “Depletion and double layer forces acting between charged particles in solutions of like-charged polyelectrolytes and monovalent salts”, en, Soft Matter **13**, 3284–3295 (2017) (cit. on p. 135).

[169] Brunet, A., C. Tardin, L. Salomé, P. Rousseau, N. Destainville, and M. Manghi, “Dependence of DNA Persistence Length on Ionic Strength of Solutions with Monovalent and Divalent Salts: A Joint Theory–Experiment Study”, en, Macromolecules **48**, 3641–3652 (2015) (cit. on p. 135).

[170] Picas, L., F. Rico, and S. Scheuring, “Direct Measurement of the Mechanical Properties of Lipid Phases in Supported Bilayers”, en, Biophysical Journal **102**, L01–L03 (2012) (cit. on p. 160).

[171] Markovich, T., D. Andelman, and R. Podgornik, “Charged Membranes: Poisson–Boltzmann Theory, The DLVO Paradigm, and Beyond”, en, undefined (2016) (cit. on p. 162).

[172] Curk, T., J. Yuan, and E. Luijten, “Accelerated simulation method for charge regulation effects”, en, The Journal of Chemical Physics **156**, 044122 (2022) (cit. on p. 174).

A Chapter in Appendix

A.1 Planar Membrane Energetics

The bilayer ribbon is modeled as a parallelepiped of length L, width W, and thickness δ. The membrane energy can be written as a sum of electrostatic energy and interfacial energy, which accounts for the contact between the hydrophobic chains and water on the side faces of the ribbon.

$$H_{memb} = H_{elec} + H_{int} \tag{A.1}$$

The electrostatic energy is formulated as

$$H_{elec} = 2\int \rho(\mathbf{r})\rho(\mathbf{r'})u(\mathbf{r}-\mathbf{r'})d^3r d^3r' \tag{A.2}$$

Here, $u(\mathbf{r}-\mathbf{r'})$ is the electrostatic potential energy for interaction between two elementary charged (here two +1 charged molecules) and is approximated as

$$u(\mathbf{r}-\mathbf{r'}) \propto l_B \frac{e^{|\mathbf{r}-\mathbf{r'}|/\lambda_D}}{\mathbf{r}-\mathbf{r'}} \tag{A.3}$$

Here, the Debye length $\lambda_D \propto c^{-1/2}$ and l_B is the Bjerrum ength. $\rho(\mathbf{r})$ is the molecular charge density of the ribbon and can be approximated as $N_T = \frac{\alpha M_T}{V}$ where M_T is the total number of molecules and V is the ribbon volume, and α is the fraction of the molecules that are charged. Therefore, eq A.2 can be rewritten as

$$H_{elec} = 2\Big(\frac{N_T}{V}\Big)^2 k_B T l_B \int \frac{e^{|\mathbf{r}-\mathbf{r'}|/\lambda_D}}{\mathbf{r}-\mathbf{r'}} d^3r d^3r' \tag{A.4}$$

Table A.1: Estimates for membrane properties

Parameter	**Value**
Ribbon Area: $A = L \times W$	1 μm^2
Ribbon Thickness: δ	4 nm
Surface Molecular Density/Leaflet	2 nm^{-2}
Bjerrum Length: l_B	0.7 nm
Interfacial Tension: γ	70 mN/m

Since for C$_n$K$_1$ ribbons, only the top and bottom surfaces are charged, the volume integral can first be thought of as a 2D integral. Let $\boxed{\mathbf{r}} = \mathbf{r} - \mathbf{r}'$ and in addition, we will perform a change of variables $x_r = x/\lambda_D$, $y_r = y/\lambda_D$. This results in eq A.5,

$$H_{elec} = 2\Big(\frac{N_T}{V}\Big)^2 V\delta k_B T l_B \lambda_D \int_0^{W/\lambda_D}\int_0^{L/\lambda_D} \frac{e^{-\sqrt{x_r^2 - y_r^2}}}{\sqrt{x_r^2 - y_r^2}} dx_r dy_r \tag{A.5}$$

The interfacial energy is:

$$H_{int} = 2\gamma\delta(L + W) \tag{A.6}$$

In eq A.6, γ is the surface tension at the hydrophobic tail/aqueous solution interface. The electrostatic and the interface energies in eqs A.5 and A.6 when divided by the membrane volume result in energy densities in eq 2.5 in the main text.

Numerical simulations for the electrostatic and the interfacial energies as a function of salt concentration and degree of ionization (main text) were carried out using the following fixed parameters for the membranes: The rough estimate for the ribbon area is based on TEM images (e.g. Figure 2.1, main text), which show membranes with areas of a few μm^2. The ribbon thickness is based on SAXS estimate of bilayer thickness of 0.38 nm. For surface molecular density, the area per lipid per leaflet is taken to be 0.5 nm^2 , which is close to the WAXS estimated APL of ~0.41 nm^2 for C$_{16}$K$_1$ (Figure 2.9, main text). Bjerrum length is that for pure water at $T = 298$K and the hydrophobic tail/aqueous interface tension is taken to be close to that for air/water interface for simplicity.

A.2 Cochleate Membranes

A membrane immersed in water with high salt concentration shapes a helicoidal-spiral surface as seen in Figure 1.3. The helicoidal-spiral surface can be described through the mapping

$$S : (z, \theta) \to \boldsymbol{X} \in \mathcal{R}^3 \tag{A.7}$$

where $\theta \in [0, \frac{R}{D}]$, and $z \in [0, w]$ in which R and w are the external radius and the width of the membrane,r espectively. The explicit mapping takes the form

$$\boldsymbol{X}(\theta, z) = (D\theta \cos\theta, D\theta \sin\theta, p\theta + z) \tag{A.8}$$

where D is the constant separation between sheets and p is the pitch of the helicoidal growing. This surface has a zero Gaussian curvature and its non-vanishing principal curvature is of the form: $K = \frac{2+\theta}{D(1+\theta^2)^{3/2}}$ while the area element is $dA = d\theta dz D\sqrt{1+\theta^2}$. Thus, the required bending energy to construct such a configuration takes the form

$$H_B[\boldsymbol{X}] = \frac{\kappa_0 D w}{2} \int_S d\theta \sqrt{1+\theta^2} K^2 \tag{A.9}$$

where κ_0 is the membrane bending rigidity. However, under this model, an spiral configuration is not energetically favourable, so other interactions are required to stabilize it. The total energy that governs a membrane with chiral and tilt ordering, immersed in a monovalent electrolyte must be of the form $H_T = H_B[\boldsymbol{X}] + H_F[\boldsymbol{X}] + H_{vW}[\boldsymbol{X}] + H_S$, where H_F is the Frank energy, and H_S is the electrostatic energy, and H_B is the bending energy.

For a membrane surface with curvature tensor K_{ab}, and a uniform tilt vector projection in the tangent plant m (the order parameter $\boldsymbol{m} = \cos\phi_0\hat{\theta} + \sin\phi_0\hat{z}$, $\phi_0 = const$), the Frank interaction reduces to the form [36],

$$H_F[\boldsymbol{X}] = \int dA[\kappa' m^a m^b K_{ac} K_b^c + \lambda_{HP} m^a m^b K_{ab}] \tag{A.10}$$

The meaning of the parameters was explained in 1.3.3. We are using the Helfrich-Prost model [36] and assuming that the tilt vector is uniform, i.e., $\boldsymbol{m} = \hat{\theta}\cos\phi_0 + \hat{z}\sin\phi_0$, where $\hat{\boldsymbol{\theta}}$, $\hat{z}$ are the unit vectors in the azimuthal and axial direction, respectively (Figure 1.3B). Thus, for a cochleate membrane, Frank energy reduces to

$$\kappa' m^a m^b K_{ac} K^c_b - \lambda_{HP} m^a m^b K_{ab} = \frac{\kappa'}{2} K^2 \cos^2\phi_0 - \lambda_{HP}\sin\phi_0\cos\phi_0 \tag{A.11}$$

Futhermore, for a surface with external radius R, width W and inter-bilayer spacing D, we can intergrate explicityly the bending energy and the electrostatic energy to get

$$H_B + H_S \simeq \frac{\kappa}{2}\int dA K^2 = \frac{\kappa W}{2}\Big[\frac{8\big(1+\frac{9D^2}{8R^2}\big)}{3\big(1+\frac{D^2}{R^2}\big)^{3/2}} + \sinh^{-1}\big[\frac{R}{D}\big]\Big] \tag{A.12}$$

where the bending rigidity is renormalized as $\kappa = \kappa_0 + c\lambda_D \sim 10^{-19}$ J due to the screening of electrostatic effects. For high salt concentrations and a planar membrane, $c = \frac{k_B T}{\pi\lambda_B}$[66].

Notice that the van der Waals interaction can be written as follows,

$$H_{vW} = \frac{-Ww}{24D}\Big[\frac{R}{D}\sqrt{1+\frac{R^2}{D^2}} + \sinh\big[\frac{R}{D}\big]\Big] \tag{A.13}$$

but $W \sim 2\times 10^{-22}$ J is the Hamaker constant, which makes this energetic contribution neglible in the continuum approximation of the membrane. Therefore, the total membrane energy takes the form

$$\frac{H_T}{W} = \frac{\kappa_T}{D}\Big[\frac{8\big(1+\frac{9D^2}{8R^2}\big)}{3\big(1+\frac{D^2}{R^2}\big)^{3/2}} + \sinh^{-1}\big[\frac{R}{D}\big]\Big] - \lambda\Big[\frac{R}{D} + \tan^{-1}\frac{R}{D}\Big] \tag{A.14}$$

where $\kappa_T = \frac{1}{2}(\kappa + \kappa'\cos^2\phi_0)$ and $\lambda = \lambda_{HP} K \sin\phi_0\cos\phi_0$. Minimization of A.14 with respect to the tilt angle ϕ_0 and the separation D provides the following relationships between the critical values and the elastic parameters of the membrane,

$$\sec 2\phi_0 = \frac{2\kappa+\kappa'}{\kappa'}, \text{ and } D\frac{g[R,D]}{f[R,D]} = \frac{\sqrt{\kappa^2+\kappa\kappa'}}{\lambda_{HP}} \tag{A.15}$$

where $f[R,D] = \left[\frac{8\left(1+\frac{9D^2}{8R^2}\right)}{3\left(1+\frac{D^2}{R^2}\right)^{3/2}} + \sinh^{-1}\left[\frac{R}{D}\right]\right]$ and $g[R,D] = \left[\frac{R}{D} + \tan^{-1}\frac{R}{D}\right]$.

Notice that while the tilt orientation of the molecules is related just with the elastic parameters of the membrane, the separation between sheets depends also on the strength of chiral interaction between lipid molecules. Thus, the membrane scroll morphology is a result of the chiral interactions among the molecules that compose the membrane. We used a test value of $R \sim 100$ nm, which is of the same order of magnitude as the experimentally determined cochleate radius, to solve for the critical distance. $\kappa_0 = 2 \times 10^{-19}$ J was used [170]. We found that the experimental data fit well with a chiral interaction of $\lambda_{HP} \sim 10^{-11}$J/m. In order to improve our estimate, we added to the optimized D value in A.15 the membrane width δ measured from SAXS.

A.3 Curvature of Cochleate Surface

Caculating the curvature of surfaces all follow the same procedure: parameterization, finding tangent and normal vectors, finding curvature tensor, and then calculating mean and gaussian curvature.

For the cochleate surface

Parameterization:

$$\boldsymbol{X} = \begin{pmatrix} D\theta\cos\theta \\ D\theta\sin\theta \\ p\theta + z \end{pmatrix} \tag{A.16}$$

Tangent Vectors:

In this case, the surface of the cochleate is parameterized by the two coordinates θ and z. So we have:

$$\hat{t}_\theta = \frac{\partial \boldsymbol{X}}{\partial \theta}, \qquad \hat{t}_z = \frac{\partial \boldsymbol{X}}{\partial z} \tag{A.17}$$

$$\hat{t}_\theta = \begin{pmatrix} D(\cos(\theta) - \theta\sin(\theta)) \\ D(\sin(\theta) + \theta\cos(\theta)) \\ p\} \end{pmatrix}, \qquad \hat{t}_z = \begin{pmatrix} 0 \\ 0 \\ 1 \end{pmatrix} \tag{A.18}$$

Normal Vector ($\hat{n} = \frac{\hat{t}_\theta \times \hat{t}_z}{|\hat{t}_\theta \times \hat{t}_z|}$):

$$\hat{n} = \begin{pmatrix} \frac{D(\sin(\theta)+\theta\cos(\theta))}{\sqrt{\left|D(\theta\cos(\theta)+\sin(\theta))\right|^2 + \left|D(\cos(\theta)-\theta\sin(\theta))\right|^2}} \\ \frac{D(\theta\sin(\theta)-\cos(\theta))}{\sqrt{\left|D(\theta\cos(\theta)+\sin(\theta))\right|^2 + \left|D(\cos(\theta)-\theta\sin(\theta))\right|^2}} \\ 0 \end{pmatrix} \tag{A.19}$$

Curvature Tensor:

$b_{ij} = \frac{\partial \hat{t}_i}{\partial x_j} \cdot \hat{n} = -\hat{t}_i \cdot \frac{\partial \hat{n}}{\partial x_j}, \qquad i = \theta, j = z$

$$\frac{d\hat{t}_\theta}{d\theta} = \begin{pmatrix} D(-2\sin(\theta) - \theta\cos(\theta)) \\ D(2\cos(\theta) - \theta\sin(\theta)) \\ 0 \end{pmatrix} \tag{A.20}$$

All other derivatives of the tangent vectors, $\frac{d\hat{t}_z}{dz} = \frac{d\hat{t}_\theta}{dz} = \frac{d\hat{t}_z}{d\theta} = \begin{pmatrix} 0 \\ 0 \\ 0 \end{pmatrix}$ Therefore, for $b_{ij} = \frac{\partial \hat{t}_i}{\partial x_j} \cdot \hat{n}$, we only need to calculate $\frac{\partial \hat{t}_\theta}{\partial \theta} \cdot \hat{n}$.

$$b_{11} = \frac{\partial \hat{t}_\theta}{\partial \theta} \cdot \hat{n} = \frac{D^2\theta}{\sqrt{\left|D(\theta\cos(\theta) + \sin(\theta))\right|^2 + \left|D(\cos(\theta) - \theta\sin(\theta))\right|^2}} = \frac{D\theta}{\sqrt{1+\theta^2}} \tag{A.21}$$

Gaussian and Mean Curvature:

The Gaussian and Mean curvature is related to b_i^j. To calculate this, we need the metric g^{ij}

(since $b_i^j = b_{ik}g^{kj}$). The inverse of g^{ij}, $g_{ij} = \hat{t}_i \cdot \hat{t}_j$, which we can calculate.

$$g_{ij} = \begin{pmatrix} \left(\theta^2+1\right)D^2+p^2 & p \\ p & 1 \end{pmatrix} \tag{A.22}$$

Therefore

$$g^{ij} = \frac{1}{\text{det}g_{ij}} \begin{pmatrix} 1 & -p \\ -p & \left(\theta^2+1\right)D^2+p^2 \end{pmatrix} = \frac{1}{D^2(1+\theta^2)} \begin{pmatrix} 1 & -p \\ -p & \left(\theta^2+1\right)D^2+p^2 \end{pmatrix} = \tag{A.23}$$

The trace of $b_i^j = b_{ik}g^{kj}$ is equal to $2H$, where H is the mean curvature and the product of the diagonal components is equal to the Gaussian curvature, K. So we have:

$$b_1^1 = b_{11}g^{11} = \frac{\theta}{D(1+\theta^2)^{3/2}}, \qquad b_1^2 = b_{11}g^{12} = \frac{-\theta p}{D(1+\theta^2)^{3/2}} \tag{A.24}$$

All other components are zero. Therefore $H = \frac{\theta}{D(1+\theta^2)^{3/2}}$ and $K = 0$

A.4 Approximate Solutions Nonlinear PB Equation [154]

The exact solution to the nonlinear PB equation for the planar geometry is [171]

$$\Psi_p(x) = 2\ln\left(\frac{1+t_0\exp(-x)}{1-t_0\exp(-x)}\right) \tag{A.25}$$

where $t_0 = \tanh\left(\frac{\Psi_0}{4}\right)$ and x is normalized by the Debye length, λ_D. Exact solutions for the nonlinear PB equation in the spherical and cylindrical geometries is not possible. To approximate solutions, the key idea is to use the exact solution for the planar case and solutions to the linearized PB (i.e. Debye-Huckel) equation for spherical and cylindrical geometries. One suggests the ansatz that curvature effects on the electrostatic potential of the surface Ψ_0 can be accounted for with the linearized solutions of the PB equation [154]. There are two ways to accomplish this.

Specifically,

$$\Psi_{s/c,\,\text{ansatz}} \simeq \Psi_{p,\,\text{exact}} \frac{\Psi_{s/c,\,\text{DH}}}{\Psi_{p,\,\text{DH}}} \tag{A.26}$$

or

$$\Psi_{s/c,\,\text{ansatz}}\Big(x,\Psi_0\Big) \simeq \Psi_{p,\,\text{exact}}\Big(x,\Psi_0 \frac{\Psi_{s/c,\,\text{DH}}}{\Psi_{p,\,\text{DH}}}\Big) \tag{A.27}$$

where s/c and p correspond to sphere/cylinder and planar, DH symbolies the Debye-Huckel solution for a given geometry. Then, the final approximate solution for a given geometry is a linear combination of these two solutions.

For the sphere, A.26 becomes $\Psi(x)_{s,1} = \Big(\frac{a}{x+a}\Big)\Psi_p(x)$ where $a = R/\lambda_D$ and A.27 becomes $\Psi(x)_{s,2} = \Psi_p(x, t_0 \to u_0(x))$ where $u_0(x) = \tanh\Big(\frac{\Psi}{4}\frac{a}{x+a}\Big)$. And the full solution for the spherical geometry is calculated as

$$\Psi_s = \Psi_{s,1}(x)[1 - \exp(-aw)] + \Psi_{s,2}(x)\exp(-aw) \tag{A.28}$$

where $w = 0.3$ most closely matches the numerical solution of the nonlinear PB equation. Similarly, for the cylinder,

$$\Psi_c = \Psi_{c,1}(x)[1 - \exp(-av)] + \Psi_{c,2}(x)\exp(-av) \tag{A.29}$$

where $\Psi(x)_{c,1} = \Big(\frac{K_0(x+a)\exp(x)}{K_0(a)}\Big)\Psi_p(x)$ where K_0 is the modified cylindrical Bessel function of the second kind, $\Psi(x)_{c,2} = \exp(x)\Psi_p(x, t_0 \to s_0(x))$ and $s_0(x) = \tanh\Big(\frac{\Psi}{4}\frac{K_0(x+a)}{K_0(a)}\Big)$, and $v = 3$.

B Chapter in Appendix

B.1 Form Factor Examples

B.1.1 Finite Slab

We consider a finite slab of length, L, width W, and thickness D. We can describe such a surface with $\boldsymbol{R} = (x, y, z) = x\hat{x} + y\hat{y} + z\hat{z}$, where $x = y = z = 0$ is at the geometric center of the slab. We consider the case that the slab has a constant electron density with respect to any background $\Delta\rho(\boldsymbol{r}) = \rho$. Therefore, eq 10 states that the form factor for such an assembly is

$$F(\boldsymbol{q}) = \int \Delta\rho(\boldsymbol{r}) \exp\big[i\boldsymbol{q}\cdot\boldsymbol{r}\big] dV = \rho \int \exp\big[i\boldsymbol{q}\cdot\boldsymbol{r}\big] dV \tag{B.1}$$

The x component for this calculation is

$$\rho \int \exp\big[iq_x x\big] dx = \frac{1}{iq_x} \exp\big[iq_x x\big]_{-L/2}^{L/2} = \frac{2}{q_x} \sin\big(\frac{q_x L}{2}\big) \tag{B.2}$$

The y and z components are similarly calculated. Therefore

$$F(\boldsymbol{q}) = \rho\Big(\frac{2}{q_x} \sin\big(\frac{q_x L}{2}\big) \frac{2}{q_y} \sin\big(\frac{q_y W}{2}\big) \frac{2}{q_z} \sin\big(\frac{q_z D}{2}\big)\Big) \tag{B.3}$$

Then, we must perform an orientational average of the θ and ϕ components of $\boldsymbol{q} = \boldsymbol{q}(q, \theta, \phi) = (q \sin\theta \cos\phi, q \sin\theta \sin\phi, q \cos\theta)$ in spherical coordinates according to 9 to relate the form factor to intensity reduced 1D (q) scattering profile. In the limit of an infinite slab sheet ($L, W \to \infty$), B.3

reduces to

$$I(q) = \frac{1}{q}\Big[\frac{2}{q}\sin\big(\frac{qD}{2}\big)\Big] \tag{B.4}$$

B.1.2 Cochleate

Some form factors, like B.4, are analytical. However, many are not. For example for a cochleate surface of constant electron density ρ, described by coordinates $\boldsymbol{X} = (D\theta \sin\theta, D\theta\cos\theta, p\theta + z)$ described in 1.3.1, we have

$$F(q, \theta_q, \phi) = \rho \int \exp[i\boldsymbol{q} \cdot (D\theta\sin\theta\hat{x} + D\theta\cos\theta\hat{y} + (p\theta + z)\hat{z})d\theta dz \tag{B.5}$$

where θ_q in $\boldsymbol{q}$ is now used to distinguish it from the real space coordinate θ. The z integration can be performed analytically, but the θ integration and orientational average over θ_q and ϕ have to be performed numerically, leading to limitations in a model dependent approach to fitting cochleate 1D scattering profiles. In principle, you can write down the form factor for any set of coordinates, but in practice, it is difficult to simulate robustly due to costly numerical computation.

B.2 Fitting Titration Data with Hill/Electrostatic Model

REACTIONS

$$NH_2 + (H^+)^m \overset{(K_a)^m}{\rightleftharpoons} NH_3^+$$

$$H^+ + OH^- \overset{K_w}{\rightleftharpoons} H_2O$$

MASS CONSERVATION

$$C_A = [NH_3^+] + [NH_2]$$

CHARGE CONSERVATION

$$[H^+] + [B^+] + [NH_3^+] = [OH^-] + [X^-]$$

VOLUMES

$$C_B = [B] = V_B \frac{C_{B,init}}{V_A + V_B}$$

$$C_A = V_A \frac{C_{A,init}}{V_A + V_B}$$

CONSTRAINTS

Figure B.1: List of reactions and constraints used to define a system of equations for titration curve analysis. The Hill exponent m [84] (discussed in the main text) is included in the amphiphile headgroup protonation reaction involving [H^+] and K_a. List of other variables: $K_w = 10^{-14}$. C_A, amphiphile concentration; C_B, total concentration of added base (in this case, [B^+]=[Na^+]); V_A is the volume of the amphiphile solution before any NaOH is added and V_B is the volume of the NaOH solution added ; X^-, counterions for the protonated amphiphiles.

The reactions, conserved quantities, and volume constraints during a titration measurement define a system of equations. We rewrite the system of equations by eliminating variables to solve for the volume of base as a function of pH (the inverse of what is experimentally performed during titration, but mathematically equivalent and more tractable). In other words, we solve this system of equations for $V_B = f([H^+]; K_a, m)$ and vary the parameters K_a, m to fit the titration data. The best-fit values for K_a and m are then inserted into the Hill equation (eq 2.1, main text) to calculate the degree of ionization at different pH levels. The above-described method for analyzing titration curves can naturally be extended to go beyond a monoprotic model [e.g. diprotic (H^2-A) or triprotic

(H^3 -A)] by including more reactions and charge/volume constraints to the system of equations. The same procedure is used in the electrostatic model of titration with V_B now a function of degree of ionization α which is determined self-consistently with the charge regulation boundary conditions discussed in 4, instead of the Hill coefficient m. Specifically,

$$V_B = f([\mathrm{H}^+]; K_a, \alpha) = V_A\Big(\frac{-H^2 - H \cdot C_{A,init}\alpha + K_w}{H^2 + H \cdot C_{B,init} - K_w} + \frac{C_{A,init}}{C_{B,init}}\Big) \tag{B.6}$$

To compare titration curves for experiments performed with different volumes of sample solution, we divide this expression by V_{equiv}, the equivalence volume of the defined in 4 (inflection point of titration curve).

B.3 WAXS Fitting and Analysis

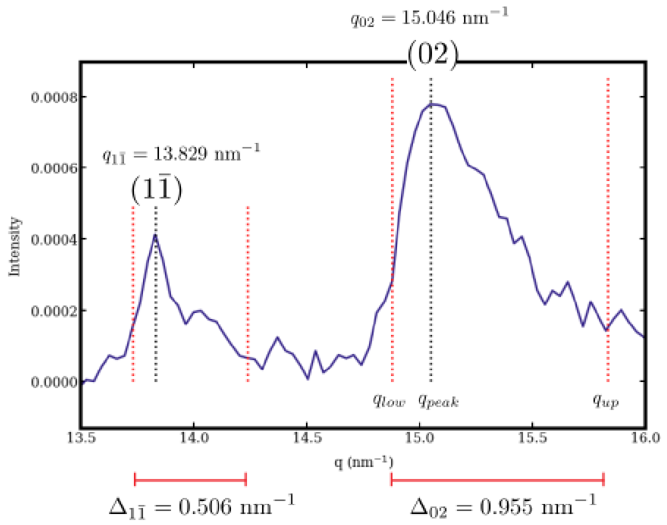

$$I(q_{low}) = \frac{1}{e} I(q_{peak})$$

$$I(q_{up}) = \frac{1}{2e} I(q_{peak})$$

$$\Delta = q_{up} - q_{low}$$

$$L_{hk} = \frac{4\lambda}{B_{hk} \cos\theta_{hk} \sqrt{\pi}} \qquad \sigma_{hk} = \frac{2\pi}{L_{hk}}$$

$$B_{hk} = \Delta_{hk} \text{ in radians}$$

$$\implies L_{10} \simeq 83 \text{ nm}, \; L_{01} \simeq 28 \text{ nm}$$

$$L_{hk} = L_{10}\Big(\frac{|h|}{|h|+|k|}\Big) + L_{01}\Big(\frac{|k|}{|h|+|k|}\Big)$$

Figure B.2: Correlation length calculation procedure based on Haruyunyan et al [98]. Peak width definitions involve an extra factor of $1/2$ for the upper side of the peak (q_{up}) to account for the long tails of observed asymmetric diffracted intensity profiles. Peak broadening is based on the Scherrer equation and an empirical relationship for the correlation lengths of different reflections, described below.

WAXS analysis $C_{16}K_1$ bilayer membranes followed the procedure for 3D powder averaging of scattered intensity from a 2D lattice described by Harutyunyan et. al. [98] leading to an intensity profile:

$$I(q) \propto e^{-q^2\lambda_{DW}} \sum_{hk} \int_0^{\pi} |F(\vec{q}_{hk}, q_z|^2 e^{-\frac{1}{2\sigma_{hk}^2}(q\sin\theta - q_{hk})^2} \sigma_{hk} \sqrt{\frac{2\pi \sin\theta}{q q_{hk}}} d\theta \tag{B.7}$$

Here, h and k are the Miller indices for a given Bragg reflection, q_{hk} is the corresponding reciprocal lattice vector that is directly related to the real space oblique lattice parameters a, b, and γ described in the main text. $q_z = q\cos\theta$ is the scattering vector component normal to the 2D lattice. $F(q_{hk}, q_z)$ is the unit cell form factor resulting from interference of scattered X-rays from different molecules within a unit cell. The Gaussian term in the integrand is the effective structure factor resulting from the summation of scattering from distinct unit cells. The leading exponential term is the effective Debye-Waller factor that arises from thermal fluctuations. The diffracted intensity is characterized by a spread $\sigma_{hk} = 2\sigma/L_{hk}$ that is inversely proportional to a correlation length. The correlation length for a given (hk) reflection is based on an empirical formulation: $L_{hk} = L_{10}[|h|/(|h| + |k|)] + L_{01}[|h|/(|h| + |k|)]$. Based on fitting of WAXS (Figure B.2), we find that $L_{10} \sim 3L_{01}$, which we attribute to the elongated aspect ratio of the observed bilayer ribbons.

In order to calculate the unit cell form factor, we assume two C$_{16}$K$_1$ molecules per unit cell and focus only on the interdigitated tail region. We approximate the tails as parallelepiped rods leading to a form factor

$$F(\vec{q}_{hk}, q_z) = \rho_t\Big(\mathrm{sinc}(\frac{q_x t_x}{2})\mathrm{sinc}(\frac{q_y t_y}{2}\mathrm{sinc}(\frac{1 - e^{iq_z h_z}}{iq_z h_z}))\Big) \tag{B.8}$$

Here the dimensions of the rod are $t_x = t_y = 0.45$ nm, and $h_z = 1.9$ nm, q_x and q_y are the x and y components of the reciprocal lattice vector q_{hk} , q_z is the z component of the scattering vector, and ρ_t is the electron density of the tails (a scaling parameter). We include the tilt of the tails with respect to the bilayer normal by performing a transformation of q_x, q_y and q_z over two rotation axes. η is a rotation angle with respect to the x-axis and β a rotation angle with respect to the y-axis.

$$q_{xt} = q_x\cos\beta + q_z\sin\beta \tag{B.9}$$

$$q_{yt} = q_x\sin\eta\sin\beta + q_y\cos\eta - q_z\sin\eta\cos\beta \tag{B.10}$$

$$q_{zt} = q_x\cos\eta\sin\beta + q_y\sin\eta - q_z\cos\eta\cos\beta \tag{B.11}$$

C Chapter in Appendix

C.1 L-/D-$C_{16}K_1$ Atomistic Effects in CHARRM36

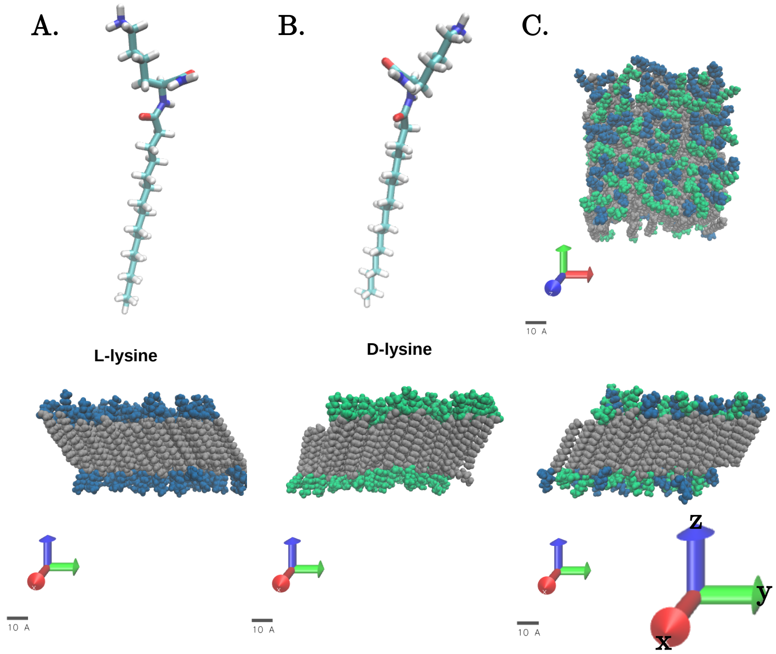

Figure C.1: **A.** L-$C_{16}K_1$ (blue) and **B.** D-$C_{16}K_1$ molecules used in atomistic simulations are shown. Note the mirrored handedness of the head group when comparing **A** and **B** molecules. Bilayers with tilt order are found for both L- and D-$C_{16}K_1$ bilayers. The tilt direction (with respect to x,y, and z coordinate system of simulations shown in bottom right, seems to flip when switching from one enantiomer to the other consistent with expectations discussed in 0.2.3. However, periodic boundary conditions limit the ability to define a unique tilt direction with respect to in-plane bilayer structure. Magnitude of tilt with respect to bilayer normal was similar between enantiomers. **C.** Racemic simulations showing bilayer formed from equal mixture of left and right handed molecules. Racemic bilayers displayed similar tilt order to D-$C_{16}K_1$ simulations, in contradiction of models discussed 0.2.3. Therefore, tilt in relation to chiral effects in atomistic simulations require further investigation.

C.2 Mapping of C_nK_1 in Martini 2.2P

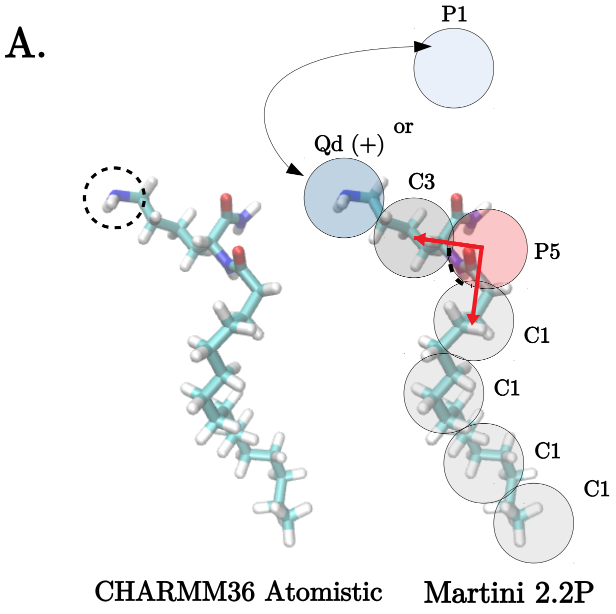

B.

	Bond Length (A)	Bond Force.C.
P5-C1 (+)	0.36	5000
P5-C1	0.39	5000
C1-C1	0.47	1250
Qd-C3	0.28	5000
C3-P5	0.33	5000

	Angle (deg)	Angle Force.C.
C3-P5-C1 (+)	135	25.0
C3-P5-C1	107	25.0
C1-C1-C1	180	25.0
Qd-C3-P5	180	25.0

Figure C.2: A. Parameterization of C_nK_1 molecules in different force fields. Specifically, $C_{16}K_1$ is shown. **B.** Bond lengths and angles in Martini 2.2P are fit to CHARMM36 atomistic simulations.

Figure C.2 illustrates different force fields used for MD simulations. The CHARMM36 force field was used for atomistic simulations of C_nK_1. Shown in Figure C.2 (left) is the uncharged version of $C_{16}K_1$. For the charged molecules, the amine side chain group (black dotted circle) contains an additional hydrogen atom to be in its positively charged, protonated state. The listed Martini 2.2P beads were used to parameterize $C_{16}K_1$ molecule for CG simulations. The lysine amino acid was modelled in its protonated (charged) or deprotonated (uncharged) state following [113]. All bond lengths and angles were matched to atomistic simulations results, listed in the lower half of the figure herein. Highlighted in red, and illustrated with red arrows in the Martini 2.2P CG representation is an example bond angle and length that was mapped from atomistic simulations following guidelines outlined at http://www.cgmartini.nl/index.php/tutorials-general-introduction-gmx5/parametrzining-new-molecule-gmx5. Bond lengths and angles for other atoms are similar to other Martini 2.2P representations of surfactant/lipid molecules [105].

C.3 Titratable Martini for Constant pH MD Simulations (Martini Sour)

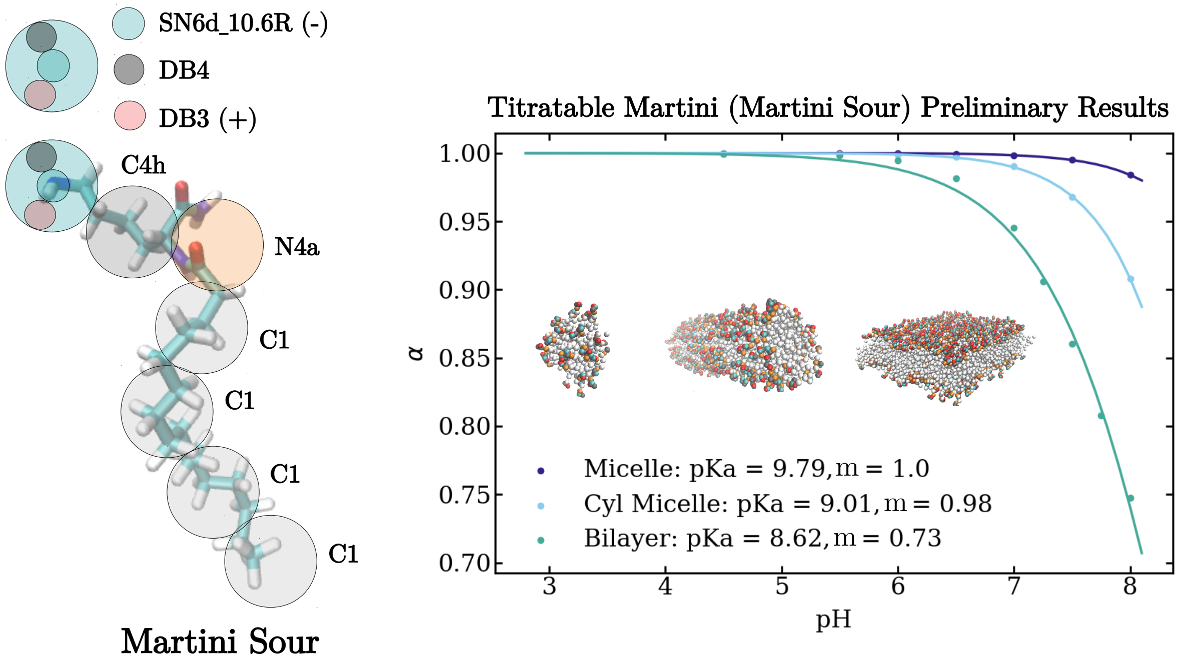

Figure C.3: Parameterization of $C_{16}K_1$ molecules in titratable Martini force field is shown to the left. Here, the charged Martini bead is replaced by a titratable bead which has the ability to exchange charged proton beads with the surrounding titratable water solvent. See [130] for more details on the titratable Martini force field. Preliminary results using the titratable Martini force field show the geometry of the $C_{16}K_1$ assembly has an effect on the degree of ionization, α.

Titration measurements and corresponding degree of ionization plots for C$_{16}$K$_1$ assemblies (micelle, cylindrical micelle, and bilayer) are shown. All simulations were performed with a step size of 8 fs. Simulations were performed at pH = 4.5, 5.0, 5.5, 6.0, 6.5, 7.0, 7.5, 8.0 for the different assemblies. 50 C$_{16}$K$_1$ molecules were simulated in a box size of $\sim 8 \times 8 \times 8$ nm^3 with Parrinello-Rahman isotropic pressure coupling and micelles formed. After formation, simulations were run for an additional 50ns which was analyzed for the degree of ionization shown in Figure C.3 following http://cgmartini.nl/images/stories/workshop2021/tutorials/tutorial_11/titratable_tutorial.pdf. Additional tutorial materials can now be found in [132]. Similarly, 180 C$_{16}$K$_1$ molecules, simulated with isotropic pressure coupling in a box size of $\sim 8 \times 8 \times 8$ nm^3 formed cylindrical micelles across the periodic boundaries. Following formation, cylindrical micelles were simulated for an additional 80 ns which was analyzed for degree of ionization. For bilayers, 180 C$_{16}$K$_1$ molecules were pre-assembled into a bilayer with normal oriented in the z-axis configuration using packmol [114] in a $\sim 6 \times 6 \times 10.5$ nm^3 box periodic boundary conditions in all directions. Upon equilibration, bilayers were simulated with semi-isotropic pressure coupling for 80 ns which was analyzed for the degree of ionization. The inset of Figure C.3 shows a snap shot of the micelle, cylindrical micelle, and bilayer configurations where bead colors correspond to color scheme shown in Figure C.2.

The most notable finding is that the equilibrium constant, pK_a, and Hill coefficient, m, decrease with assembly geometry proceeding as micelle to cylindrical micelle to bilayer. The closeness of packing of these assemblies represented by nearest neighbor distance (d_{NN}) proceeds as $d_{NN,\text{ micelle}} > d_{NN,\text{ cyl micelle}} > d_{NN,\text{ bilayer}}$. The order of magnitude shift from pK_a = 9.79 for micelles to pK_a = 8.62 for bilayers in the acid−base equilibrium constant implies a reduction in the tendency of the lysines in C$_{16}$K$_1$ to be ionized when they are assembled in more closely packed assemblies. Such charge regulation is expected because any arrangement of like-charged molecules in proximity increases the electrostatic potential energy of assemblies. The additional electrostatic potential energy is also manifested with a change in copperativity between sites represented by m ($m = 1.0$ for micelles to $m = 0.73$ for bilayers). Ionizable sites in micelles assemblies, with larger site-to-site distance separations, behave similar to dilute solution. However, when the same sites are assembled in bilayers, there is increased anti-cooperativity ($m < 1$) between the sites symbolizing the interaction between these closely packed ionizable sites.

C.4 Monte Carlo/Molecular Dynamics (MCMD) Simulations of $C_{16}K_2$ Micelle Assemblies

Colloidal nano-particles acquire charge due the ionization of acid or basic groups. The degree of ionizations depends on the pH and salt concentration of the solution but also the influenced by the presence of other charged particles in the vicinity. Charge-regulation (CR) effects have been shown to reduce the electrostatic repulsion between like-charged particles and increase the attraction between a large particle coated with dissociable sites and small ions. To better understand such effects when considering $C_{16}K_2$ micelle assemblies, we performed hybrid MCMD simulations.

Similar to modelling with the nonlinear PB equation described in 4, we model the CR by the reaction:

$$\mathrm{B} \rightleftharpoons \mathrm{B}^{+} + \mathrm{OH}^{-} \tag{C.1}$$

In this equation the base acid group (B) is ionized by a hydroxyl ion OH^- from the system to the reservoir. The solution contains free ions (salt, protons and hydroxyl ions) of diameter l_B where $l_B = q_0/(4\epsilon_0 k_B T)$ is the Bjeerum length. q_0 the elementary charge and ϵ_0 the vacuum permittivity. Simulations were performed using the Large-scale Atomic/Molecular Massive Parallel Simulator (LAMMPS) and using the molecular dynamics package for Charge Regulation MD/MC hybrid tool for modeling CR effects in solvated systems [30, 172]. The system contains 108 shell-spherical nanoparticles immersed in an implicit solvent with a dielectric constant ϵ. The simulation was performance using periodic boundary conditions in a cube box of size $75 l_B$. Each nanoparticle contains n_A dissociable groups uniformly distributed on a spherical shell. Depending on the ionic environment of the system, the degree of ionization of the dissociable groups on the shell can change. For Figure 4.8D, n_A = 106, 110, 114, 122, 130, 140, 150 and 158, which are related to the salt concentration in the system, corresponding to the values equal to 10^{-5}, 5, 10, 25, 50, 100, 175 and 200 mM, respectively. These aggregation numbers correspond to the SAXS measured values highlighted in Figure 4.2. These salt concentrations are related with the values pI_s = 5, 2.3, 2, 1.6, 1, 0.75 and 0.69, which are inputted into the simulation. The interactions between the ions and the dissociable groups are modelled with a long range electrostatic potential. Electrostatic interactions are considered by the PPPM algorithm with accuracy of 10^{-4} and the real space cutoff $r_{cut} = 10l_B$. The excluded-volume interaction is modelled through a LJ potential.

All the simulations shown in Figure 4.8D were performed at pH = 6. The base groups on the surface of the nanoparticle have dissociation constant pK_a = 10.5, equivalent to what was used in the nonlinear PB modelling discussed in the main text. We start the simulation with a random configuration for the spherical nanoparticles of $r = 2l_B$. We use a Langevin thermostat with damping time $\tau = \sqrt{m\sigma^2/k_BT}$, where m is the ion mass. For the simulations, we use a damping time equal to 20τ. We run $1.5 \times 10^6\tau$ for equilibration and $5 \times 10^5\tau$ for productions runs with an MD time step $\delta t = 0.001\tau$. After every 800 MD steps, we perform 200 MC steps to determine the preferred ionization state of the dissociable groups. Radial distribution functions of the negatively charged ions ($g(r)$) were calculated from five different equilibrium configurations generated in the simulation. From the radial distribution function of negatively charged ions surrounding the charged nanoparticle, we can calculate the effective charge of the micelle assemblies using 4.7. We note here that when the system is at high salt concentration, $g(r)$ shows an additional two consecutive peaks, meaning we have two layers of negatively free ions around the nanoparticle.

D Chapter in Appendix

D.1 List of Codes and Resources

- List of codes and data used in this manuscript are published on github, https://github.com/josephmccourt2018/thesis.
- A useful MD simulations in Gromacs tutorial by Justin Lemkul: http://www.mdtutorials.com/gmx/ (and then specifically with the Martini force field http://cgmartini.nl/index.php/tutorials-general-introduction-gmx5) and for MD simulations in LAMMPS: https://lammpstutorials.github.io/index.html.